Master's thesis

NTNU
Norwegian University of Science and Technology
Faculty of Engineering
Department of Energy and Process Engineering

Erling Gjeset

Thermal Management Systems for Compact Electrical Machines

Master's thesis in MTPROD
Supervisor: Erling Næss
June 2020

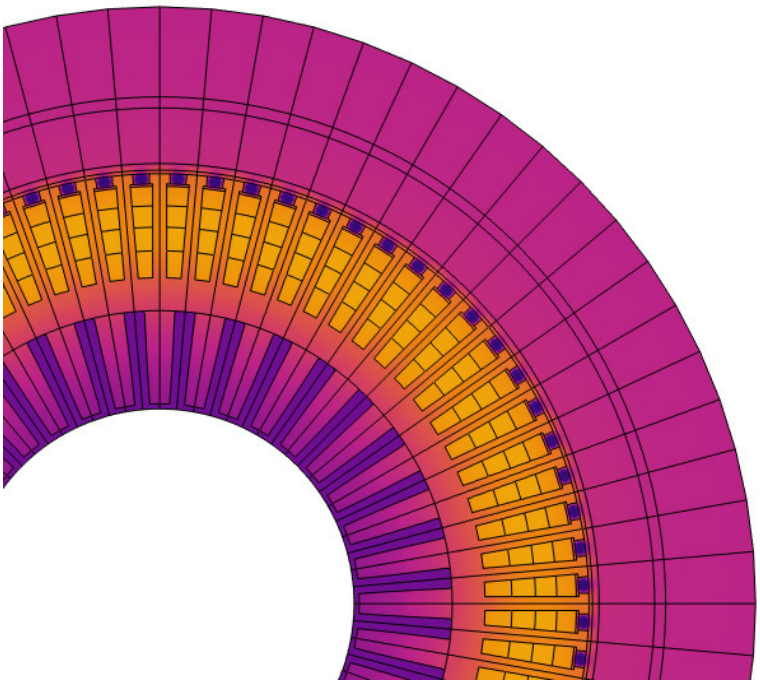

NTNU
Norwegian University of
Science and Technology

Erling Gjeset

Thermal Management Systems for Compact Electrical Machines

Master's thesis in MTPROD
Supervisor: Erling Næss
June 2020

Norwegian University of Science and Technology
Faculty of Engineering
Department of Energy and Process Engineering

NTNU
Norwegian University of
Science and Technology

Thermal Management Systems for Compact Electrical Machines

NTNU and Rolls-Royce are working on sustainable technologies for the future "more electric aircraft" (MEA). Preliminary work on the thermal management and engine cooling system concepts has been done for a compact, high-efficiency electrical machine. Further studies will focus on expanding upon the different options.

1. An overview of published/available cooling concepts for compact electrical machines shall be presented and discussed
2. Two thermal management systems, based on air and thermal oil as coolant, shall be analyzed. The oil system will be based on the existing design from the project work, but is to be further expanded to account for previous assumptions. Both the oil and air-based systems shall be optimized with regards to coolant mass flow rate, hot spot temperatures and geometry. Based on the performance analysis, a comparison shall be drawn between the alternatives.

The heating caused by electrical resistance within the conducting wires of electrical engines can become critical in high current density machines. In order to create better thermal models, a study will be performed regarding the effective transverse and longitudinal thermal conductivity of the windings.

3. A calculation model shall be established for the calculation of transverse and longitudinal temperature distribution in electrical wire mesh conductors having internal heat generation due to ohmic resistance. Wire mesh geometries and resin materials shall be defined in cooperation with the Department. Relevant factors influencing the heat flow and temperature distribution shall be investigated. Based on model calculations, simplified 'engineering'-type correlations/models shall be proposed.
4. Suggestions for further work shall be presented and discussed.

Preface

On my desk, right next to my monitors, stands a 1:48th scale model replica of a Mk.XIII De Havilland Mosquito, a WW2 British military aircraft famous for its ingenious design letting it be one of the fastest planes of its era. The assembly is not my best work, but this is the first model aircraft that I built back when I was in elementary school, and it is this plane that opened up my fascination for mechanical engineering. I am still mesmerized by the levels of advancement that led from da Vinci, Otto Lilienthal, through the Wright brothers, biplanes, Mosquitoes and into the modern jet age. It is the progress that has led us to master the power of flight, however mysterious the science behind it might seem.

It is my hope that this development does not stop, and that the forward focus will be on creating greener alternatives, cutting greenhouse gas emissions from air travel. I believe that electrifying aircraft is a good possibility to achieve this, and I am very happy to contribute my small part in the further evolution of aircraft engineering towards a respectable goal.

Figure 1: De Havilland Mosquito (1:48th scale model replica)

This thesis is written as a part of the M.Sc. in mechanical engineering at the institute of energy and process engineering, NTNU, in the spring of 2020. The work was done in collaboration between NTNU and Rolls-Royce Electrical Norway. The project's initial goal was to continue previous work done during the fall of 2019 and create an experimental test rig to study. Due to time restrictions and the global outbreak of COVID-19, this could not be achieved. The previous thesis statement is given in the appendix.

I would like to thank my supervisors; Erling Næss and Kolbeinn Kristjansson, the coordinator at RREN; Børge Noddeland, and my two collaboration partners; Sigurd Bøyum Fossum and Lars Helge Verde.

Trondheim, June, 2020

Erling Gjeset

Summary

During the transition to more electric aircraft (MEA), more compact, lighter electric machines will be built to power the new planes. These motors place stricter requirements on performance from all engineering aspects.

A team of of students of electromagnetic, mechanical and thermal engineering will in this project design and evaluate a prototype, high speed machine with an external rotor configuration. This report focuses on the thermal management, constructing a cooling system capable of ensuring a sufficiently low operating temperature. Two separate methods are considered, a closed-loop and an open-loop system using oil or air, respectively. These are integrated with the motor geometry and evaluated through numerical software

The study shows that either configuration is a good option for the thermal management system of the prototype, since they both manage to keep the temperatures below the material limits at relatively low pumping cost. This is due to the distribution of the cooling ducts, combining both direct and indirect cooling. However, both alternatives have their separate advantages and drawbacks considering the practical implementation onto an electric aircraft motor. This includes weight, ducting and pumping issues, ancillary heat exchanger sizing etc. These concerns are noted, but the study was not able to quantify their impact, as they require more real-life experience with the actual machine and/or more part-specific analysis.

Two separate, more detailed studies were also performed: flow modelling of the air gap between the stator and rotor, and the winding composite thermal conductivity. The aim was to find a good engineering correlation for use in the thermal modelling of electrical machines. Previous, similar models have been collected from literature and evaluated against numerical simulations.

The flow structure in the air gap exhibits both turbulence and Taylor vortices, and has proven too complex to be captured by the simplified 2D-model used in this report. Likewise, the correlations from previous work indicate strong dependencies on the experiments' geometry and boundary conditions, as they do not correlate well with each other. More in-depth research is needed within this field to find a more fitting model.

The homogenization techniques used for calculating the bulk thermal conductivity of windings are shown to correlate well with the more detailed, numerical results. The more recent relations are the ones following closest to the simulations, as they are able to account for more of the geometrical elements. However, these models relate to straight wire windings, and are not able to capture the transposition effect in twisted litz wire. In this case, the complex geometry proves difficult to generalize, though previous work shows promise in modelling such compositions as thermal resistance networks.

Sammendrag

Elektrifisering av luftfarten stiller høyere krav til elektromotorene som skal drifte hybride eller helelektriske fly. De må være kompakte, sikre og ha lav vekt. Dette krever mer av utviklerne innenfor alle ingeniøraspekter.

En samarbeidsgruppe bestående av elektroingeniører, maskiningeniører og termiske ingeniører har blitt satt sammen for å utvikle og evaluere en prototype av en høyhastighets-, elektrisk flymotor med en utvendig rotor. Denne raporten fokuserer på den termiske styringen av maskinen. To kjølesystem skal testes, en lukket oljekrets og en åpen luftkrets, for å se hvilken som er best i stand til å kjøle motoren under materialgrensetemperaturene. De to systemene integreres med elmotor-geometrien og simuleres numerisk.

Studiet viser at begge kretsene er potensielle kandidater, ettersom de er i stand til å opprettholde forsvarlige temperaturer i motoren ved relativt lav pumpekraft. Dette er på grunn av fordelingen av kjølekanaler, som benytter seg både av direkte og indirekte kjøling. Systemene har sine fordeler og ulemper når det kommer til den praktiske implementeringen i en flymotor, slik som vekt, innløps-/utløpskanaler, pumper, eksterne varmevekslere etc. Disse aspektene blir påpekt og vurdert, men kan ikke bli tallfestet, ettersom dette krever mer praktisk erfaring og/eller detaljstudier av de aktuelle komponentene.

I tillegg til hovedprosjektet har det blitt foretatt to detaljstudier: strømningsmodellering av luftgapet mellom stator og rotor, og homogeniseringsmodeller av viklingene i stator. Målet for begge var å finne gode ”ingeniørmodeller” til bruk i termisk modellering av elektromotorer. Lignende studier fra litteraturen har blitt sammenlignet med numeriske beregninger.

I luftgapet vil luftstrømmene være turbulente og inneholde Taylor-virvler, som har vist seg vanskelig å modellere med den nåværende 2D-strømningsmodellen. Korrelasjonene fra tidligere arbeid viser dessuten store variasjoner basert på hvilke geometrier og grensebetingelser som er brukt i eksperimentene. Mer grundig analyse trengs for å finne en passende modell.

Homogeniseringsteknikkene som er funnet i litteraturen stemmer bra med den numeriske analysen. De mest moderne relasjonene er de som følger tettest opp mot simuleringene, ettersom de er i bedre stand til å ta i betraktning den komplekse geometrien. Til tross for dette får hverken av modellene til å fange opp ”transposisjonseffekten” som er i litzviklinger. Den sammenflettede strukturen til litz gjør seg vanskelig å generalisere, men nylige rapporter ser ut til å kunne klare dette ved hjelp av termiske resistansnettverk.

Contents

List of Tables

List of Figures

Nomenclature

Abbreviations

AC	Alternating current
CCW	Counterclockwise
CFD	Computational fluid dynamics
CS	Cross-section
DC	Direct current
ER	External rotor
FE	Finite element
HSP	High specific power
TC	Taylor-Couette flow
TCP	Taylor-Couette-Poiseuille flow
TMS	Thermal Management system

Subscripts

A	Active section of stator
ag	Air gap
amb	Ambient
B	Wire bundle
b	Bulk condition
C	Conductor
E	Encapsulant
el	Electrical
EW	End winding
fb	Fin base
fs	Finned surface
I	Electrical insulation
if	Internal, finned annulus
in	Inlet
L	Laminate steel
lz	Litz bulk property
nc	Non-conductor
out	Outlet
oc	Outside channel
R	Rotor
Ri	Rotor inside
Ro	Rotor outside
S	Stator
s	Outer surface
sl	Slot
So	Stator outside
th	Thermal
W	Winding
ws	Wire strand
0	Unaltered
λ	Longitudinal
τ	Transverse
$\square$	Orthogonal array
$\triangle$	Orthocyclic array

Symbols

A	Area [m^2]
c_p	Specific heat capacity [J/kgK]
	@ Constant pressure
C_f	Friction factor (longitudinal)
C_w	Windage friction factor (rotational)
D	Diameter [m]
D_h	Hydraulic diameter [m]
H	Litz bundle height [m]
h	Convection coefficient [W/m^2K]
I	Electric current [A]
k	Thermal conductivity [W/mK]
L	Axial length [m]
$\dot{m}$	Mass flow rate [kg/s]
m^*	Mass flow split ratio
Nu	Nusselt number
P	Pressure [Pa]
PF	Packing factor
$\underline{PF}$	$1 - PF$
$\overline{PF}$	$1 + PF$
Pr	Prandtl number
$\dot{q}$	Volumetric heat generation [W/m^3]
q'	Cross-section heat generation [W/m]
q"	Heat flux [W/m^2]
$\dot{Q}$	Heat rate [W]
R	Radius [m]
$\mathbb{R}$	Resistance [Ω or K/W]
$\mathbb{R}''$	Contact resistance [m^2K/W]
Re	Reynolds number
T	Temperature [K]
Ta	Taylor number
t	Thickness [m]
U	Voltage [V]
V	Velocity [m/s]
W	Litz bundle width [m]
$\dot{W}$	Mechanical work rate [W]
z	Axial coordinate [m]
Γ	Air gap aspect ratio
δ	Air gap thickness [m]
ϵ_{fs}	Fin effectiveness
ηfs	Fin efficiency
θ	Angular coordinate [rad]
Λ	Litz wire length of lay [m]
μ	Dynamic viscosity [Pa s]
ν	Kinematic viscosity [m^2/s]
ρ	Density [kg/m^3]
ϱ	Radius ratio
Φ	Flow rate coefficient
ω	Angular velocity [rad/s]

Chapter 1

Introduction

In order to satisfy the demand of lowering greenhouse gas emissions, the aircraft industry is looking into electrifying their propulsion systems. Though the technology for electric planes is not new,[1] there is still more development needed to create a economically feasible, secure system for mass employment.

This report will look into electric engines, more specifically the high-speed, high specific power (HSP) machines needed to power the propulsion devices on e-aircraft. These new, compact motors intensifies the demands put on the thermal management systems (TMS) due to high loss densities and small available spaces in which to implement cooling devices.

1.1 Motivation

Electrification has become an increasingly more popular solution to the growing demand of low or zero emission technology. By de-carbonizing our energy consumption, replacing oil, coal and gas powered power plants with electric machines. The goal is to drastically reduce pollutants discharged from the fuel-burning systems.

The transition from fossil fuels to greener energy sources is envisioned to be achieved by the following methods:[2]

I. Changes in public opinion

II. New policies

III. Advancements in technology

[1] Hepperle 2012.
[2] Armstrong et al. 2016.

The land-based transport industry has experienced such development, with a expansion in the production and sales of electric cars. Norway is one of the countries with the highest densities of such vehicles, where, between 2013 and 2018, the amount of new zero-emission cars rose by almost 1000%, which is thought to be due to economic incentives from the government.[3] This has a snowball effect on the popularity and innovation, further affecting new sales and production. It is estimated that by following this trend from 2010-2050, it would be possible to save 400 million tons of CO_2 emitted.[4]

In this case, it is possible to point out that the main driving force has been the enticements laid out by the state, though this would not have been possible without the contemporary development of more efficient and long range electric cars, as well as the growing interest to own such vehicles. As such, the transformation will need all three aspects in order to succeed properly, and finding the starting point is often a case of choosing the chicken or the egg.

It must also be mentioned that the overall percentage of electric vehicles is low, about 7% in Norway as of 2019,[5] and that the switch from fuel to electric is not without its own problems, such as costs, range, charging and sustainable production.[6]

Despite its drawbacks, the trend shows that the possibility exists to drastically cut the carbon emissions from ground transport, which in turn drives the motivation for electrification of other types of vehicles, such as aircraft.[7] In fact, a recent report from the Norwegian Civil Aviation Authority and Avinor puts forth the possibilities of enabling more electric aircraft for regional transport, attempting to copy the success of electric cars.[8] Reaching this goal is not as straight-forward as duplicating the recipe for cars, since requirements on economy, logistics and safety are different. Many companies, such as Lilium, Equator Aircraft, Eviation, Airbus and Rolls-Royce are developing new, e-aircraft technology,[9] but these are at the time of this report still in the concept/development-phase. The current technology is not yet capable of efficiently transporting enough passengers and/or goods in order to have economically feasible air transport.

This report will focus on the enabling technology for electric flight, specifically the electric motor itself. The other mechanisms, I. and II. are not further covered, but can be studied in "The Frontiers of Energy", "Vehicle Electrification: Status and Issues" and *Forslag til program for introduksjon av elektrifiserte fly i kommersiell luftfart*.[10]

[3] NTB Nyhetsbyrå 2020; Statistisk Sentralbyrå 2018; Statistisk Sentralbyrå 2019.
[4] NTB Nyhetsbyrå 2020.
[5] Statistisk Sentralbyrå 2019.
[6] Boulanger et al. 2011.
[7] Hepperle 2012; Masson et al. 2007.
[8] Larsen and Steinland 2020.
[9] Airbus 2019; Equator Aircraft 2019; Eviation 2019; Lilium 2019.
[10] Armstrong et al. 2016; Boulanger et al. 2011; Larsen and Steinland 2020.

1.1.1 Technology Advancements

A powered aircraft uses an aerodynamic propulsion device, most often a fan or propeller, to accelerate an air flow and provide thrust. Generally speaking, this is a power conversion system; some energy source is converted to mechanical energy which drives the propulsion component. At the present moment, this mechanical power is almost always provided by an internal combustion engine, either a piston or turbine machine. Some common modern-day configurations are described in figure 1.1.[11]

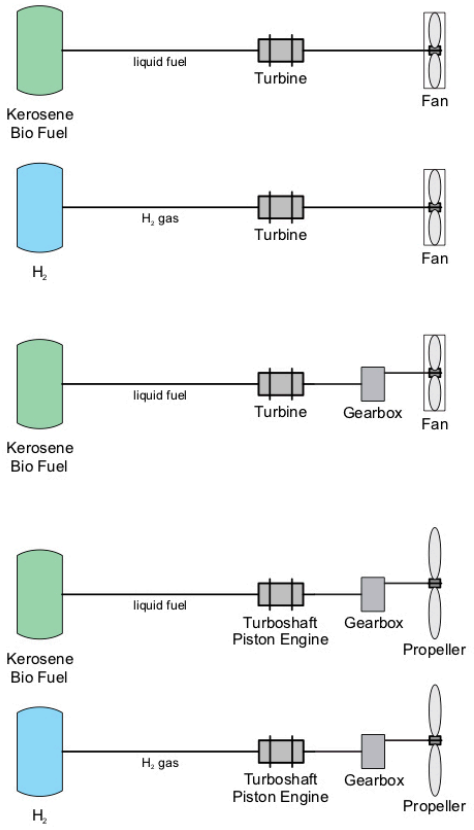

Source: Hepperle 2012.
Figure 1.1: Common internal combustion power conversion systems.

The key challenge with the current system are the emissions, mainly consisting of greenhouse gases and particulate matter.[12] The hopes are that by partly or fully electrifying the power conversion chains, the exhaust will be reduced. This can be achieved by switching out one or more of the components shown in figure 1.1 with electrical machines. Multiple

[11] Hepperle 2012.
[12] Heywood 1988.

concepts already exist, as shown in table 1.1 and figure 1.2, though they have limitations on weight, efficiency and safety. One issue is the energy density of modern-day batteries and hydrogen fuels compared to hydrocarbon fuels.[13] Another matter is the motor itself, producing the mechanical work necessary to propel the aircraft at comparable power-to-weight ratios to modern-day jet engines.[14]

	Weight	**Efficiency**	**Emissions**
Turboprop	low	∼45%	HC exhaust
Turbofan	low	∼35%	HC exhaust
Battery electric	high	∼75%	none
Hydrogen electric	medium	∼45%	water vapor

Table 1.1: Comparison between the typical energy conversion chain options for aircraft.

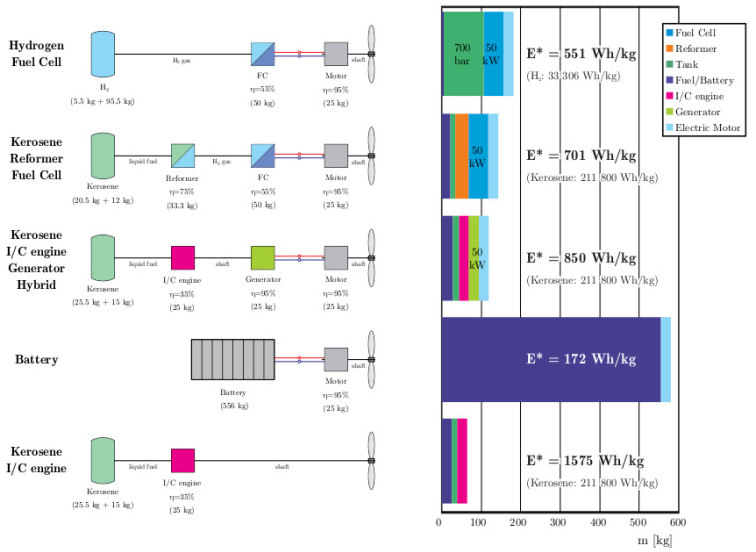

Source: Hepperle 2012.

Figure 1.2: Power conversion systems mass/energy comparison (generalized).

The turbojets and turbofans presently used in aircraft have had time to develop since the mid 20^{th} century, and current large passenger airliners operate with megawatt-scale propulsion pods.[15] Comparatively, most of the existing electric motor concepts or designs for aviation produce 100 kW or less.[16] In order to compete, new electric machines capable

[13] Armstrong et al. 2016; Boulanger et al. 2011; Hepperle 2012; Larsen and Steinland 2020.
[14] Hepperle 2012; Kahourzade et al. 2018; McFarland, Jahns, and El 2015; Wikipedia 2020; Yi 2016.
[15] Loftin 1985.
[16] Duffy et al. 2018; Hepperle 2012.

of matching or surpassing the jet engine characteristics have to be designed. Such requirements present new challenges for the developers in the fields of electromagnetic, structural and thermal engineering.

1.2 High Power Electrical Aircraft Motors

Rolls Royce joined Airbus in 2017 on the hybrid-electric E-Fan X aircraft.[17] The project aimed to create an electric flight demonstrator out of a 100-seater regional jet by removing one of the four turbofans and replacing it with an electric propulsion unit, which in turn would be supplied by a gas turbine generator and batteries,[18] as shown in figure 1.3.[19] The E-Fan X motor is rated at 2 MW, and is over 60 times more powerful than any previous iterations from Airbus.[20] Sadly, the project was ended in spring 2020, before the aircraft was able to do its demonstration flight.[21]

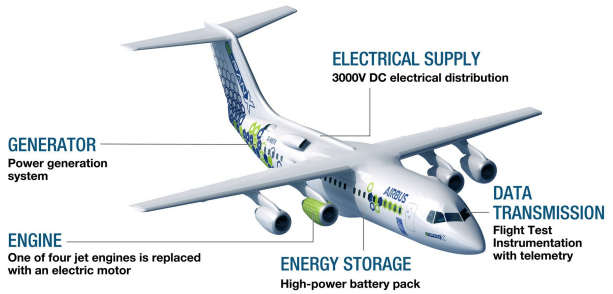

Source: Airbus 2019.
Figure 1.3: Airbus E-Fan X electric flight demonstrator.

Despite the setback, Rolls-Royce Electrical Norway is still working on high power electrical aircraft motors. In a joint operation between the company and the Norwegian university of science and technology (NTNU), a research team of engineering students has been put together to develop a scaled down prototype of a new electric motor with some of the same operating characteristics of the E-Fan X.

This machine is going to have an external rotor (ER) configuration, which has both significant advantages and disadvantages over more conventional, internal rotor designs. The team of students, consisting of electromagnetic, structural and thermal engineers, will eval-

[17] Dalløkken 2017.
[18] Rolls-Royce 2019.
[19] Airbus 2019.
[20] Airbus 2018.
[21] Airbus 2020; Dalløkken 2020.

uate the concept. While the two former aspects is covered in other reports,[22] this thesis will mostly focus on the heat generation from power losses and the design of necessary cooling systems in order to keep an acceptable operating temperature. The research is mainly focused on the case in question, but it is believed that the considerations taken in this analysis will be applicable to other compact, high power electrical machines as well.

1.3 Preliminary Work

This thesis relies heavily on previous work done by Rolls-Royce, presenting the general characteristics of the electric machine, as well as initial studies conducted by the engineering students team at NTNU (electromagnetics,[23] structural[24] and thermal[25]), where the goal was to create a multiphysics model of the entire machine to study its behaviour. The idea being that since all aspects interfere with one another, the cooperative expertise will help achieve a more optimal and feasible design. The following report follows closely on the initial collaboration and expands upon this work.[26] On the other hand it is important to note that the focus in this specific thesis lies in the thermal management and does not extensively cover the other topics, but can be studied both together with and separate from the other team members' studies.

Included in the first thermal study is a proposed thermal management system for the prototype machine based on 2D finite element (FE) analysis in COMSOL[27] Multiphysics. The suggested cooling system proved capable of sufficiently cooling the motor, keeping the hot-spot temperature below the material limits.[28]

1.4 Task

The following work expands upon the initial thermal study of the motor, discussing alternative cooling methods and practical considerations when working on such a multidisciplinary project. The report's main concern is the cooling of the electric machine given the limited available space for heat exchange, and the dense heat generation due to the internal losses. Meanwhile, the thermal management system must be in line with the low-weight, high specific power requirements of electrical aircraft motors.

Several potential candidates for cooling systems are presented as options, of which, two different concepts will be integrated into the prototype in a design analysis. First, a closed-loop oil circuit is tested, continuing from the findings of the first study (chapter 3). The

[22] Fossum 2020; Verde 2020.
[23] Fossum 2019.
[24] Verde 2019.
[25] Gjeset 2019.
[26] Fossum 2019; Gjeset 2019; Verde 2019.
[27] COMSOL is a registered trademark of COMSOL inc.
[28] Gjeset 2019.

2D FE model is expanded and previous assumptions are corrected. The ideal mass flow rate is found in order to keep the hot-spot temperatures lower than the critical values, and the temperature fields and cooling channel pressure losses are calculated. A sensitivity analysis is also performed.

As an alternative to the oil-cooled TMS presented initially, an air-cooled concept is evaluated (chapter 4), looking at the possibility of cutting weight by constructing an open-loop configuration. A similar FE simulation model is made, and a numerical analysis of turbulent air convection in the rotor-stator air gap has been executed, comparing with established experimental results and correlations.

The two options are compared according to their ability to provide suitable machine operating temperatures (chapter 5). Advantages and disadvantages are also evaluated, such as their general characteristics, weight and practical applications. Since no real version of the machine exists, and since in any case the purpose of it would be for a laboratory test rig, the actual mass, robustness and in-flight operation are not studied, but merely mentioned as a consideration.

Ultimately, the main goal of this thesis is to use the prototype electric motor as a case study to highlight different aspects in thermal design and present specialized cooling systems. An experimental test setup was planned in order to calibrate and validate the numerical results, as well as obtain valuable practical experience. The experiments themselves, however, have been postponed due to the outbreak of COVID-19.

Extending the study, a deeper analysis has also been done on the bulk heat transfer properties of electrical windings (chapter 6 & 7). This type of small-scale, multi-material component is challenging to implement in its entirety in a complete 3D numerical model of the machine, and a preferred method is to use a lumped-element homogeneous material in its place. Several homogenization techniques are presented and screened against a simplified FE model.

Chapter 2

General Considerations

In an internal combustion engine, the main contributor to heat generation is the combustion process, happening in a limited space, typically a combustion chamber, where components affected by this are thoroughly engineered in order to withstand the high temperatures. Meanwhile, the heat generated by the electric motor has contributions from many different physical phenomena, and occur more uniformly distributed. A lot of the material characteristics (plastics, magnets, copper) are highly temperature dependent and/or they cannot withstand high temperatures. For this reason, proper thermal management of the machine, understanding the electromagnetic and thermophysical phenomena to create efficient cooling systems is vital for the overall performance.[1]

2.1 Electrical Outrunner Machines

The two main components of an electrical machine is the rotor and the stator. In a permanent magnet motor the stator will consist of a stationary armature; an iron core with teeth, each separating a stator slot, where conducting wires are placed, winding around the teeth. The rotor is a set of permanent magnets on a mount which will rotate due to the electromagnetic forces that occur when current is passed through the winding wires (figure 2.1).[2,3]

2.1.1 Internal vs. External Rotors

One way to categorize different motor geometries is the relative location of the rotor and stator. As shown in figure 2.1, there exists inrunners, where the magnets are located concentrically inside the stator armature, and outrunners, which are the inverse of inrunners.

[1] Yang et al. 2016.
[2] RClab 2014, URL: http://www.rclab.info/2014/01/the-basics-of-electric-power-brushless.html.
[3] Hanselman 2006.

While they both achieve the same output, namely rotation and torque, their performance differ due to their distinct configurations.

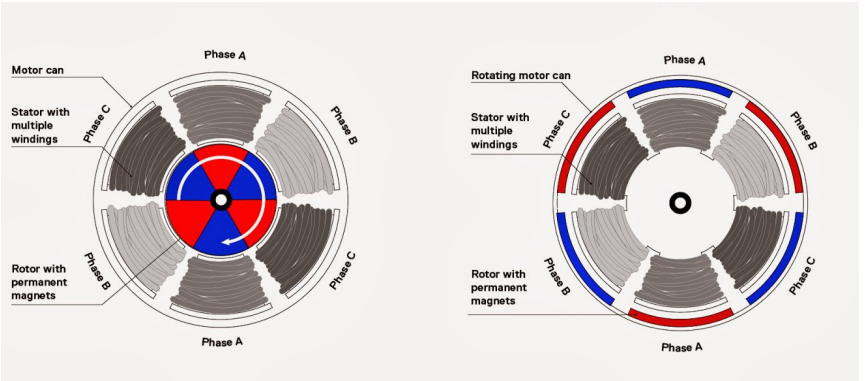

Source: RClab 2014.
Figure 2.1: Permanent magnet machines; inrunner (left) and outrunner (right).

As a rule of thumb, outrunners generate higher torque as an equally sized inrunner, due to the greater moment of inertia, resulting in a higher power-to-weight ratio.[4] External rotor (ER) motors may, however, be difficult to manufacture, and prove difficult to cool adequately, as hot-spots are more difficult to reach and there is less space for cooling systems.[5] This is due to the fact that a major contribution to the losses, and thus the heat generation and temperature rise, are the joule losses from the resistance within the conducting wires. In a permanent magnet machine, this happens in the stator, and since an outrunner has this placed in the center, it becomes more complex to duct this heat out of the motor.[6]

2.1.2 Prototype Machine

The prototype machine to be studied is a small scale outrunner motor. The main specifications are listed in table 2.1, and a concept sketch is shown in figure 2.2. It is designed for high speed an power density, acting as a demonstrator for larger electric aircraft motors. The performance characteristics are given by the initial electromagnetic sizing analysis.[7]

As figure 2.2 and table 2.1 indicate, the motor consists of a stator in the center with 72 slots in which the electrical windings are placed. Around this, a ring of permanent magnets supported by a steel casing will rotate, generating torque. Not shown in figure 2.2 is that the outer structure will wrap around each end of the structure to be supported by bearings at

[4] Christie, Dubois, and Derlaga 2017; Duffy et al. 2018.
[5] Hanselman 2006; RClab 2014.
[6] Gjeset 2019.
[7] Fossum 2019.

either end of the support tube. Effectively, the inner components in the assembly are sealed within a rotating drum. The full description of the components and the structural analysis are found in the mechanical reports.[8]

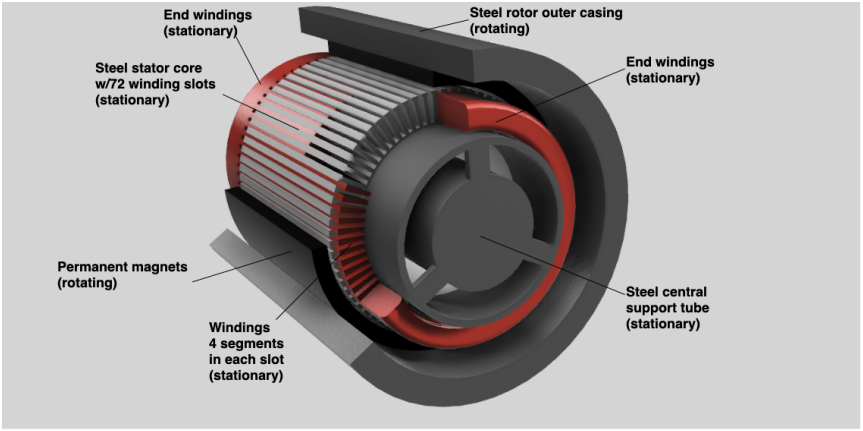

Figure 2.2: External rotor prototype machine concept.

Parameter	Value
Motor type	Internal stator External rotor Permanent magnets 72 Slots
Rated power	250 kW
Rotational speed	15 000 rpm
Torque	160 Nm
Inner stator diameter	116 mm
Outer Stator diameter	170 mm
Inner rotor diameter	174 mm
Outer rotor diameter	194 mm
Active length	160 mm
Max stator temperature	∼220 °C
Max rotor temperature	∼90 °C

Table 2.1: ER prototype; main specifications.

As the machine operates, losses are generated within the different segments. Different mechanical and/or electromagnetic phenomena contribute to the heat generation, and will eventually increase the temperatures.[9] As noted in table 2.1, the plastic in the winding insulation and the magnets are the most sensitive components, and they will eventually fail

[8] Verde 2019; Verde 2020.
[9] Fossum 2019; RClab 2014.

if they are kept above the tabulated limits for an extended period of time.[10]

The losses are tabulated below (table 2.2), collected from the initial electromagnetic performance analysis.[11] In order to account for potential calculation errors, the loss values have been rounded up to ensure more conservative results. Figure 2.3 displays each contribution to the total, where it can be seen that the stator provides more than 90%.

Parameter	Value
Stator iron loss	3000 W
Stator winding loss	1500 W
Total stator loss	4800 W
Magnet & sleeve loss	130 W
Windage loss*	200 W
Total rotor loss	330 W
Total loss	4830 W
Efficiency	∼98 %

Table 2.2: Electric engine internal losses @ operating conditions.
* Further discussed in section 4.1.3.

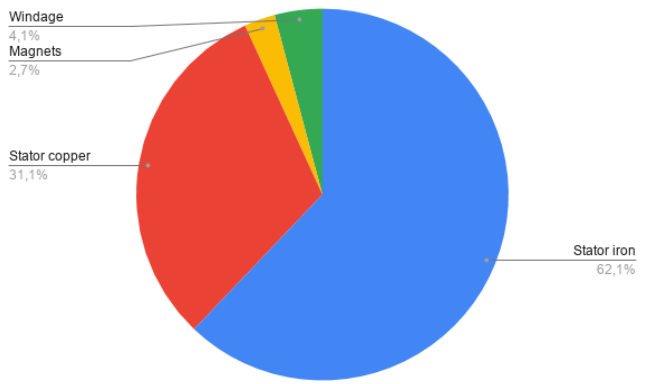

Figure 2.3: Breakdown of the total losses.

To summarize, the motor consists of an inner structure generating a large amount of heat, surrounded by a steel drum rotating at high speed. If left running for a long period of time, the heat will cause the temperature to rise above the materials' critical limits, causing machine failure. There is need for a thermal management system (TMS) to cool down the

[10] Gjeset 2019; Yang et al. 2016.
[11] Fossum 2019.

structure, which has to fit into the confined space between the stator and the rotor.

In order for the motor to perform properly, all of the aspects; structural, electromagnetic and thermal engineering have to be integrated and optimized. This is true for all electric machine design, but is even more evident when working with such compact constructions as this ER prototype. The limited amount of space available requires proper evaluation of the effectiveness of every component, in some cases demanding multiple functions of the same part.

This thesis will focus on enhancing the heat transfer out of the machine through a cooling system, but the design of the TMS is not isolated from the other aspects. The final machine design is done in cooperation between all the team members in the project, and this report can be studied both together with and separate from the other team members' studies.

2.2 Thermal Analysis

The general characteristics and sizing of an ER machine has been presented based on ideal electromagnetic models (tables 2.1 & 2.2) and the surrounding structure has been created from a mechanical analysis.[12] Using this given data, a thermal management system (TMS) will be created to remove the heat and ensure stable and acceptable operating temperatures. The proper sizing and composition of the TMS is found using thermal analysis models, for which the theory is briefly presented in the following section. Unless otherwise specified, the expressions are collected from *Principles of Heat and Mass Transfer*.[13]

2.2.1 Theory of Heat & Momentum Transfer

An electric motor constitutes of different, more or less complicated geometries and materials which combined have to be kept below a certain temperature. In this case, the limiting components are the insulation ($T_{max} = 220°C$) and the neodymium magnets ($T_{max} = 90°C$).[14] All the while, the machine itself generates a constant volumetric heat rate, $\dot{q}$, corresponding to the losses tabulated in 2.2 within their respective segments. As a result, the temperatures will rise within the construction, yielding a distributed temperature field. The magnitude and distribution will vary based on the governing equation, the heat diffusion equation (2.2), based on Fourier's law (2.1):

$$q'' = -k\nabla T \tag{2.1}$$

$$\dot{q} = -k\nabla^2 T \tag{2.2}$$

Where q'' is the heat flux at some point in the machine and k is the material's thermal conductivity at that point.

[12] Fossum 2019; Verde 2019.
[13] Incropera et al. 2013.
[14] Gjeset 2019; Yang et al. 2016.

The partial differential equation (2.2) can be solved in finite element (FE) software to display the steady state operating temperature field, considering a constant value, k, for each material and a given distributed volumetric heat generation, $\dot{q}$. The calculation results will give the temperature and location of eventual hot spots.

However, some boundary conditions are required in order to solve equation (2.2), For which two possibilities exist:

1. Dirichlet: $T = \text{constant}$
2. Neumann: $-k\nabla T = q''$

The model is set up in such a way that only case 2. needs to be considered. This is because each outer interface is either perfectly insulated ($q'' = 0$) or interacts with a convective fluid flow, where Newton's law of cooling can be applied:

$$q'' = h(T_s - T_b) \tag{2.3}$$

h is the flow's convection coefficient, T_s is the channel surface temperature and T_b is the fluid bulk temperature. In short, equation (2.3) calculates a fluid's ability to transfer a certain rate of heat to or from a surface it interacts with. The flow in question is the cooling flow through the cooling ducts. This implies that good choices have to be made to ensure that the parameters of equation (2.3) are sufficient and the maximum motor temperature does not exceed the material limits.

The heat convection coefficient used in equation (2.3) is a parameter dependent on geometry, fluid properties and temperature. It is often described by the non-dimensional Nusselt number, defined as follows (for an internal flow):

$$Nu = \frac{hD_h}{k} \tag{2.4}$$

Where D_h is the hydraulic diameter of the cooling channel:

$$D_h = 4 \cdot \frac{\text{Flow CS area}}{\text{Flow CS perimeter}} \tag{2.5}$$

And k is the fluid's thermal conductivity. The value and/or function for the Nusselt number is often specific to each geometry and flow/heat transfer scenario. These are described later, at the point at which they are applied.

Since this TMS utilizes fins as a means of extending the surface area and increasing heat transfer, the fin efficiency, η_{fs}, provides a method of analyzing the surface extension's performance:

$$\eta_{fs} = \frac{\dot{Q}_{if}}{hA_{fs}(T_{fb} - T_b)} \quad , \quad \eta_{fs} \in [0, 1] \tag{2.6}$$

The definition is such that the actual heat transfer from the total surface is compared to the ideal case in which the entire fin surface(A_{fs}) is at the fin base temperature (T_{fb}). A

drastic decrease in the surface temperature along the fin will diminish the efficiency.

Alternately, a measure for the overall increase in heat transfer caused by adding the surface extensions can be calculated from the fin effectiveness, ϵ_{fs}:

$$\epsilon_{fs} = \frac{\dot{Q}_{if}}{hA_0(T_{fb} - T_b)} \tag{2.7}$$

Where A_0 is the original surface area without the added fins. If η_{fs} or ϵ_{fs} is sufficiently low, the geometry should be revised or the fin be removed altogether.

Since the fluid flowing through the cooling channels will constantly receive heat from the machine, following equation (2.3), the temperature will rise within the fluid itself. This will lead to an flow-axial evolution of the fluid bulk temperature, T_b, governed by the following equation (in this case considered for a flow parallel to the z-axis):

$$\frac{d\dot{Q}}{dz} = \dot{m}c_p\frac{dT_b}{dz} \tag{2.8}$$

Where $\dot{m}$ is the mass flow rate and c_p is the fluid's specific heat capacity.

The frictional losses and subsequent pressure drop caused by the flow has to be compensated by some pump or fan of feasible and/or economical size. As such, the best option is to keep ΔP as low as possible. The numerical value can either be analyzed directly from software or it can be calculated through the use of a friction factor, C_f:

$$\Delta P = 2C_f\frac{L_A}{D_h}\rho V^2 \tag{2.9}$$

Where V is the average flow velocity through the duct.

Lastly, it is necessary to define three additional non-dimensional numbers used in both the thermal and fluid dynamic analysis. These will be used later in correlations related to the physical models. The firs is the Reynolds number, relating to the flow structure:

$$Re = \frac{VD_h}{\nu} \tag{2.10a}$$

ν and μ is the fluid's kinematic and dynamic viscosity, respectively. For internal flows, it is common practice to assume laminar flow conditions as long as $Re < 2300$.[15]

In some cases of rotational flow, it is common to use the Taylor number instead of the Reynolds number to define the flow:[16]

$$Ta = \frac{\omega^2 D_{Ri}\delta^3}{2\nu^2} \tag{2.11}$$

[15] Çengel and Cimbala 2010; Incropera et al. 2013.
[16] Childs 2010.

Where ω is the angular velocity.

The Prandtl number indicates the relation between diffusion of heat versus momentum, and is commonly used in convection calculations and correlations as a material property of the convective fluid:

$$Pr = \frac{\mu c_p}{k} \tag{2.12}$$

As will be shown later, many of the important flow characteristics, such as friction factors, C_f/C_w, and Nusselt numbers, Nu, can be derived from the non-dimensional parameters through correlations. These expressions are often case specific, and will be described at the point at which they are used.

$$Nu = f(Re, Ta, Pr, ...) \tag{2.13}$$
$$C_f = f(Re, Ta, ...) \tag{2.14}$$
$$C_w = f(Re, Ta, ...) \tag{2.15}$$

2.2.2 Thermal Model Input

Having established the necessary physical relations for the thermal analysis, the design of the TMS can be created and evaluated considering the underlying principles. As described in section 2.1.2, the base composition of the prototype is given, the main geometric parameters listed in table 2.1. Figure 2.4 shows a $\frac{1}{9}^{th}$ fraction of the radial cross section, and figure 2.5 shows the electrical winding "block", which will be discussed in further detail in chapters 6 and 7.

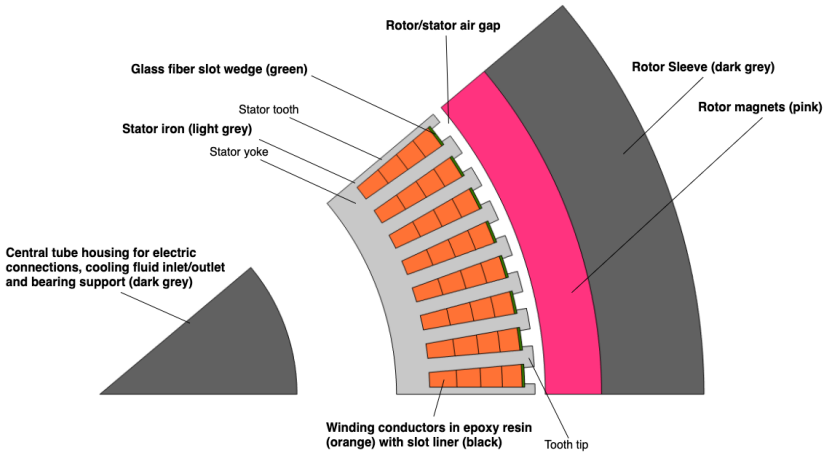

Figure 2.4: $\frac{1}{9}^{th}$ of the base design (radial cross-section).

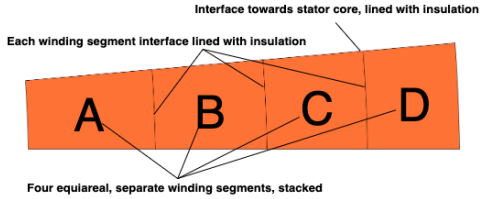

Figure 2.5: Detail of the electrical winding.

As a starting point, this ”base composition” should not be altered, as it could potentially compromise the structural integrity and/or motor performance. This applies to any area in figure 2.4 which is colored. This leaves little space left to implement the cooling system, which is often the case when creating an outrunner machine.

The composition and materials of the electric machine is considered to remain constant throughout the analysis, and are given in tables 2.1, 2.3 and figures 2.4 and 2.5. The losses and heat generation will neither change (table 2.2).

Some of the parameters presented in table 2.3 are uncertain, either due to the fact that some material choices not being final in the actual prototype design, or that there is some inherent variation in composites. The tabulated values are in any case characteristic and are readily interchangeable for later iterations of the machine.[17]

In table 2.3, there are also listed some thermal contact resistances, $\mathbb{R}''$. These are due to imperfect contact faces between separate components and/or very thin insulation layers. It generally relates to the following equation:

$$\mathbb{R}'' = \frac{\Delta T}{q''} \tag{2.16}$$

The winding interface contact resistance corresponds to a 0.5mm ”slot liner” consisting of an insulation material with a poor thermal conductivity of 0.1 $\frac{W}{mK}$. This resistance is applied to the entire winding/stator slot boundary, as well as between the individual winding segments.

$$\mathbb{R}''_W = \frac{t}{k} \tag{2.17}$$

Where t is the insulation thickness.

[17] Cousineau et al. 2015; Elghnam 2014; Incropera et al. 2013; Kristjanson 2019; Saripally 2015; Staton, Boglietti, and Cavagnino 2003; *Characteristics of NdFeB Magnets*.

Parameter	Value
Copper conductor, k_C	385 $\frac{W}{mK}$
Varnish insulation k_I	0.26 $\frac{W}{mK}$
Epoxy encapsulant k_E	0.85 $\frac{W}{mK}$
Winding longitudinal,* $k_{W,\lambda}$	∼150 $\frac{W}{mK}$
Winding transverse,* $k_{W,\tau}$	∼1.6 $\frac{W}{mK}$
Winding interface, $\mathbb{R}''_W$	5.0×10^{-3} $\frac{m^2K}{W}$
Laminate steel, longitudinal, $k_{L,\lambda}$	1.6 $\frac{W}{mK}$
Laminate steel, transverse, $k_{L,\tau}$	25 $\frac{W}{mK}$
Glass fiber slot wedge/casing, k_{gfib}	0.4 $\frac{W}{mK}$
Neodymium magnets, k_{mag}	9 $\frac{W}{mK}$
Steel casing, k_{st}	44.5 $\frac{W}{mK}$
Magnet/steel interface, $\mathbb{R}''_R$	2.0×10^{-4} $\frac{m^2K}{W}$
Convective heat transfer from rotor, h_{Ro}	40 $\frac{W}{m^2K}$

Table 2.3: Electrical machine thermal model input.
* Further discussed in chapter 7.

2.3 Cooling Concepts

Electrical machine performance is often limited by the material temperature limits (commonly the insulation plastic or the magnets), requiring a capable cooling system to conduct the heat from the losses out of the structure.[18] In order to achieve the necessary heat transfer, some components are typically needed, such as cooling ducts, fins, and ventilation holes. However, as has been noted previously, this construction is compact, and there is limited space in which to add more parts. Referring back to figure 2.4, most of the machine is already occupied by either the stator, rotor or support structure. There are, however, two ”free areas” available:

- The annulus between the stator yoke and the central support tube
- The air gap between the stator and the outer rotor

These areas are also commonly referred to in this paper as the inside (annulus) and outside (air gap) domains.

The losses are focused in the stator, which is enclosed within the rotor drum. The most efficient way to remove the heat generated is to duct it out through forced convective heat transfer, letting a fluid (gas or liquid) flow through the machine, absorbing the heat and transporting it outside. This has to be achieved at a decent rate so that the temperatures are kept below the specified limits, while the cooling system itself has to fit the space and

[18] Tüysüz et al. 2017; Yang et al. 2016.

weight restrictions for the application. Multiple configurations exist, based on the principles of heat transfer and compact heat exchange,[19] and many specific methods applicable to electric machines have been presented through research.[20]

Generally, the following the following concepts are worth considering when constructing the thermal management system (TMS):

I. Geometry of the fluid cooling channel
   (a) Shape
   (b) Surface area
   (c) Location in relation to heat generation
   (d) Circuit

II. Cooling fluid
   (a) Phase/phase change
   (b) Motion

III. Temperature gradients
   (a) Inflow temperature
   (b) Fluid heating

Considering I., one main way to categorize the cooling structure is whether it is an open or closed loop configuration (ref. I.d). As demonstrated by the left section in figure 2.6, an open cooling system will draw in some fluid, commonly air, and pass it through a heat sink inside the machine. Here, the coolant will be heated following equations (2.3) and (2.8), before it is expelled.

A closed loop will operate on the same principle as the open, namely taking in some coolant, exchanging heat and passing the heated fluid. The main difference is what happens in front of and after the flow passes the motor: The ”closed” in closed loop implies that nothing is supposed to leak in or out of the system, and the ”loop” suggests that a cycle exists to link the inflow and outflow. In order to achieve this, a series of ducts and pumps are used to pass the fluid through the system, as shown in the right field of figure 2.6. Since the coolant will heat up following relation (2.8), it must be cooled down before re-entering the machine, which is why a secondary heat exchanger (SHE) is needed.

In effect, the open loop will let the machine exchange heat directly with some surrounding fluid, while the closed loop extract the heat from the motor, allowing it to be removed by the secondary heat exchanger at a more convenient location. The reason they are referred to as ”air cooled” and ”liquid cooled” in figure 2.6 is because the open structure relies upon

[19] Incropera et al. 2013; Kays and Crawford 1993.

[20] Christie, Dubois, and Derlaga 2017; Demerdash, Garg, and Hamilton 1975; Fabbri 1997; Fabbri 1998a; Fabbri 1998b; Fabbri 2000; Guechi et al. 2013; Huang et al. 2012; Karim and Yusoff 2014; Popescu et al. 2016; Vlach, Grepl, and Krejci 2007; Yang et al. 2016.

a large reservoir of coolant, since there is no recycling of the flow, and as such they are more suitable for air cooling, as the gas is readily available in the surrounding atmosphere. Meanwhile, liquid cooling configurations typically have a fixed volume of fluid running through the loop exchanging the heat between the two stations.

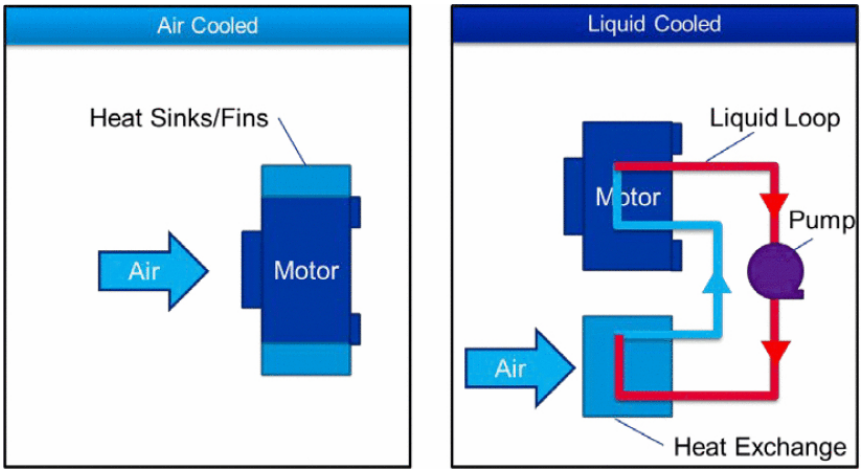

Source: Duffy et al. 2018.
Figure 2.6: Typical schemes of open-loop (left) and closed-loop (right) motors.

The positioning of the cooling system within the machine have to be optimized to ensure a stable and robust design considering I.a, I.b, I.c and II. fitting inside the available space. Possible options are:[21]

A. Axial flow ducts passing through one or both of the available domains

B. Axial flow ducts through stator disk and/or winding slots

C. Liquid cooling jacket

The choice of either relates to the possible advantages and disadvantages regarding direct and indirect cooling (ref. I.c). The logic behind is simple: if the heat sink, i.e. cooling channels, is closer to the source of the heat generation, smaller temperature gradients, and thus lower overall temperatures are found in the motor. On the other hand, indirect cooling systems are easier to create, as they interfere less with the already existing structures.[22]

The extremes are either B., placing the channels inside the stator itself, closest to the hottest components (windings) or C., constructing a separate component located at a more convenient section (e.g. the annulus) where there is enough space. Cooling jackets are typically employed as off-the-shelf solutions for machines which have already been optimized considering the electromagnetic and mechanical aspects, since they can be constructed fully

[21] Karim and Yusoff 2014; Tüysüz et al. 2017.
[22] Tüysüz et al. 2017; Yang et al. 2016.

decoupled from the rest of the design process.[23] This benefit is at the expense of efficient heat transfer, as the heat sink is located further away from the source. As a consequence, these systems are often heavier, and for this reason, the concept is not applied to the current prototype.

Conversely, direct cooling will often imply removing material from the stator, which in turn may negatively affect the electromagnetic performance.[24] As such, the effect of overheating and good thermal management must be weighted against the machine requirements and efficiency in a joint optimization study. While the multidisciplinary approach may be better suited for finding the ideal location with regards to both thermal and electromagnetic aspects, the process requires better understanding of both phenomena as well as better cooperation between the engineers. As this thesis is more focused on the thermal analysis, this method is left for further work.

However, the first option, using the already available space proves a good alternative, showing some of the characteristics of both direct and indirect cooling. For one, the outer domain is fairly close to both the stator slot and the rotor magnets. The electrical windings provide a large amount of the total losses, while also being difficult to reach and susceptible to high temperatures. The magnets, directly opposite the windings, consist of the most temperature sensitive material in this machine. It is therefore beneficial to locate a heat sink close to these components. Meanwhile, the annulus on the inside has a relatively large volume compared to the outside, and fins can be attached to the inner surface, further expanding heat exchange area for the bulk removal of heat.

Finally, there is also a possibility of combining the two spaces, linking them either in parallel or in series. After all, though the heat generation is focused on specific components, the overall losses are relatively distributed within the stator, and adding multiple heat sinks should improve both the control of hot spot temperature and minimize temperature gradients while keeping the operating cost (pump/fan power) low.[25]

Based on the considerations made above, combining the geometry (I.) and fluid (II.) creates two possible options for cooling the motor:

1. A closed loop, oil cooled thermal management system using a series arrangement

2. An axial, open loop air flow running in parallel through each of the cavities

These two alternatives are the ones further described and analysed in later sections, comparing the advantages and disadvantages of the coolant fluid and the open or closed configuration. Some evaluation is also made on the arrangement and location of the cooling channels in the systems.

[23] Tüysüz et al. 2017.
[24] Demerdash, Garg, and Hamilton 1975; Tüysüz et al. 2017.
[25] Huang et al. 2012; Tüysüz et al. 2017; Vlach, Grepl, and Krejci 2007.

Other, possible cooling methods which are not implemented into this machine, but may be considered in future TMS designs include:[26]

C. Solid/liquid phase change material for increased cooling at start-up (e.g. take-off)

D. Spray-cooling of end windings (evaporative or constant phase)

E. Ferrofluids, micro-channels, piezoelectric fans and other exotic cooling schemes

Though both C. and D. are viable options for this design, the added complexity in both the analysis, manufacturing and integration of the systems is considered high compared to the efficiency. The same applies to E., as new and experimental configurations require deeper studies into the underlying mechanisms. The present study aims to investigate the prototype compact electrical machine, creating an efficient thermal management system capable of ensuring stable operating conditions. As a starting point, more well established methods such as forced convection cooling through axial ducts will be studied, and other alternatives are left for further work.

The same argument applies to more passive methods for improving existing TMS designs:[27]

- Cooling fin/channel geometry optimization
- Graphite sheets between laminations functioning as heat pipes
- Better heat conducting material choices in stator and/or windings

While these options prove interesting concepts for optimizing the thermal design, these plans are left as optimization tools for constructing more efficient TMS at later development stages.

The configurations mentioned in this section demonstrate some examples of components in different thermal management systems. Though they will not be further discussed in this report, they prove the wide range of possibilities to consider and the complexity in designing the proper system for weight, power and effectiveness optimization.

Following the decisions of evaluating and comparing two separate TMS concepts, the models for either must be constructed for the analysis. This thesis is a continuation of the initial project work, where the basic design for the oil TMS has been laid down and a first iteration of the thermal analysis has been performed.[28] The current study will further expand upon the original model for the liquid cooled configuration. In total, three iterations of this system has been or will be created and studied:

[26] Ayat et al. 2019; Guechi et al. 2013; Huang et al. 2012; Tüysüz et al. 2017; Vlach, Grepl, and Krejci 2007; Yang et al. 2016; Yi and Haran 2019; Zhang et al. 2018.

[27] Fabbri 1997; Fabbri 1998a; Fabbri 1998b; Fabbri 2000; Guechi et al. 2013; Incropera et al. 2013; Kays and London 1984; Yang et al. 2016.

[28] Gjeset 2019.

I. Initial Thermal Model (ITM) iteration: the first design of the TMS and performance analysis described in the previous report[29]

II. Oil Correlation Model (OCM) iteration: the second version of the oil TMS with updated geometry and values, analysed with the same methods as the ITM

III. Oil COMSOL Model (COM) iteration: an updated numerical representation of the same configuration as the OCM.

The second alternative, the open-loop air TMS, has not been considered earlier, and a basic assessment will be performed in this study to give insight to the possible options with potential benefits and drawbacks.

IV. Air Correlation Model (ACM) iteration: an alternative TMS using ambient air as coolant, modelled through FE analysis and correlations

The systems will be described in the following sections (2.3.1 & 2.3.2), while the performance analysis is done in the subsequent chapters (3 & 4). A final comparison and some additional considerations are put forth in chapter 5.

2.3.1 Oil Configuration

Based on the already existing components and the space left for cooling systems, it was decided that two separate cooling channels should be used:[30] An annular, finned duct on the inside of the stator with the fins as an extension of the stator back iron (yoke), and a set of small, rectangular channels in the space between the windings, stator tooth tips and an external, glass fiber casing. This is shown in the following figure, 2.7.

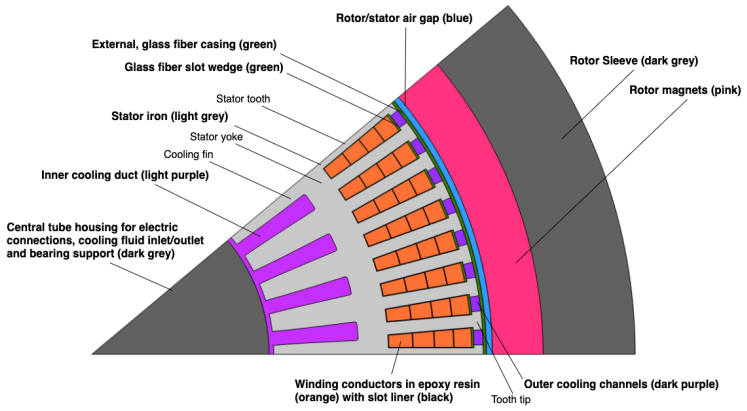

Figure 2.7: $\frac{1}{9}^{th}$ of the simulated, oil cooled motor + TMS (radial cross-section).

[29] Gjeset 2019.
[30] Gjeset 2019.

	W [mm]	**H** [mm]	$\mathbf{D}_h$ [mm]	$\mathbf{A}_c$ [mm^2]
Outer channels	3.2	2.0	2.5	6.4×72
Space between fins	2.0	18.5	3.6	37×36

Table 2.4: Oil cooling channel geometric parameters (approx.).

The initial suggestions were to use a laminar flow of either air or transformer oil as coolant. For simplicity, water has been left out due to its potential corrosive properties, and a liquid/vapor phase change material could be susceptible to failure in the small outer channels if large quantities of vapor blocked the flow gaps. The laminar air flow proved insufficient, and the transformer oil MIDEL[31] 7131 was finally selected, for which the manufacturer has provided the necessary thermal properties.[32] These are listed in appendix A.4.

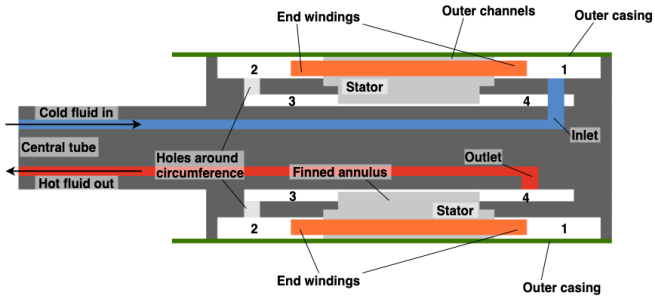

Figure 2.8: Assembly drawing of the oil cooled motor + TMS (axial cross-section).

The two separate conduits (outer channel and inner, finned annulus) are connected to form a closed loop, ”double pass” cooling design with the oil entering at one end into the outer channels and returning through the finned annulus to be collected and returned. This is shown in figure 2.8: The oil enters through a pipe within the central tube and flows into a cavity (#1) which also houses electric connections and end windings. After this, the fluid is passed through the outer channels before reaching another volume (#2), equal to the first one, but where there are holes allowing for the oil to enter the inner annulus with a slightly smaller space (#3). Finally, the medium continues through the inner cooling duct until it arrives at the final chamber (#4) and is let out through the outlet.

The performance of this system has been studied through FE simulation with convection as a boundary condition. Initially, the convection coefficients were found through correlations for fully developed flow from Shah and London.[33] This analysis is more detailed in the first report.[34] Later, the model has been expanded to include non-isothermal CFD.

[31] MIDEL is a registered trademark of M&I Materials Ltd.
[32] MIDEL 2018.
[33] Shah and London 1971.
[34] Gjeset 2019.

These results are discussed in sections 3.1 and 3.2.

2.3.2 Air Configuration

Recent studies of similar motor topologies as the present prototype have been conducted, indicating promising results using an open loop air cooled system.[35] The main advantage is that no secondary heat exchanger is needed, making the system more lightweight and robust. As an added bonus, air is easily accessible from the machine's surrounding atmosphere, and the inflow may be as simple as letting the coolant pass through the motor itself.[36] This is not without its drawbacks, however, as air is a less capable cooling fluid than water or oil, so that a significantly higher mass flow is needed. A pump and filtration system is also needed to supply the air without abrasive particles damaging the machine which also should not impose an excessive drag force on the aircraft.[37]

Considering these factors, an alternative, air cooled TMS (figure 2.9) is presented in chapter 4 and analysed. The goal is to assess whether air is sufficient as cooling medium to remove the heat from the prototype machine in terms of available mass flow and pressure drop. The pump and filtration system is not extensively covered in this report, neither is the air inlet and outlet.

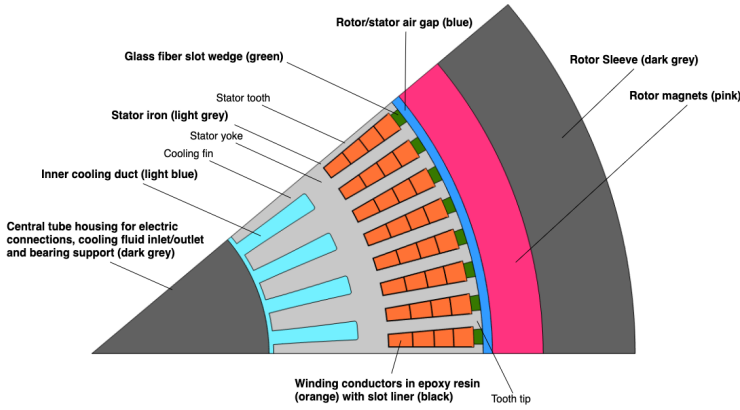

Figure 2.9: $\frac{1}{9}^{th}$ of the simulated, air cooled motor (radial cross-section).

Contrary to the serial connection of the two cooling channels in the oil TMS, this version will split the total incoming mass flow rate and letting it pass in parallel through the ducts, as shown in figure 2.10. The outer partition flows through the air gap between the rotor and stator (as seen in fig. 2.9), where now no outer, glass fiber casing is needed, and the slot wedges are placed in the gap between the tooth tips. The finned annulus is unchanged,

[35] Christie, Dubois, and Derlaga 2017; Yi 2016.
[36] Duffy et al. 2018.
[37] Christie, Dubois, and Derlaga 2017.

and this is where the inner flow will cross. The actual ratio of the split, how much passes through the air gap and the inner annulus, is to be evaluated in the analysis (chapter 4).

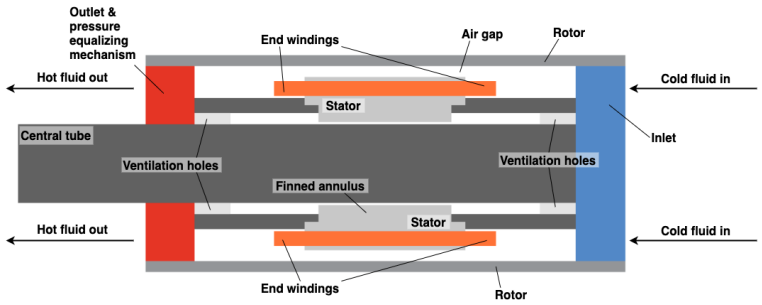

Figure 2.10: Assembly drawing of the air cooled motor + TMS (axial cross-section).

	W [mm]	**H** [mm]	$\mathbf{D}_h$ [mm]	$\mathbf{A}_c$ [mm^2]
Rotor/stator air gap	N/A	2	4	1080.7
Space between fins	2.0	18.5	3.6	37×36

Table 2.5: Air cooling channel geometric parameters (approx.).

Both flows are considered to be turbulent, as it was found in the initial analysis that laminar air flow was unable to provide sufficient cooling.[38] Due to the rotation of the rotor, the air gap flow structure will follow a combination of turbulent Couette-Poiseuille and Taylor flow, the structure of which will affect both the momentum and heat transfer. A separate CFD model is to be set up to study this case.

In addition to monitoring the air gap flow, some consideration must also be given to the axial pressure drop through either conduit. In a series configuration, these pressure losses will simply add up, but since the air TMS uses a parallel structure, the mass flow attempt to divide itself through the two channels balance the pressure through the system, overriding the desired split ratio for optimal thermal performance. In order to counter this, a nozzle may be coupled to one side, equalizing the pressure loss.

The air TMS is presented as a separate alternative to the initial oil cooled design. The overall goal is to find out whether both configurations are capable of ensuring stable operating conditions for the prototype ER machine, as well as analyze their performance in order to draw a comparison of the two. The grounds for this evaluation should be (in prioritized order):

1. Traffic light analysis (is the TMS capable of ensuring sufficiently low temperatures?)
2. Thermal performance (location of hot spots, temperature gradients, safety factor, sensitivity, etc.)

[38] Gjeset 2019.

3. Weight optimization

This thesis does not aim to complete this list, but attempts to either present the results that could be used in the assessment or point out considerations that should be made in the comparison. Though thermal management of electrical machines is not a new field, the performance requirements for the new, high speed, high specific power motors for electric aircraft present the need for more aggressive cooling schemes and a more integrated, multi-disciplinary approach during the design process.[39]

2.4 Compact Machines & Aircraft Considerations

As discussed above, the electrical machine design is made to fit the requirements for large electric aircraft. Though this is only a scaled down prototype, it exhibits many of the features such as compactness and high power output at high speed. One important factor to consider is the total weight of the structure, due to the performance and endurance penalties of the added mass.[40] Eventually, aerodynamic features, such as air intakes for ventilation should minimize additional drag.[41] Lastly, an important factor in any component is safety and robustness, as this is an important factor in most aircraft applications.[42]

The full evaluation of the complete system is a heavy task requiring all of the engineering disciplines to cooperate. This need is further heightened by the strict qualities of electric aircraft machines, opting for a more integrated process and balancing the structural, thermal and electromagnetic components for optimal performance.[43] The following analysis of the TMS and the general machine design is carried out with these considerations in mind.

At this stage in the project, both the specific prototype ER machine as well as similar designs from the literature are still in the early phases of development.[44] As such, more information is needed on the possibilities, limitations and design methods before working on the actual optimization. However, the points raised in this section, as well as other practical considerations mentioned earlier, are important to keep in mind during the advancement of electrical aircraft machines.

[39] Christie, Dubois, and Derlaga 2017; Tüysüz et al. 2017; Yang et al. 2016; Yi and Haran 2019; Zhang et al. 2018.
[40] Hepperle 2012.
[41] Christie, Dubois, and Derlaga 2017.
[42] Christie, Dubois, and Derlaga 2017; Hepperle 2012.
[43] Yi 2016.
[44] Dubois et al. 2016; Duffy et al. 2018; Hepperle 2012; Yi 2016.

Chapter 3

Oil Cooling

An oil thermal management system (TMS) has been described in section 2.3.1. The concept is based on the initial reports,[1] where the inside and outside surfaces of the stator are cooled by running transformer oil, MIDEL 7131, through the inner and outer heat sinks. The full detail of the geometry is detailed in 2.3.1, and the figures are reprinted (figs. 3.1 & 3.2).

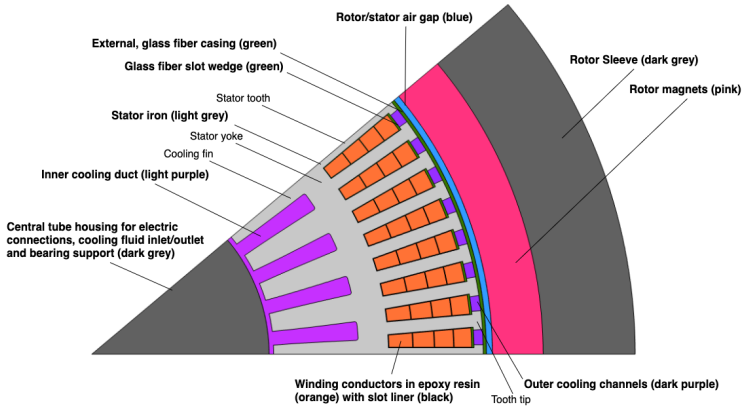

Figure 3.1: $\frac{1}{9}^{th}$ of the simulated, oil cooled motor + TMS (radial cross-section) (revisited).

This report will expand the analysis from the initial reports' correlation model, updating the geometry and creating a new combined FE representation with CFD simulation for the oil cooling channels. Using this new study, further investigation can be done on the TMS performance, and a sensitivity analysis can be conducted.

[1] Fossum 2019; Gjeset 2019; Verde 2019.

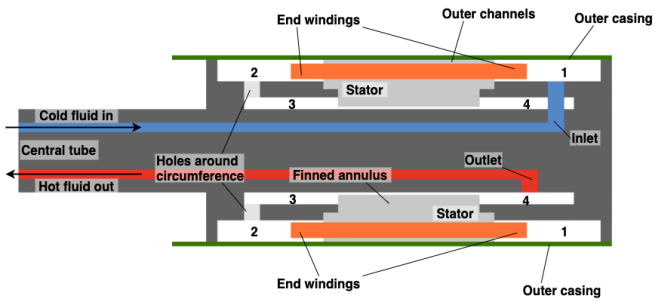

Figure 3.2: Assembly drawing of the oil cooled motor + TMS (axial cross-section) (revisited).

Previous work has shown that the double conduit system with oil as cooling fluid was sufficient to keep the operating temperature below a maximum of $220°C$ with a low mass flow rate of 0.035kg/s. The full description of this analysis is detailed in *Cooling of Electrical Aircraft Machines*.[2] The updated model described earlier in section 2.3.1 uses the same design as previous, though it includes some minor modifications to geometry and assumptions compared to the first analysis:

i. Casing material changed from aluminium to glass fiber

ii. Glass fiber slot wedge added

iii. Winding has been sectioned into 4 equiareal segments

iv. Slot liner removed and replaced with thermal contact resistance

v. Bolt holes removed

vi. Number of fins changed to $\frac{1}{2}$ fin per tooth (36 total) in order to save weight & manufacturing cost

vii. Fins shortened to fit a larger diameter central tube

viii. Updated material properties

k_w calculated from homogenisation techniques (discussed in chapter 7)

These revisions are shown in figures 3.1 and 3.2, and a more detailed breakdown of important geometry parameters are given in tables 2.1 and 2.4 along with heat transfer parameters in table 2.3. A technical drawing of the stator, including measurements, is given in appendix A.3.

[2] Gjeset 2019.

3.1 Correlation-based Study

Based on the method described in the initial report, the new design has been found to behave similar to the original, though the average and maximum temperatures are slightly higher.

The full method description and the calculations of the original TMS performance are not give in this report, but can be found in the previous work.[3] Some of the more important results from the first study are presented in table 3.1, and the temperature distribution plots are included in appendix A.2 for comparison. A brief summary of the updated TMS evaluation follows.

3.1.1 Model Description

The analysis is based on a steady-state FE model of the geometry solving the heat diffusion equation (2.2) using fluid convection (2.3) as boundary conditions for the stator/cooling channel interfaces. In equation (2.3), correlations for fully developed, laminar flow were used to acquire the Nusselt numbers and the subsequent temperature-dependent convection coefficients are calculated through equation (2.13).[4]

The flow heating and bulk fluid temperatures were found using the assumption that the heat generated in each radial cross-section, q', would be taken up by either the inner or outer channels corresponding to a heat split factor, τ:

$$q'_{oc}(z) = \tau(z)q' \tag{3.1a}$$
$$q'_{if}(z) = (1 - \tau(z))q' \tag{3.1b}$$

Where τ would vary linearly from the start to the end of the active length of the motor. The oil temperature increase will relate as follows:

$$\frac{dT_{oc}}{dz} = \frac{q'_{oc}}{\dot{m}c_p} \tag{3.2a}$$
$$\frac{dT_{if}}{dz} = \frac{q'_{if}}{\dot{m}c_p} \tag{3.2b}$$

Lastly, by setting a given flow rate and inlet temperature, the oil axial temperature evolution in both conduits could be calculated in MATLAB[5] and fed into COMSOL[6] Multiphysics to run the total FE simulation. This resulted in an iterative process where the fluid temperature would directly affect the heat transfer and vice-versa. The recursive loop is shown in figure 3.3.

[3] Gjeset 2019.
[4] Shah and London 1971.
[5] MATLAB is a registered trademark of MathWorks Inc.
[6] COMSOL is a registered trademark of COMSOL inc.

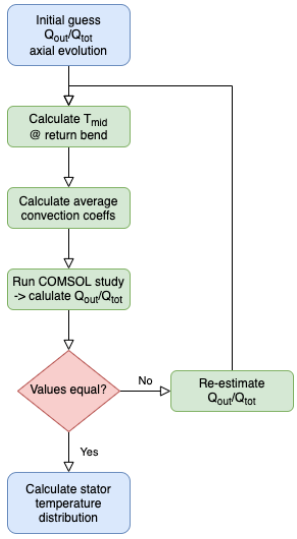

Figure 3.3: Oil-TMS MATLAB-COMSOL solver sequence.

3.1.2 Results

The initial report concluded that a TMS with two cooling channels, inner and outer, with transformer oil as coolant and 72 fins was the most robust design, achieving the lowest maximum stator temperature. The same configuration with half the amount of fins would also be adequate, despite increasing the motor temperature 20.7% compared to the first option. The two systems are compared in table 3.1, and the motor temperature field is shown in appendix A.2, figures A.1 and A.2 for the 1 fin per tooth and 0.5 fin per tooth alternatives, respectively.

The updated model analysis provided the results shown in table 3.2. As can be seen, the TMS is not as effective as initially calculated, due to changes in the model geometry and material properties, though it is still capable of keeping the machine within the material limits. The temperature field is shown in figure 3.4.

The combined FE and correlation study has proved an efficient design tool, as it is able to quickly produce initial estimates for the capabilities of the different configurations. However, it does have its limitations in that it relies on proper established correlations, which have to be selected with respect to flow and heat transfer characteristics and geometry. Proper care also has to be taken to assess the assumptions and simplifications taken in the creation of this model.

Parameter	Value 1 fin per tooth	Value 0.5 fin per tooth
Oil temperature		
Inlet	30°C	30°C
Outlet	90°C	90°C
Mass flow rate	0.035kg/s	0.035kg/s
ΔP	$\sim$400Pa	$\sim$400Pa
Shah and London - Nusselt #		
Outer channels	3.21	3.21
Finned surface	6.41	5.58
Maximum winding temperature	147°C	174°C
Average stator temperature	128°C	165°C
Fin effectiveness, ϵ_{fs}	3.6	4.3
Fin efficiency, η_{fs}	0.45	0.73

Table 3.1: Initially reported cooling system thermal performance.

Parameter	Value
Oil temperature	
Inlet	30°C
Outlet	95°C
Mass flow rate	0.035kg/s
Shah and London - Nusselt #	
Outer channels	3.21
Finned surface	5.45
Maximum winding temperature	202°C
Average stator temperature	176°C
Fin effectiveness, ϵ_{fs}	3.1
Fin efficiency, η_{fs}	0.83

Table 3.2: Updated cooling system thermal performance (correlations).

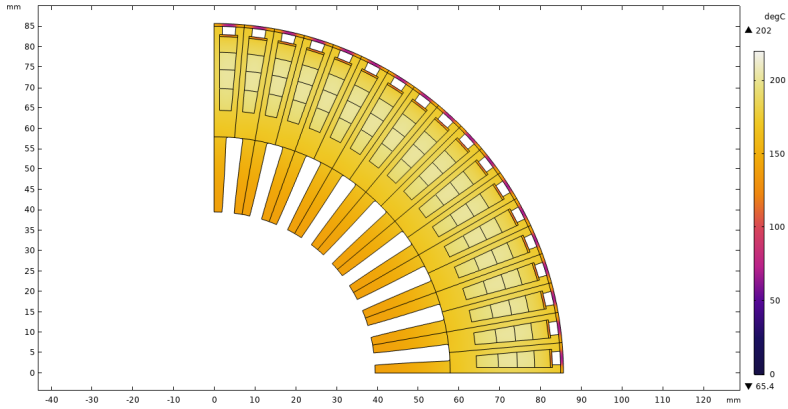

(a) Inlet/outlet section, T_b at inlet temperature and outlet temperature.

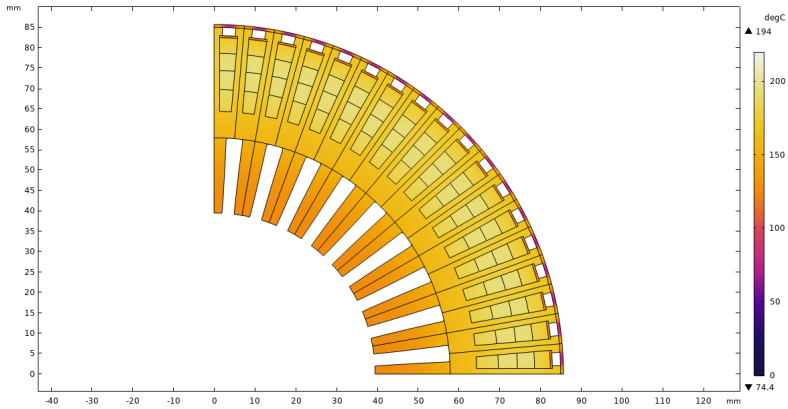

(b) Middle section.

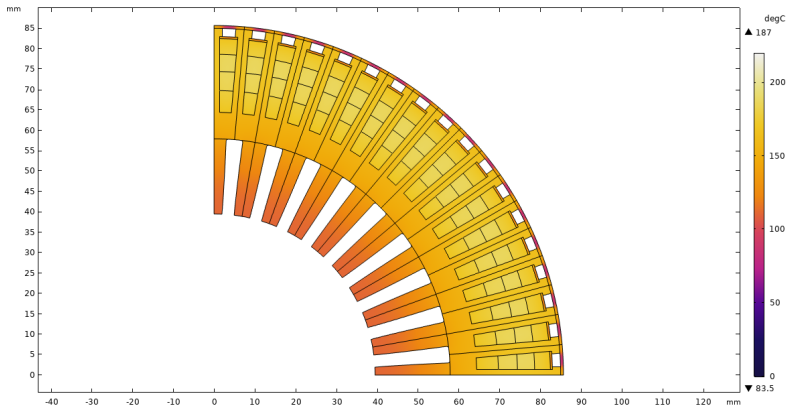

(c) End section, T_b equal on both sides.

Figure 3.4: FEM analysis using axial evolution of h and T_b.

The study was performed using a combination of empirical and analytical expressions for the convective heat transfer and heating of the oil. The main assumptions to form this basis was fully developed, laminar oil flow.

Recalling equation (2.10), the transition to turbulence can be identified by the Reynolds number, where $Re < 2300$ can be considered laminar. Using a average bulk temperature and velocity in the outer and inner channels, the Reynolds number for each segment can be calculated:

$$\begin{aligned} Re_{oc} &= \frac{V_{oc} D_{h,oc}}{\nu} \\ &= \frac{\dot{m} D_{h,oc}}{72 A_{oc} \mu} \\ &\approx 7 \end{aligned} \tag{3.3}$$

$$\begin{aligned} Re_{if} &= \frac{\dot{m} D_{h,if}}{36 A_{if} \mu} \\ &\approx 7 \end{aligned} \tag{3.4}$$

When an isothermal fluid such as the oil enters a heated section, the temperature distribution within will change as a result of the heat transfer. A flow is considered fully thermal developed as soon as the shape of the temperature profile at some axial point and onward does not change.[7] The thermal entry length is the flow-axial length from the inlet until the flow becomes fully developed, and is defined as:

$$\begin{aligned} z_{th,oc} &= Re_{oc} Pr_{oc} \frac{D_{h,oc}}{20} \\ &\approx 250mm \end{aligned} \tag{3.5}$$

$$\begin{aligned} z_{th,if} &= Re_{if} Pr_{if} \frac{D_{h,if}}{20} \\ &\approx 190mm \end{aligned} \tag{3.6}$$

The low Reynolds number is due to the fact that the total mass flow rate (0.035 kg/s) is small, and since it is below the turbulence limit of 2300, the assumption of laminar flow

[7] Incropera et al. 2013.

is valid. However, since the Prandtl number for oil is large ($Pr > 100$), the thermal entry length is greater than the stator active length ($160mm$). The oil does not have enough time to set the temperature profile, leaving to question the simplification of fully developed flow.

As a rule of thumb, the Nusselt number will decrease and converge towards the fully developed Nu-value as the flow evolves. This effect will increase the average estimate, leading to a higher heat transfer coefficient than the one assumed in this study. It is expected that a more complete model will cause the maximum temperature to drop.

3.2 Combined FE-CFD Model

In order to have a numerical model more closely resembling reality, the COMSOL representation was expanded to include the following modifications:

ix. Directional values for thermal conductivity added to windings and stator iron

x. Oil flow correlations replaced with non-isothermal CFD and multiphysics coupling

xi. Rotor added with air gap correlation relating the heat transfer between the rotor and stator

xii. ”Rotating cylinder in air”-correlation added to the outer surface of the rotor

While point ix. will account for the three-dimensional effect of using composite materials, the main advancement lies in point x., using non-isothermal CFD to simulate the fluid flow convection. This enables the model to more accurately capture the cooling channel performance, including phenomena such as entry length and flow heating without having to use separate relations. The coupling done in COMSOL between the FE model for the machine and the CFD calculations for the oil will also automatically relate the heat transfer coefficients, imposing the necessary boundary conditions while solving equation (2.2). It is, however, important to properly define the flow domain and its boundary conditions.

3.2.1 Model Description

The same geometry and flow configuration as for the initial model and the updated one is used. The oil enters the outer channel, marked blue in figure 3.5, flows through and returns via the finned annulus, exiting the red/pink face. The oil chambers described in section 2.3.1, figure 2.8 connecting the inlets,outlets and separate channels are not modelled, as the simulation only covers the active length of the stator/rotor configuration. Instead, the average temperature at the outer canal outlet is kept and set as an inlet condition at the finned side. Otherwise, the incoming mass flow rate is equal to the total of 0.035kg/s at either of the conduits, and the ”back pressure” is set to 0 Pa in order to account for the pressure difference between the inlet and outlet, i.e. the pressure drop through the cooling channels. The upstream fluid temperature is 30°C.

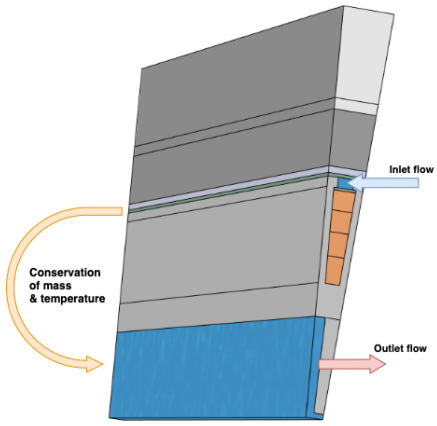

Figure 3.5: Oil TMS COMSOL model geometry with flow boundary conditions.

The coolant is a transformer oil, MIDEL 7131, for which the manufacturer has provided the temperature dependent fluid characteristics and thermal properties.[8] The provided data sheet is found in appendix A.4.

The outer rotor has been implemented into this model. This was not included in the previous analyses. Some of the other previous simplifications were also addressed, such as the convection through the mechanical air gap, windage losses, rotor magnet and sleeve losses. The outer surface of the rotor is assumed to transfer heat to the surrounding air. Correlations were used to estimate the convection coefficient.

Between the stator and rotor is a 2mm air gap. While the stator is stationary, the rotor spins at very high rotational speeds (15 000rpm). The resulting turbulent Taylor-Couette flow will cause convection to be the main mode of heat transfer. Tachibana and Fukui have studied this particular case, and given the following correlation for the Nusselt number:[9]

$$Nu_{ag} = 0.42(Ta \cdot Pr)^{\frac{1}{4}} \tag{3.7}$$

$$k^*_{ag} = \frac{Nu_{ag}}{4} k \tag{3.8}$$

k^*_{ag} is the apparent thermal conduction of the air gap. Since this is an enclosed volume, it can at steady-state be considered as a stationary material. In the COM-model, the air gap is constructed as a solid with k^*_{ag} as the thermal conductivity and a uniformly distributed heat loss from windage (as noted in table 2.2). This is a simplification from the real case, as most of the viscous dissipation will happen closer to the wall, but since these losses are low when compared to the stator heat generation, the adaptation is assumed to have little impact. The air gap itself is not the main focus of this part of the study, but rather its effect

[8] MIDEL 2018.
[9] Fénot et al. 2011; Tachibana and Fukui 1964.

on the temperatures within the magnets of the rotor.

The rotor outer surface is assumed to be in contact with still, ambient air. This type of flow and heat transfer case has also been studied. Elghnam has a correlation:[10]

$$Nu_{Ro} = 0.022 Re_{Ro}^{0.821} \tag{3.9}$$

$$h_{Ro} = \frac{Nu_{Ro} k}{D_{Ro}} \tag{3.10}$$

The convection coefficient, h_{Ro}, relates to the heat transfer between the rotor outer surface and the ambient air, which is considered at 20°C.

3.2.2 Results

The model, as described above, was run through a steady-state, combined CFD-FE numerical solver in COMSOL. The resulting TMS performance and machine temperature field is given in table 3.3 and figure 3.6, also indicating oil flow direction and velocity.

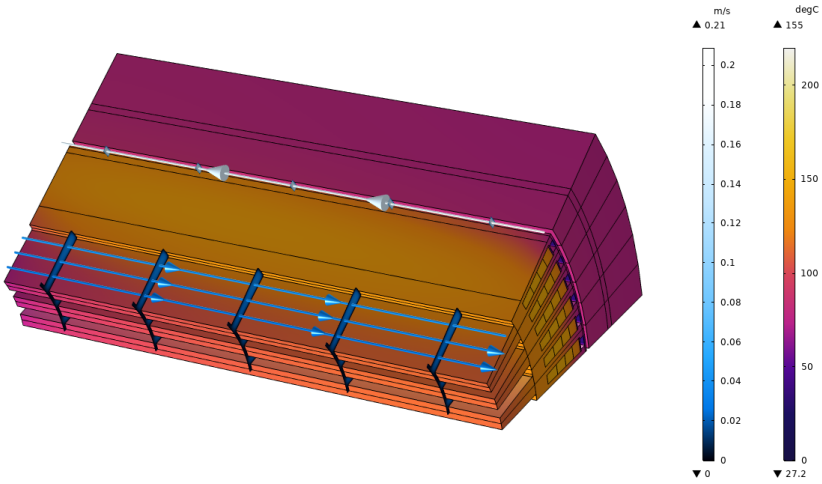

Figure 3.6: COM-model temperature field and oil channel flow analysis. $\dot{m} = 0.05 kg/s$.

As can be observed in table 3.3, the mass flow rate had to be increased to 0.05kg/s as opposed to the previous 0.035kg/s in order to keep the rotor temperature below the material limit. This is due to the fact that the rotor and magnets were not accounted for in the earlier analyses. As a consequence, the pressure drop through the system will increase by ∼45% and the stator winding temperature will drop by ∼12%. The close proximity between the stator windings and the rotor magnets are the limiting factor, as heat is transferred through the air gap.

[10] Elghnam 2014.

Parameter	Value
Oil temperature	
Inlet	30°C
Outlet	90°C
Mass flow rate	0.05kg/s
ΔP	1300Pa
Maximum winding temperature	155°C
Average stator temperature	137°C
Maximum magnet temperature	85°C
Fin effectiveness, ϵ_{fs}	2.9
Fin efficiency, η_{fs}	0.72

Table 3.3: Updated cooling system thermal performance (COMSOL).

Apart from the added limitations, the COM-model behaves similarly to the OCM. Comparing the two at $\dot{m} = 0.035kg/s$, there is a 16% lower maximum winding temperature and a 14% lower average stator temperature in the updated simulation. This is thought to be due to the developing flow being modelled by COM and not in OCM. As shown previously, the thermal entry length is significantly larger than the channel length, implying that this effect should be considered. The increased heat transfer coefficients will also affect ηfs and ϵ_{fs} (ref. equations (2.6) & (2.7)), which is also observed to be lower in COM.

Parameter	Value OCM	Value COM
Oil temperature		
Inlet	30°C	30°C
Outlet	95°C	110°C
Maximum winding temperature	202°C	174°C
Average stator temperature	176°C	155°C
Fin effectiveness, ϵ_{fs}	3.1	2.8
Fin efficiency, η_{fs}	0.83	0.69

Table 3.4: OCM & COM @ $\dot{m} = 0.035kg/s$ comparison.

The more complete COM analysis is shown to give more detailed results than the correlation based study, but this does come at an added computational cost. The design process has become more streamlined by first choosing the geometry through the ITM and OCM studies, while the final calibration and check can be done by a higher fidelity numerical model.

The current configuration with $\dot{m} = 0.05kg/s$ is capable of keeping the machine within its operating field with a margin of ∼5%. This leaves the prototype sensitive to miscalculations and/or simplifications. For this reason, a brief sensitivity analysis is performed.

3.2.3 Sensitivity Analysis

Considering the fact that the model is supposed to replicate a real-world prototype machine, some uncertainties in the assumptions have to be addressed. By observing the variations (mainly on temperature) when modifying certain model parameters will help identify which critical values need to be ensured. This sensitivity analysis will also help assess which parameters are optimal (from a thermal standpoint) to improve when updating the machine design. As it would be time consuming to run this study over all the variables, only a few have been selected, deemed significant in the present model.

a. $\dot{Q}_S$, letting $\dot{Q}_W$ & $\dot{Q}_L$ simultaneously increase $100\% \rightarrow 160\%$

b. $\dot{m}$, ranging $\pm 30\%$

c. L_A, ranging $\in [140, 180] mm$

d. $\dot{Q}_{EW}$, letting $\pm 30\%$ of $\dot{Q}_{winding}$ enter/exit through the winding faces at either end of the stator

e. k_L, letting $k_{L,\lambda}$ & $k_{L,\tau}$ simultaneously range $\pm 30\%$

f. k_W, letting $k_{W,\lambda}$ & $k_{W,\tau}$ simultaneously range $\pm 30\%$

g. $\mathbb{R}''_{W,int}$, ranging $\pm 30\%$

h. $\mathbb{R}''_{R,int}$, ranging $\pm 30\%$

i. T_{amb}, ranging $\pm 5\%$

j. t_R, ranging $\pm 30\%$

	Min param. value			**Max param. value**		
	$\boldsymbol{T_W}$	$\boldsymbol{T_M}$	$\boldsymbol{T_{avg}}$	$\boldsymbol{T_W}$	$\boldsymbol{T_M}$	$\boldsymbol{T_{avg}}$
$\dot{Q}_S$	155	85	137	236	105	189
$\dot{m}$	172	93	155	143	80	128
L_A	166	90	145	146	80	130
$\dot{Q}_{EW}$	141	81	125	179	89	149
k_L	162	85	142	150	85	133
k_W	158	85	138	154	85	138
$\mathbb{R}''_{W,int}$	150	85	134	160	85	139
$\mathbb{R}''_{R,int}$	155	85	137	155	85	137
T_{amb}	155	79	137	155	92	137
t_R	155	85	137	155	85	137

Table 3.5: Sensitivity analysis results. All temperatures in °C

The resulting maximum winding and magnet temperatures, as well as the average stator temperature are tabulated in table 3.5 for the parameter's minimum and maximum values.

Some of the more important findings are graphically represented in figures 3.7, 3.8 and 3.9, while the full list of sensitivity plots are given in appendix A.6.

The study shows that the uncertainties in material parameters have much less effect than the fluctuations in heat generation. The biggest material influence is by k_l with a 12°C difference within the interval. This is mainly due to the fact that this parameter will affect the fin performance, as well as the fact that the laminate steel makes up most of the stator volume.

Since the end windings are not included in the COMSOL numerical model, it is important to bear in mind that this section of the conductors may be a significant source of heat generation, as well as it having good potential for cooling the windings directly, since they are relatively exposed.[11] In the oil-TMS design, this region is considered flooded in oil, and while this will help with cooling, the fluid will be more or less stagnant in these cavities, and their convective capabilities unknown. For this reason, d. simulates the two possibilities: Either the end windings are sufficiently cooled as to impose an axial heat transfer out of the slot, or additional heat is generated and enters the windings at either side. Simulating the end-winding effect seems not to affect the rotor significantly, while the stator is still well within good operating temperatures.

The parameters relating to the largest temperature fluctuations are the ones either directly related to heat generation or TMS configuration. Naturally, increasing $\dot{Q}_S$ or $\dot{Q}_{EW}$ will elevate the entire temperature field, while additional $\dot{m}$ or a longer machine (L_A) will improve the heat sink by either adding more flow or expanding the heat transfer area.

As can be observed from figure 3.7, increasing the heat generation will linearly increase all temperatures. The graph shows that only a $\sim$110% increase will cause demagnetizing and subsequent machine failure. Ignoring this, it is possible to increase over 150% until the insulation limit is reached. This proves to show that the magnets are the delimiting factor in this TMS. If maximum output is desired, it would be advisable from a thermal standpoint to switch this magnet type for one with a higher demagnetizing temperature.

Conversely, adding to the mass flow rate will help reduce the temperature field, though this influence diminishes with increasing $\dot{m}$, as can be seen in figure 3.8a. This is what was done in the COM evaluation to cope with the magnets. Simultaneously, the pressure losses within the outer channels increase (figure 3.8b), requiring larger pumps. Additional weight penalties will also occur due to the added weight of oil and the larger required secondary heat exchanger to cool down the oil, but these considerations are not accounted for. During the $\dot{m}$ sensitivity analysis,it was discovered that as long as the heat flux from the stator to the rotor was approximately 0 or less, the heat transfer from the machine's outer surface would be sufficient to keep the magnet temperature low enough. This is shown in figure 3.9: 3.9a plots the maximum magnet temperature, while 3.9b gives the heat transferred through the stator outer surface, following equation (3.11). Both are evaluated at the same range for $\dot{m}$.

[11] Yang et al. 2016.

$$\text{Air gap cooling} = \frac{q''_{So} A_{So}}{\dot{Q}_S} \tag{3.11}$$

As can be observed, the two functions follow each other closely, and it is not before the heat flux approaches zero that the magnets are sufficiently cool. For an oil mass flow rate of $\sim$0.047kg/s, the stator outer surface is near isolated, and the maximum magnet temperature is $\sim$86.5°C, implying that the rotor assembly is capable of ensuring its own stable operating temperature solely due to the outer surface convection. Further increasing the mass flow rate will effectively absorb some of the windage or magnet losses, further decreasing the temperature. In the COM analysis, 0.05kg/s is chosen in order to have some clearance.

In effect, no heat from the windings should be transferred through the air gap, as this may cause demagnetizing. The outer channels will act as an insulating barrier, or ”heat shield” against the stator losses. This could also be achieved by convection through the finned annulus alone, but this would have been significantly less efficient.

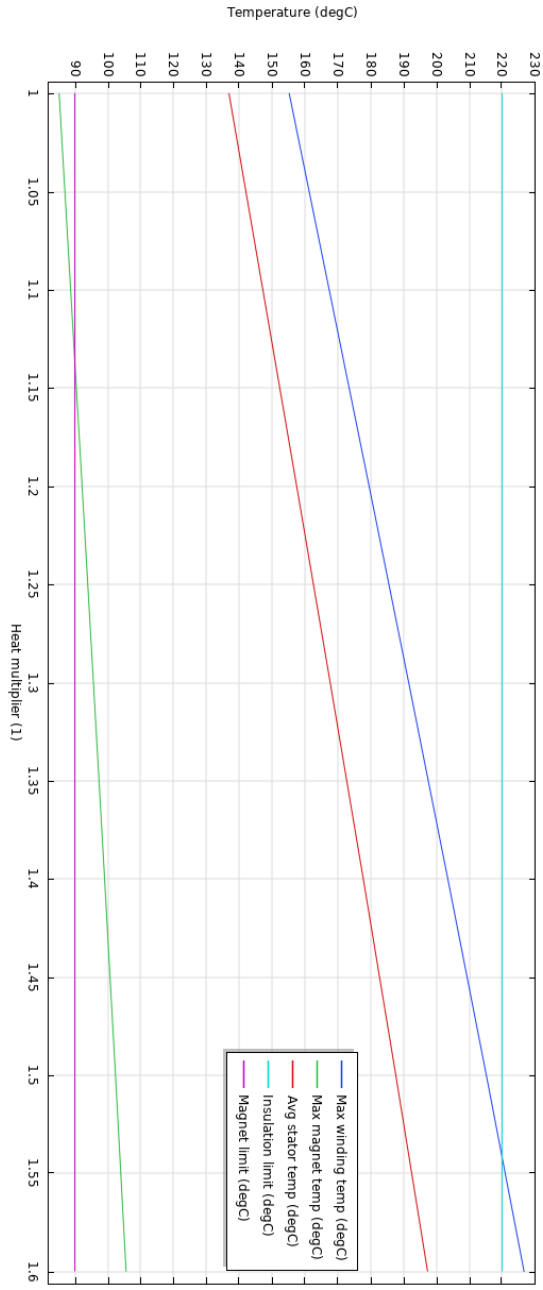

Figure 3.7: $\dot{Q}_{stator}$ temperature sensitivity.

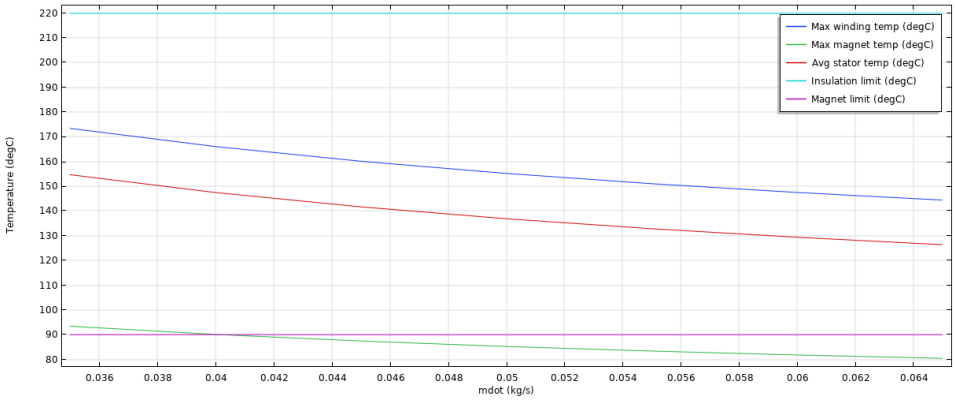

(a) $\dot{m}$ temperature sensitivity.

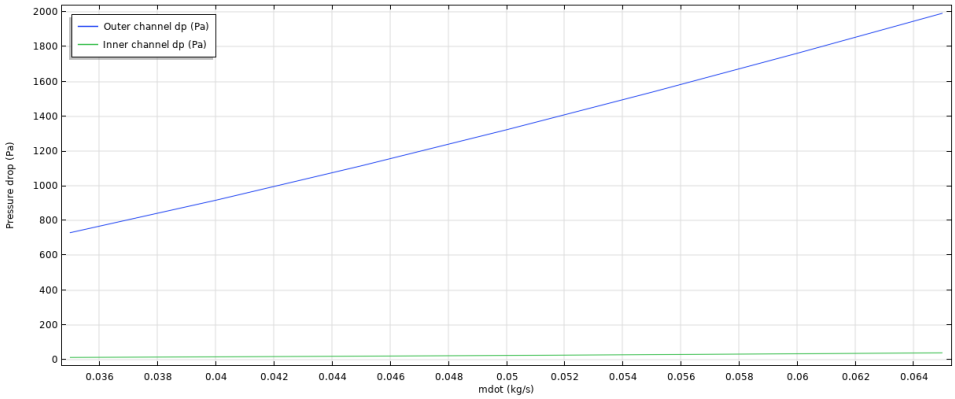

(b) $\dot{m}$ pressure sensitivity.

Figure 3.8: $\dot{m}$ influence.

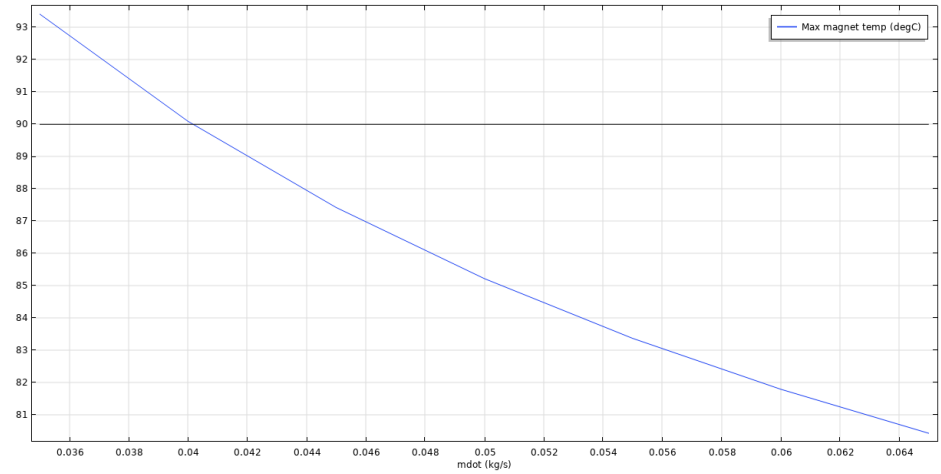

(a) Maximum magnet temperature @ varying $\dot{m}$.

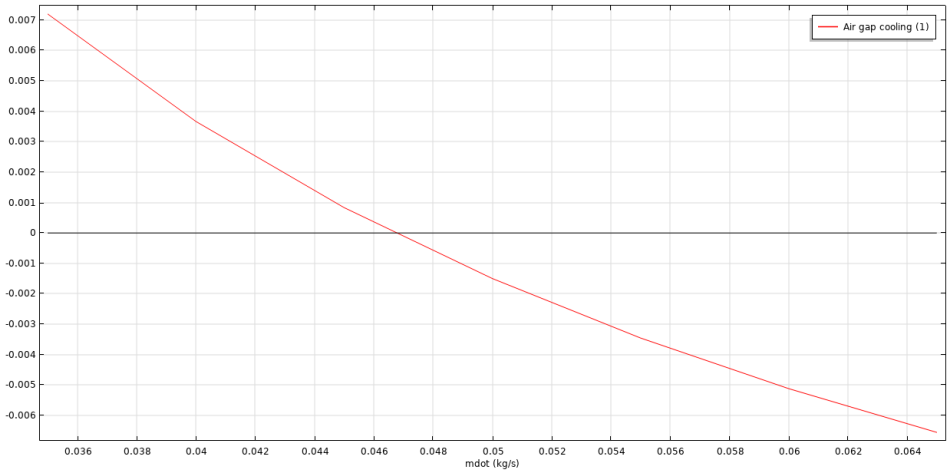

(b) Heat flux stator $\rightarrow$ rotor @ varying $\dot{m}$.

Figure 3.9: Magnet temperature & out-of-stator heat flux.

3.3 Prototype & Calibration Test

The goal of this project was to produce a physical prototype of the electrical machine with the oil cooled TMS. This would be used to set up an experimental test bed for the team to evaluate the numerical results compared to a real-world case. The experiences taken from the construction and running of the motor would eventually assist the analyses for the potential next iterations of the machine.

Due to unforeseen environmental constraints and time limits, this test rig did not reach the construction phase. Despite this shortcoming, the outline of the planned thermal experiment is presented in the following section.

For the thermal analysis, the prototype experimentation would serve two main purposes:

1. Verify & calibrate the numerical model
2. Uncover overlooked thermal phenomena or manufacturability issues

Item 1. is the fundamental intention. Having simulated the TMS and the machine performance in COMSOL, the results will be dependent on the model assumptions and estimates of material parameters in order to make a good representation of the real world case. Comparing the virtual representation to a tangible prototype will show whether these simplifications and choices are valid, and it is possible to update the numerical model parameters to follow more closely to the actual machine.[12]

While 2. refers to unknown concerns, it is still possible to logically predict possible matters. For one, the size of the machine and the flow channels in the TMS renders the construction susceptible to manufacturing errors. This risk is further heightened by cutting costs in the manufacturing process, which will typically infer larger tolerances in the geometry.

A critical step is the packing and impregnation of the electrical windings. The packing factor, PF, is important to keep high, both for the electromagnetic performance and the thermal conductivity of the copper section (further discussed in chapter 7), though this might prove difficult to achieve with the small slot dimensions. The impregnation is done by filling the air gaps between the windings and stator slot with resin. If there are air gaps left in the slot after this operation, these will act as heat transfer barriers, increasing the copper temperature (further discussed in section 7.2). On the other hand, if the resin fills the spaces intentionally left open for the cooling channels, this would block the oil flow and impede the TMS.

3.3.1 Calibration Test

The test itself would consist of two separate steps: the first is running a direct current (DC) through the windings, utilizing Ohm's law (3.12) to have a well defined power loss located

[12] Boglietti et al. 2018.

in the windings.[13]

$$U = \mathbb{R}_{el} I \tag{3.12}$$

with U being the voltage drop over the test section, $\mathbb{R}_{el}$ the electrical resistance through the winding and I the DC current.

This process can be carried out on both sub-assemblies as well as the total machine if necessary. While the DC experiment is underway and has reached steady-state, strategically placed temperature probes monitor the temperature field within the structure. Comparing this to the COMSOL model with equal heat generation will identify the differences between the two. This method can potentially help calibrate hard-to-define parameters such as k_W, k_L and $\mathbb{R}''_{W,int}$, as well as convection coefficients, h, for the coolant flow.

Having calibrated the model, a second, alternating current (AC) test could be run with the same instrumentation setup, this time using the numerical model to evaluate the losses and their distribution within the machine. The second analysis could also be expanded to include transient operation and different loading scenarios, testing the capacities of both the machine and the TMS.

3.3.2 Instrumentation

The method described above was envisioned to be used on the entire stator + TMS assembly with or without the rotor. A satisfactory amount of type T thermocouples were planned to be labelled and positioned within the winding slots as described in figure 3.10, including additional extras located on the stator iron itself. As has been noted in the numerical analysis, it is the stator that experiences the highest temperatures and strongest gradients, and so it is assumed that it should be sufficient to monitor only this part of the motor.

The cooling system and transformer oil would be evaluated by a separate series of T-thermocouples, following the piping and instrumentation diagram seen in figure 3.11. A flow-meter (FI0101) combined with a regulator valve (FC0101) is set up to measure and control the flow of coolant. The pump unit, tank and plate heat exchanger ensure a steady supply. The in-flowing and out-flowing temperatures are monitored by sensors TI0101 and TI0102, respectively.

During the experiment, both systems (01 = coolant, 02 = test rig) should be observed to check for steady state and check for critical errors and/or failure. If the tests were to be carried out, a preliminary simulation of the testing conditions should be run in the COM-model to indicate the expected values and identify possible runaway scenarios.

[13] Boglietti et al. 2018.

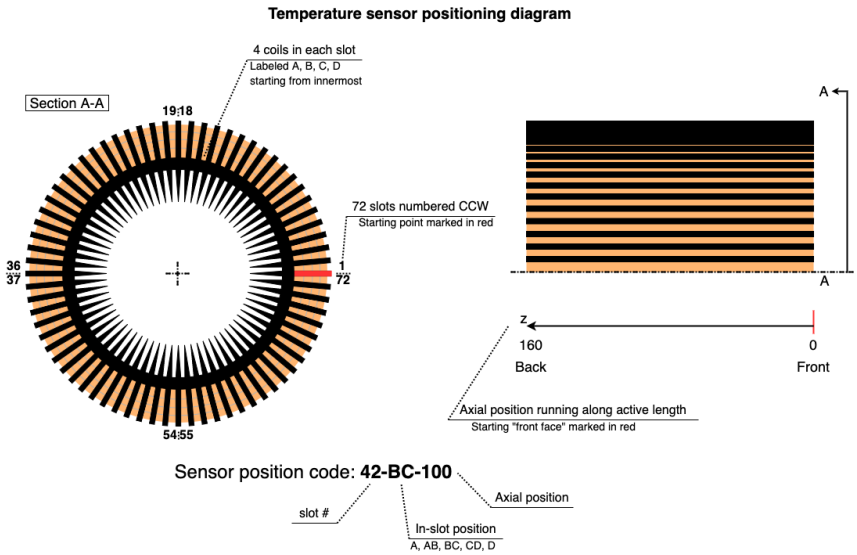

Figure 3.10: Test bed stator visualizing the location codes of the thermocouples.

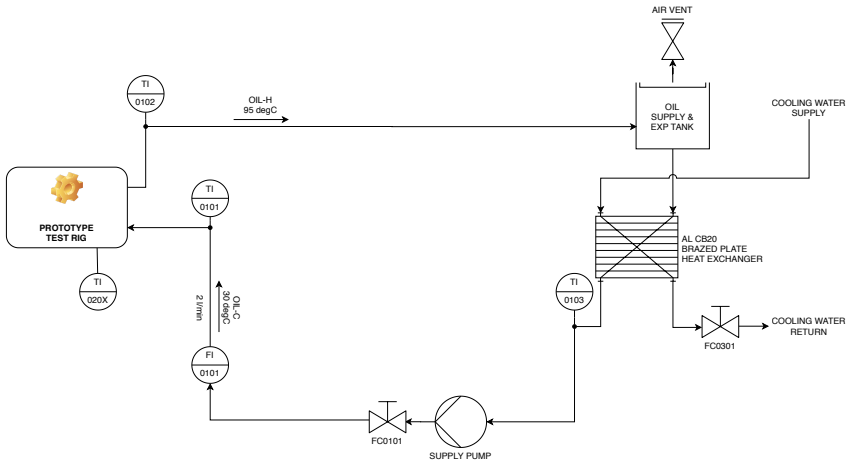

Figure 3.11: Cooling cycle P&I diagram.

Chapter 4

Air Cooling

As described in section 2.3.2, an alternative TMS is designed using air as cooling fluid for the same prototype motor described in chapters 2 & 3. It will consist of an open loop with two parallel channels. The air will be taken in through an inlet with the help of a fan, split and led through the two paths, after which they are expelled from the machine.

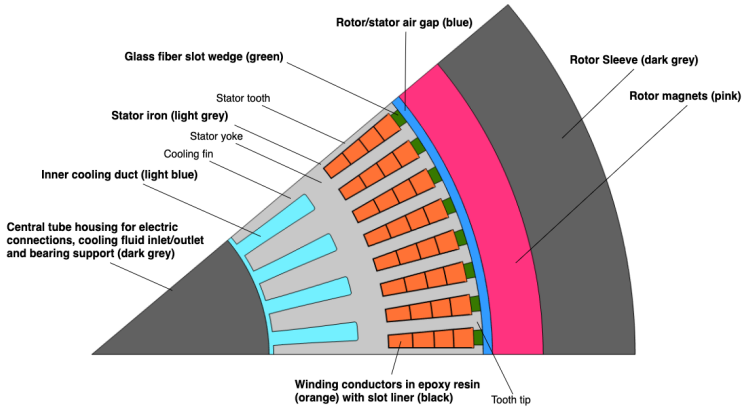

Figure 4.1: $\frac{1}{9}^{th}$ of the simulated, air cooled motor (radial cross-section) (revisited).

The main concern lies in how high the necessary mass flow rate should be in order to maintain the machine at stable operating conditions, how much of this should pass through either channel, and what the resulting pressure loss in each duct would be. The last issue relates to two questions: whether the pressure drop in one would be significantly higher, limiting the amount of air that would pass through this section, or if both are critically high, rendering it infeasible or uneconomical to make the supply fan.

This chapter aims to create a model using a combination of established correlations, FE conduction simulation in COMSOL, and CFD analysis. This will be used to identify the required air mass flow rate, pressure drop and windage loss. The machine performance can then be analyzed and compared with the oil-cooled version when optimizing the motor, which will be done in chapter 5.

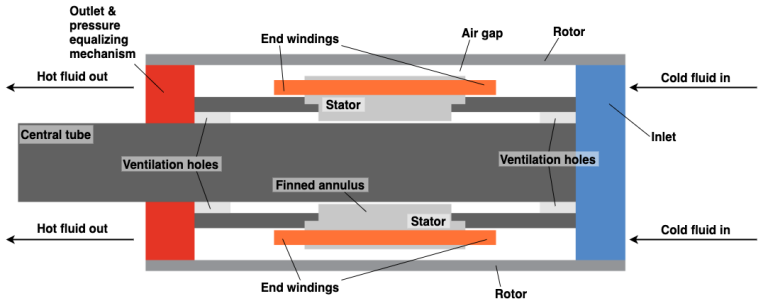

Figure 4.2: Assembly drawing of the air cooled motor + TMS (axial cross-section) (revisited).

The main benefit of using ambient air as coolant is the fact that it is readily available in the surrounding atmosphere. By simply opening up the motor, letting the gas pass through the cooling ducts and be vented back out, the resulting open-loop cooling system omits the need for storage tanks and secondary heat exchangers to keep a stable supply of cold fluid. Depending on the size and mass of these support structures, removing them would potentially be a significant weight benefit, which is a critical factor in aircraft applications.[1]

There are on the other hand several drawbacks to substituting transformer oil for ambient air in the TMS, including:

a. Air having poor heat transfer characteristics compared to oil

b. Turbulent mass flow rates may be necessary, leading to increased pressure losses

c. Optimization of inlets & outlets, as well as a fan and a filtration unit

d. Mass inflow is dependent on the incoming airspeed

e. The atmospheric conditions change with altitude

Addressing a., common convection coefficients for gases may lie in the range between 25-250 W/m^2K, while liquids, including oils, value from 100-20000 W/m^2K.[2] This implies that in order to achieve the same rate of heat transfer, following equations (2.3) and (2.8), either the temperature difference between the stator and the coolant, or the mass flow rate of air has to increase.

[1] Hepperle 2012.
[2] Incropera et al. 2013.

Assuming that the inlet temperature is limited to that of the surrounding atmosphere, the mass flow rate remains as the most viable option for optimizing the heat transfer. As an added bonus, a sufficiently high $\dot{m}$ will trigger turbulence, which will greatly increase the heat transfer coefficient. However, as noted in b., a turbulent flow will inflict higher pressure losses within the channels. The air supply fan will be scaled according to this value, raising the question whether it is feasible or economically reasonable.

Another issue with open-loop configurations are how the the air is sucked in and expelled. Currently, the rotor completely encloses the stator in an outer, rotating shell. This will have to be opened in some way by adding ventilation holes, and a fan unit and nozzle should be installed to impose the necessary pressures to drive the air flow. Additionally, air intakes and exhausts need to be implemented in the final design, which have to be aerodynamically optimized.[3] Abrasive particles or other pollutants must also be filtered out to avoid damaging the machine.[4]

Considering the application for this machine, namely to be placed on an aircraft, the speed at which it travels will impose an incoming air velocity on the cooling channel intake. Conversely, during ground operations, the vehicle is still or travelling at low speeds (or completely still), which will reduce the incoming air mass, causing the system to be less efficient during ground operations.

Item e. refers to how the air properties, temperature, pressure and density vary with altitude. Notably, each of these parameters drop steadily as the height above sea level increases. This can be seen in section A.11, the international standard atmosphere (ISO 2533:1975), as reported by the International Organization for Standardization.[5]. The decreasing density will directly affect the incoming mass flow rate, reducing it at higher elevation, which will in turn drive up the temperatures in the machine. Reduction in inlet pressure will affect the fan performance, while the lower temperature will improve the heat transfer, but will have to be weighted against the adverse effect of the thinner air.

In other words, the air cooled TMS sizing analysis should consider the effects of air heat transfer characteristics (a.), flow characteristics (b.), application specifics (c. & d.) and the atmosphere (e.). However, since this is a free standing concept prototype, neither the effects of d. nor e. are examined in the present study. The aim of the air TMS evaluation is to have grounds for comparison with the oil-cooled concept, presenting alternatives for optimization. For this reason, the inlet air is considered at sea level, standard atmospheric conditions, as seen in table 4.1. The main items to consider are heat transfer (a.) and flow (b.), while practical considerations (a.) are included, but not calculated.

Item c. concerns a joint structural and CFD analysis of the machine and TMS, and is outside the scope of this study.

[3] Dubois et al. 2016.
[4] Yi and Haran 2019.
[5] International Organization for Standardization 1975.

$\boldsymbol{\rho}$	$\boldsymbol{\nu}$	$\boldsymbol{k}$	$\boldsymbol{c_p}$	$\boldsymbol{Pr}$
$1.16\,\frac{kg}{m^3}$	$1.59 \cdot 10^{-5}\,\frac{m^2}{s}$	$2.63 \cdot 10^{-2}\,\frac{W}{mK}$	$1.01\,\frac{kJ}{kgK}$	0.707

Table 4.1: Thermophysical properties of air @ sea level.

The model will be created by establishing separate relations for the air gap and finned annulus heat and momentum transfer characteristics, starting with the air gap. These will then be combined with the FE COMSOL model of the stator geometry and evaluated.

4.1 Air Gap Characteristics

Since this report's primary focus is on the thermal performance of cooling systems, the main issue lies in finding a good model for the convective heat transfer between the heated rotor/stator surfaces and the air flowing through the air gap. Correlations based on experimental studies and numerical analysis exist for cases both with and without axial flow.[6] However, since both the geometry and flow structure have multiple degrees of freedom, choosing the correct relation for the actual case has to be handled with care. Slight differences in geometry, experimental set-up, boundary conditions and assumptions between the correlation and the case may lead to relatively large errors.

In the following sections, some existing flow models from the literature are presented, after which they are compared to a turbulent CFD simulation of the prototype machine air gap. The final goal is to have a suitable correlation to implement in the air-TMS.

4.1.1 Geometry & Non-dimensional Numbers

The air gap model is characterized by its geometry, flow structure and heat transfer boundary conditions. These parameters relate to their respective non-dimensional numbers. These will be presented, and their influence on heat and momentum transfer will be discussed later.

The cavity geometry is described by its hydraulic diameter, D_h, the radius ratio, ϱ, and the aspect ratio, Γ. For simplicity, the indentations on the stator surface from the slots are considered to be filled with a glass fiber slot wedge, leaving two concentric cylinders.

$$\delta = R_{Ri} - R_{So} \tag{4.1}$$

$$D_{h,ag} = 2\delta \tag{4.2}$$

$$\varrho = \frac{R_{So}}{R_{Ri}} \tag{4.3}$$

$$\Gamma = \frac{L_A}{\delta} \tag{4.4}$$

[6] Fénot et al. 2011.

Equations (4.1)-(4.4) applied to the prototype machine yields table 4.2. The air gap in the present case is narrow, with a large aspect ratio.

$\boldsymbol{\delta}$	$\boldsymbol{D_{h,ag}}$	$\boldsymbol{\varrho}$	$\boldsymbol{\Gamma}$
$2[mm]$	$4[mm]$	0.977	80

Table 4.2: Air gap geometric parameters.

The outer cylinder, the rotor, has a fixed rotational speed, ω, which will, due to the no-slip condition and viscosity, cause the air in between the rotor and stator to flow.[7] The resulting flow structure can be described by either the Taylor number, or rotational Reynolds number:

$$Ta = \frac{\omega^2 D_{Ri} \delta^3}{2\nu_{air}^2} \tag{4.5}$$

$$Re_{\theta,ag} = \frac{\omega D_{Ri} \delta}{\nu} \tag{4.6}$$

Additionally, an axial mass flow of air enters at one end and leaves the other, serving as the cooling flow for the TMS. This will superimpose on the existing fluid movement, which is governed by the axial Reynolds number, or optionally, the flow rate coefficient, Φ:

$$Re_{z,ag} = \frac{2\dot{m}_{ag}}{\pi \delta \rho \nu} \tag{4.7}$$

$$\Phi = \frac{\dot{m}_{ag}}{R_{Ri} \rho \nu} \tag{4.8}$$

In some cases in the literature, the combined axial and rotational flow can be characterized by a vector-averaged effective Reynolds number, $\overline{Re}$:[8]

$$\overline{Re} = \sqrt{Re_{z,ag}^2 + \alpha Re_{\theta,ag}^2} \tag{4.9}$$

Where α is some coefficient $\in [0, 1]$, weighting the influence of either part of the flow, dependent on the report. The corresponding $\overline{Re}$ to the actual correlation are given, when applicable.

4.1.2 Flow Conditions

The combination of axial and rotational flow, also known as Taylor-Couette-Poiseuille (TCP) flow, in an annulus exhibits complicated behaviour dependent on both directions of fluid movement, as well as the duct geometry and presence of heating. As a consequence, it is important to critically review previous studies when utilizing or comparing

[7] Çengel and Cimbala 2010; Childs 2010.
[8] Fénot et al. 2011.

the results.[9] Notably, most of the literature presented in this section regards to the case of the inner and not the outer cylinder rotating. It is however assumed that the physical phenomena remain the same. As such, it is of little importance which side is stationary and which is not.

Generally, the flow is characterized by the presence and magnitude of the two superimposed flows. The axial contribution is considered to become turbulent at sufficiently high $Re_{z,ag}$, while the rotation will at some critical Taylor number, Ta_c cause toroidal vortices to form, known as Taylor vortices. These phenomena merge when the flows coexist, causing four possible combinations:[10]

i. Laminar flow

ii. Laminar flow with Taylor vortices

iii. Turbulent flow

iv. Turbulent flow with Taylor vortices

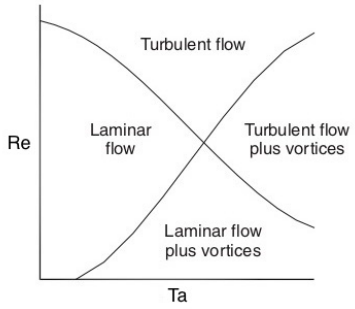

Source: Childs 2010.

Figure 4.3: Interaction between the four flow modes in a rotating annulus with axial flow.

The transition between either of the four modes is dependent on $Re_{z,ag}$ and Ta, as is shown in figure 4.3.[11] However, as noted by Becker and Kaye, these limits are dependent on both the air gap geometry and the temperature gradients in the fluid.[12] This is further complicated by the fact that the boundaries found in figure 4.3 are not as sharp as might seem from the representation, but rather behave as gradients from one to another.[13]

The main mechanisms behind the heat transfer in the annulus are directly dependent on the flow mode. Therefore, it is necessary to give a brief description of each in the following.

[9] Fénot et al. 2011.
[10] Becker and Kaye 1962; Fénot et al. 2011; Howey, Childs, and Holmes 2012.
[11] Childs 2010.
[12] Becker and Kaye 1962; Fénot et al. 2011.
[13] Çengel and Cimbala 2010; Fénot et al. 2011.

i., laminar flow, relates to the classical case of Couette flow between parallel plates which may or may not be superimposed with a laminar, axial flow. This mode is dominated by the viscous forces and can be solved analytically.[14] The fluid will be heated through convection close to the wall, where there is little flow, and the heated particles will be carried parallel to the rotor/stator surfaces along the streamlines (which is commonly referred to as advection). This is the conventional example of convection heat transfer.[15]

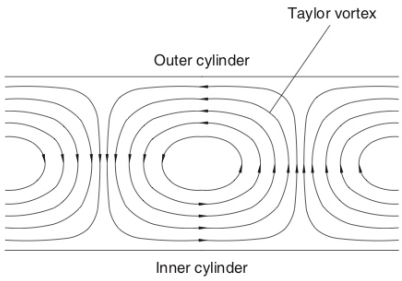

Source: Childs 2010.
Figure 4.4: Taylor vortex (axial CS).

As the Taylor number increases, passing Ta_c, the radial pressure gradient and viscous forces are no longer able to counteract instabilities in the flow. Consequently, toroidal vortices form along the annulus, known as Taylor vortices (ii.). These are found in symmetric pairs rotating against each other, as shown in figure 4.4.[16]

These toroids will stack perpendicular to the flow direction, and the "mixing" movement created by the onset of these structures enhance the heat transfer, as it adds a normal advection component to the flow.

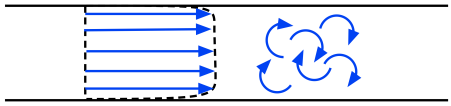

Source: Ryan Toomey. University of South Florida / CC BY-SA, Creative Commons.
Figure 4.5: Turbulent flow (axial CS).

Turbulent flow (iii.) through ducts are characterized by the chaotic fluid motion that occurs due to the relatively high inertial forces in relation to the viscous forces, as expressed by the Reynolds number (2.10).[17] The disorderly flow will typically fluctuate in all three

[14] Çengel and Cimbala 2010; Howey, Childs, and Holmes 2012.
[15] Incropera et al. 2013.
[16] Childs 2010.
[17] Çengel and Cimbala 2010.

dimensions, and will in the case of heat transfer achieve the same effect as the Taylor vortices, enhancing advection.

Naturally, since both turbulence and vortices intensifies the convective heat transfer, the combination of both (iv.) will have the greatest effect. However, the addition of the axial flow at high Reynolds numbers will effectively postpone the onset of Taylor vortices, making this mode more demanding to achieve.[18] This can be observed in figure 4.3. An empirical relation for this effect is given:[19]

$$Ta_c(Re_{z,ag}) = \sqrt{Ta_{c0}^2 + 6.625Re_{z,ag}^2} \tag{4.10}$$

Where Ta_{c0} is the critical Taylor number without axial flow, which is found to be 1700.[20]

The heat transfer associated with the Taylor-Couette-Poiseuille flow will, as noted, differ according to the flow structure present in the annulus. A study performed by Becker and Kaye reported the behaviour shown in figure 4.6.[21] The x-axis displays the Taylor number, and the separate lines correspond to different Reynolds numbers, where the top part contains the turbulent regime while the bottom is laminar. Note that the definition of Nu and Ta differ somewhat between the plot and the current report, and that figure 4.6 is first and foremost emblematic.

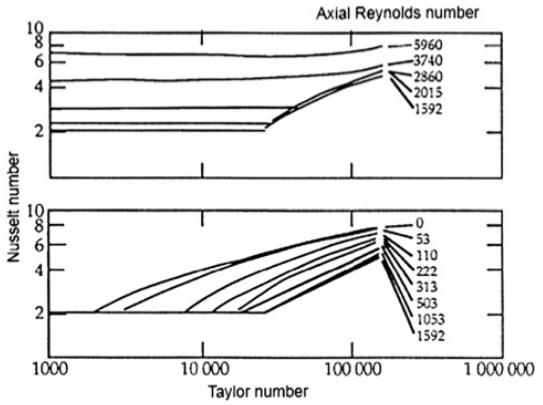

Source: Becker and Kaye 1962.
Figure 4.6: Nusselt number evolution with varying Ta and $Re_{z,ag}$.

Figure 4.6 exhibits the four separate modes: The straight lines on the bottom graph indicates the constant values typically associated with laminar flow,[22] while the abrupt inclina-

[18] Becker and Kaye 1962.
[19] Childs 2010.
[20] Fénot et al. 2011.
[21] Becker and Kaye 1962.
[22] Incropera et al. 2013.

tion models the increase in heat transfer following the onset of Taylor vortices. As $Re_{z,ag}$ increases, the critical Taylor number will rise, extending the linear regime in accordance with the "delay effect" noted previously.

At a sufficiently high Reynolds number, the influence of the turbulent structures increase Nu, as the top part of figure 4.6 demonstrates. The horizontal lines lie at increasing values of Nu, while the critical Taylor number is continuously inflated. It seems from the graph that the influence of the Taylor vortices become less as the turbulence increases, which would carry some logic, though the range of Ta in the experiment is not wide enough to fully support this argument.

Due to the complexity of the model and the dependencies on flow structure, temperature and geometry, the best option to describe the heat and momentum transfer characteristics of this type of flow is by empirical correlations or numerical studies. Though, as mentioned, since there are multiple degrees of freedom, it is important to review the conditions of previous results before indiscriminately using the expressions and/or values in one's own work. For this reason, a combined study of certain established correlations and a CFD analysis is performed. This is described in more detail in the following sections.

In the following calculations, the air thermophysical properties are taken at the mean bulk fluid temperature:

$$T_{mid} = \frac{T_{out} + T_{in}}{2} \tag{4.11}$$

4.1.3 Air Gap Windage Loss

The windage loss in the air gap results from the viscous forces from the acceleration of the fluid from rest at the stator to the tangential velocity at the rotor. This power dissipation directly affects the machine performance, as it opposes the rotational movement, causing losses. It is commonly defined as follows:[23]

$$\dot{W}_{wnd} = C_w \rho \pi \omega^3 R_{Ri}^4 L_A \tag{4.12}$$

The windage coefficient, C_w, is a non-dimensional number dependent on the flow structure, geometry and magnitude. Since the windage loss is important for electric machine design, C_w is typically found through experiments or numerical simulations and directly inserted into equation (4.12) in the motor performance analysis. In this study, three of these correlations are listed in table 4.3 (with the full relations are listed in appendix A.7). These are not analyzed in full detail, as they are not the main focus of this report, but will be used in comparison with a numerical, turbulent CFD model for inspection.

The two first models in table 4.3 relate to pure rotational flow, also known as Taylor-Couette (TC) flow, and serve two purposes: One is to have a benchmark for comparison with rotational-axial models, the other is for the calculation of windage losses for the

[23] Gorland, Kempke, and Lumannick 1970.

machine without the air-TMS. The experimental values found by Gorland, Kempke, and Lumannick are the ones used with equation (4.12) to calculate the windage loss found in table 2.2. The third expression covers the combined case of both axial and rotational flow, and will be used as comparison with the CFD model for the full TCP analysis.

Model	Relation (ap. A.7)	Description
Gorland, Kempke, and Lumannick	$C_w(Re_{\theta,ag}, \delta)$ - A.7.1	Experimental study tabulated data with different air gap sizes @ varying rotational speed.
Zheng et al.	$C_w(Ta)$ - (A.1)	Experimental correlation for TC flow.
Gao and Yu	$C_w(Re_{\theta,ag}, Re_{z,ag})$ - (A.2)	Experimental correlation for TCP flow, accounting for the added axial flow.

Table 4.3: Windage coefficient correlation comparison.

It is assumed that if the numerical solver is able to capture the behaviour of the turbulent, viscous flow, it should also be sufficient to model the non-isothermal behaviour of the flow.

4.1.4 Air Gap Convection

In the oil-TMS model, the air gap was modelled as a solid with an apparent thermal conductivity taken from Tachibana and Fukui's correlation for Taylor-Couette convective heat transfer between two cylinders, as described in section 3.2. This is a commonly used relation, having been backed by multiple other studies.[24]

$$Nu_{ag} = 0.42(Ta \cdot Pr)^{\frac{1}{4}} \qquad \text{(3.7 revisited)}$$

As previously discussed, the heat transfer is dependent on the flow structure modes. Equation (3.7) assumes a fully developed Taylor vortices and no bulk axial movement, which is an appropriate assumption it the case of a fully enclosed air gap space. Though suitable for the simple case, it does not model the added effect of the throughflow. Comparing different heat transfer studies in the literature, the expressions and correlations for the heat transfer characteristics vary between the cases.[25] This may be due to the multiple degrees of freedom described in 4.1.2, or simply differences in experimental setup and measurements.

This leaves the question which is most applicable for the current model, which may be further complicated by the fact that the prototype case parameters may be different from the previous studies' assumptions. Several possibly suitable correlations have been chosen

[24] Fénot et al. 2011; Tachibana and Fukui 1964.
[25] Fénot et al. 2011.

from a review by Fénot et al. and are listed in table 4.4.[26] These will presently be compared to a CFD model of the prototype's geometry and heat transfer boundary conditions in order to either verify one or more of the relations, or create a new expression fitting the present configuration. The full expressions in table 4.4 are shown in appendix A.8 along with the ranges of ϱ, Γ, $Re_{z,ag}$, $Re_{\theta,ag}$ and Ta.

Model	Relation (ap. A.8)	Description
Kosterin and Finatev	$Nu(\overline{Re})$ - (A.4)	Based on experimental data of TCP flow.
Grosgeorge	$Nu(\overline{Re}, Re_{z,ag}, Pr)$ - (A.6)	Based on experimental data of TCP flow.
Bouafia et al.	$Nu(\overline{Re})$ - (A.8)-(A.10)	Based on experimental data of TCP flow.
Poncet, Haddadi, and Viazzo	$Nu(Re_{\theta,ag}, Pr, \Phi)$ - (A.12)-(A.13)	Based on numerical study of TCP flow.

Table 4.4: Nusselt number correlation comparison.

4.2 CFD of the Air Gap

In order to analyze the windage friction relations (table 4.3) and Nusselt number correlations (table 4.4), a CFD numerical model has been created in COMSOL to numerically simulate the physical phenomena. The results from this experiment will be compared to the expressions found in the literature.

4.2.1 Model Description

The model geometry is a 2D-axisymmetric representation of the air gap, measuring $2 \times 160mm$ (ref. tables 2.1 & 2.5). The geometry is considered symmetric on the θ-axis to save computational time, and it is assumed that the velocity and temperature gradients in this direction are negligible.

COMSOL uses a combined multiphysics study solving both the heat and momentum transfer. This implies the construction of two separate sets of boundary conditions and solver configurations. The basis is a "swirl flow"-model, allowing for rotational velocity while

[26] Fénot et al. 2011.

simplifying the problem to 2D.[27] The flow equation is considered turbulent, following the random-averaged-Navier-Stokes, k-ω turbulence representation with wall functions at the viscous sublayer. The heat transfer occurs between the stator, air and rotor, where the two surfaces are kept at constant temperatures and the air enters at ambient temperature. The main characteristics of the CFD model are listed in table 4.5.

	Model	**Boundary conditions**
Turbulent flow	RANS	Outer rotor rotational speed [rpm]
	k-ω	Inner stator fixed wall
	Wall functions	Inlet air mass flow rate [kg/s]
Heat transfer	Fluid heat transfer	Rotor constant wall temperature (100°C)
		Stator constant wall temperature (200°C)
		Fluid inlet temperature (20°C)

Table 4.5: COMSOL CFD model of the air gap.

4.2.2 Results

The model described above was first run for only the turbulent flow model, adjusting the mesh refinement and comparing with the windage relations found in table 4.3 in order to verify the model setup itself. When it could be seen that the solver had converged, a parametric sweep was performed, varying first the rotor rotational speed at zero axial flow, and then adding an increasing inlet mass flow rate of air while keeping the rotational speed constant at 15 000rpm. The limits are denoted in table 4.6.

Simulation #	**Description**	$\boldsymbol{Re_{z,ag}}$	$\boldsymbol{Ta}$
	Fixed $\dot{m}$	0	
1	Variable ω		$[1.2 \times 10^6, 7.6 \times 10^6]$
	[6,15] krpm		
	Variable $\dot{m}$	$[0, 8.2 \times 10^3]$	
2	[0,0.06] kg/s		
	Fixed ω		7.6×10^6

Table 4.6: Turbulent flow simulation sweeps.

As figures 4.7a and 4.7b show, the windage coefficients, C_w, in the numerical model (light blue line) follows the same behaviour as the previous correlations and experimental studies, yet the CFD seems to underestimate. A 35% error between the experimental data from Gorland, Kempke, and Lumannick (blue line) can be registered at 15 000 rpm, 0 kg/s. Similarly, at increasing axial flow, both the Gao and Yu-correlation (green line) and the simulations keep to the same trend, though their numerical values are unequal. A 12% error is found at 15 000 rpm, 0.06 kg/s. Otherwise, the models found in the literature

[27] COMSOL 2019.

coincide with each other within 10%.

Disregarding the numerical error, all models show a decrease in C_w at increasing ω. Though it may seem counter intuitive that the friction coefficient drops at higher flow speeds, equation (4.12) gives the relation $\dot{W}_{wnd} \propto C_w \omega^3$, indicating that the total windage loss will still increase, though the influence of rotational speed diminishes. The axial flow, on the other hand, does not by itself impose any direct opposition to the rotor, and is not accounted for in equation (4.12), yet it will still enhance the windage friction factor, causing more loss. This may be explained by a possible interaction between the turbulent and the Taylor vortices, but closer inspection is needed.

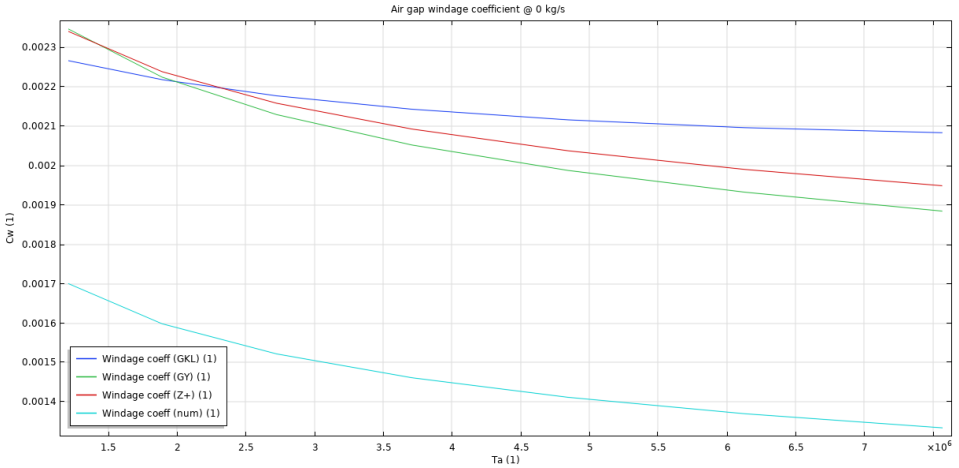

(a) C_w @ fixed mass flow rate (0 kg/s).

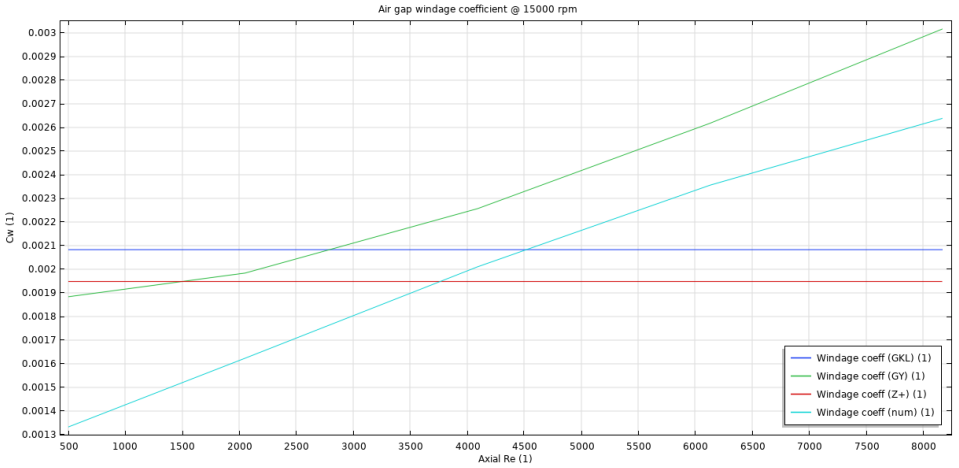

(b) C_w @ fixed rotational speed (15 000 rpm).

Figure 4.7: Windage coefficient comparison.

Following the momentum transfer analysis, a similar parametric sweep was done for the combined flow and heat transfer study, outlined by table 4.7. Note that the upper limit of mass flow rate is slightly lower than for the turbulent flow simulations, which was due to model instability at higher $\dot{m}$. The Taylor number for iteration #4 will vary $\sim 15\%$ due to the air kinematic viscosity, ν, being dependent on the fluid temperature.

Simulation #	**Description**	$\boldsymbol{Re_{z,ag}}$	$\boldsymbol{Ta}$
3	Fixed $\dot{m}$ Variable ω [5,15] krpm	0	$[4.7 \times 10^5, 3.7 \times 10^6]$
4	Variable $\dot{m}$ [0,0.05] kg/s Fixed ω	$[0, 9.0 \times 10^3]$	$(5.0 \pm 0.7) \times 10^6$

Table 4.7: Turbulent flow & heat transfer simulation sweeps.

The Nusselt numbers in the CFD simulations were evaluated at both the stator and rotor side of the air gap. As results from both Poncet, Haddadi, and Viazzo and Bouafia et al. indicate, the rotor side has slightly higher heat transfer characteristics.[28] Since this study is mainly concerned with the convection at the stator surface, Nu_S is presented in figure 4.8, while the Nu_R-plots are found in appendix A.9

Figure 4.8 shows a good concurrence between previous studies and the present CFD-model. The results seem to correspond closest to the relation given by Bouafia et al., though similar as to the windage coefficient, the simulated values estimate lower Nu_S than the correlation. Poncet, Haddadi, and Viazzo's expression grossly overestimates the heat transfer and is ruled out from the study.

The CFD study shows some peculiar behaviour when increasing the mass flow, as it has a minimum Nu-value at $Re_{z,ag} \approx 6000$. As a consequence, the Nusselt number will gradually increase for lower mass flow rate, which is not in accordance with the findings of Becker and Kaye (ref. figure 4.6), where the lower axial Reynolds numbers would converge on a constant Nu-value. Neither of the correlations from the literature follow the same trait as the numerical results.

It is believed that both the low values of C_w and the unnatural trend of the Nusselt-evaluation are symptoms of a wrongly calibrated CFD-model. Since the 2D-simplification and assumption of rotational symmetry oppose any possibility of angular gradients, the 3D nature of both the turbulent flow and the Taylor vortex structures are severely limited. The high Taylor numbers and axial Reynolds numbers indicate that this flow configuration would be in mode iv., and the interaction between turbulence and the rotation may not be accurately captured by the simple geometry. Though it was initially suspected that the flow would exhibit some form of symmetry, the strong assumptions made for the 2D swirl

[28] Bouafia et al. 1998; Poncet, Haddadi, and Viazzo 2011.

flow to be valid have to be revised. This work is however beyond the scope of this thesis and is left for further analysis.

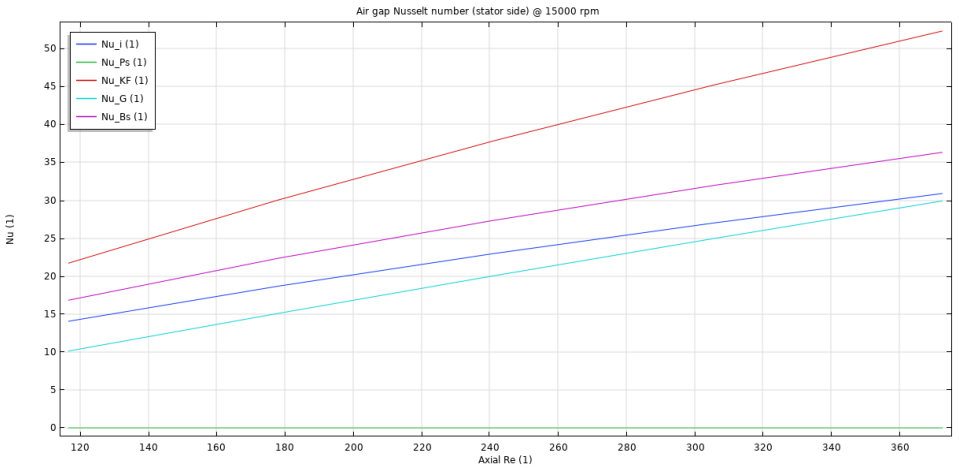

(a) Nu_S @ fixed mass flow rate (0 kg/s).

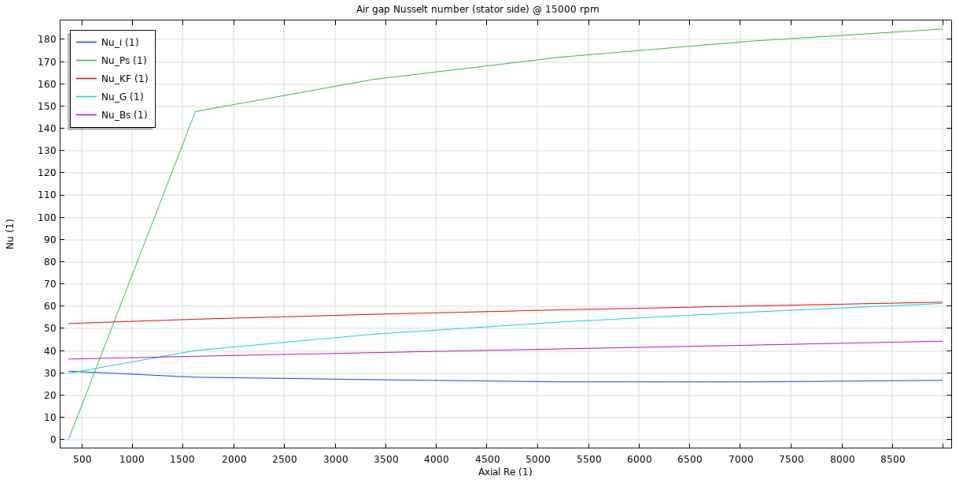

(b) Nu_S @ fixed rotational speed (15 000 rpm).

Figure 4.8: Nusselt number (stator side) coefficient comparison.

Despite the limitations of the CFD study, the model is still able to provide good initial estimates of the flow and heat transfer behaviour. For one, the study supports the theory of separate Nusselt numbers for the still and rotating sides, following closely to Bouafia et al.'s correlation. Secondly, since neither rotor nor stator is isolated, the existence of an axial mass flow, as well as its magnitude, is the deciding factor for both the extent of heat transfer as well as its direction.

Considering figure 4.9, showing the radial temperature evolution at the mid-axial position of the air gap from the stator (left) to the rotor (right). Dependent on the axial mass flow rate, the heat transfer coefficient will change, but so will also its heat uptake and subsequent temperature increase, following equation (2.8). Since heat transfers from higher to lower temperature (as per the second law of thermodynamics),[29] the interaction between the bulk air temperature, T_b, the stator wall temperature, T_S, and the rotor wall temperature, T_R, is the deciding factor as to which direction the heat flux will travel.

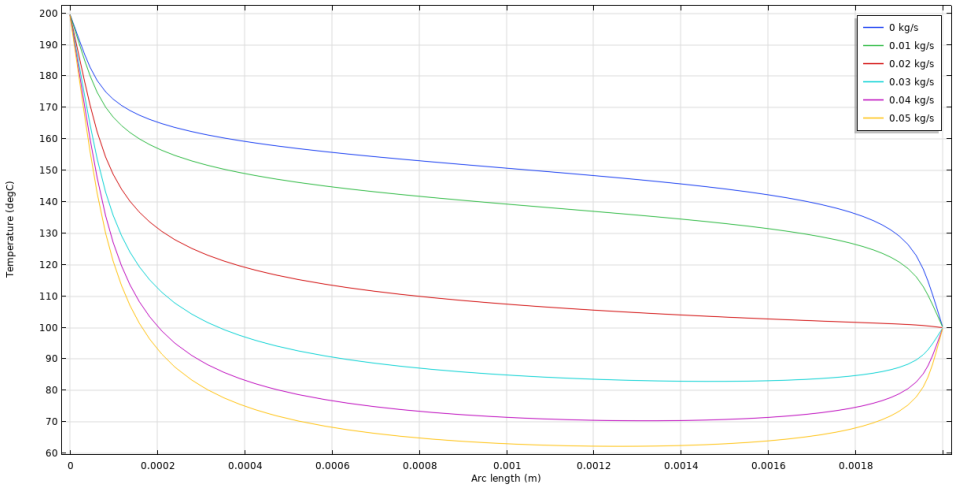

Figure 4.9: Radial temperature evolution @ $L_A/2$.

Recalling the findings in section 3.2.2, the magnet temperature was the main limiting factor in the oil-TMS design. As shown in figure 4.9, an air mass flow rate of 0.02kg/s will have almost zero temperature gradient towards the rotor wall, implying that no heat transfer happens between the air flow and the rotor. The findings from the sensitivity analysis of the oil cooling (section 3.2.3) also showed that zero heat flux from the stator towards the rotor is needed in order for the magnets to be sufficiently cooled, where the outer cooling channels were set to act as "heat shields" to enforce this condition.

Granted, this feature further complicates the heat transfer boundary conditions for the experiment, since these changes in boundary condition will affect the Nusselt number.[30] It

[29] Moran and Shapiro 2006.
[30] Fénot et al. 2011.

can be seen in figure A.7b, that the average rotor side Nu_R will fluctuate, which is believed to be due to the mentioned effect. This may also help explain why the Nu-function is concave down.

Though sufficiently precise as to model the phenomena and display the same characteristics as models from the literature, the accuracy of the COMSOL CFD study results are questionable, and are thus not used in the further air-TMS analysis. Instead, the windage coefficient from Gao and Yu (eq. (A.2)) and Nu_S-correlation by Bouafia et al. (eq. (A.10)) is used in the correlation-based study.[31] The axial pressure drop relation (eq. (4.13)) from COMSOL is kept due to shortage of other alternatives. The improvement of the numerical representation is left for further work.

The axial pressure loss (figure A.6) as a function of mass flow rate through the air gap follows the linear relation:

$$\Delta P_{ag} = 30 \left[\frac{kPa \cdot s}{kg} \right] \cdot \dot{m}_{ag} \tag{4.13}$$

4.3 Correlations for the Finned Annulus

Due to the poor heat transfer characteristics of air, a turbulent flow is needed to achieve suitable performance of the finned annulus cooling duct.[32] Uniaxial turbulent flow through conduits of constant cross section has more well defined heat and momentum transfer characteristics in the literature, and the relations are directly implemented as-is into the finned annulus part of the model.

The friction coefficient, as expressed by Petukhov, Irvine, and Hartnett, gives the pressure drop of the air passing the fins:[33]

$$\frac{C_f}{2} = \frac{1}{\left(2.236 \ln(Re_{if}) - 4.639\right)^2} \tag{4.14}$$

$$\Delta P_{if} = C_f \frac{L_A}{D_{h,if}} \frac{1}{648\rho} \left(\frac{\dot{m}_{if}}{A_{\text{fin gap CS}}} \right)^2 \tag{4.15}$$

The turbulent flow heat transfer is given by Petukhov and Kirillov:[34]

$$Nu_{if} = \frac{\frac{C_f}{2} Re_{if} Pr}{1.07 + 12.7\sqrt{\frac{C_f}{2}} \left(Pr^{\frac{2}{3}} - 1 \right)} \tag{4.16}$$

$$h_{if} = \frac{L_A}{D_{h,if}} Nu_{if} \tag{4.17}$$

[31] Bouafia et al. 1998; Gao and Yu 2013.
[32] Gjeset 2019.
[33] Kays and Crawford 1993; Petukhov, Irvine, and Hartnett 1970.
[34] Petukhov and Kirillov 1958; Petukhov, Irvine, and Hartnett 1970.

4.4 Correlation-based Study of the Air Cooling System

Having established the proper relations for the machine-air heat transfer characteristics, a complete model of the air-TMS configuration can be set up and evaluated. This analysis follows in many ways the same method as the ITM and OCM models described in section 3.1, as it uses the COMSOL FE solver for the heat diffusion equation and convection heat transfer correlations as outer surface boundary conditions. This is shown in figure 4.10

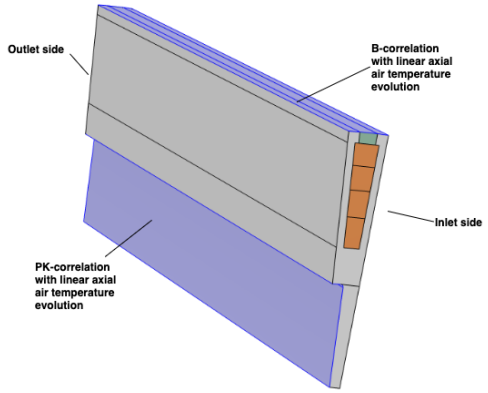

Figure 4.10: Air TMS COMSOL model geometry with flow boundary conditions.

There are, however, three main differences. For one, the cooling channel arrangement is slightly modified to better serve the air-TMS, with a more detailed description of the differences given in section 2.3.2. Secondly, the air travels in parallel through the air gap and the inner, finned annulus simultaneously, this implies that the total, incoming mass flow rate is split in two parts, resulting in a mass split factor, m^*, as defined in equation (4.18). Last, since air has lower heat transfer characteristics than oil, a higher amount is needed, causing the channel flow to be turbulent (as noted in the previous sections).

The flow through the machine is assumed to enter at one end and split into two paths, one through the air gap and the other via the finned annulus, cooling either side of the stator. The mass split ratio, m^*, is defined as:

$$m^* = \frac{\dot{m}_{ag}}{\dot{m}} \tag{4.18}$$

Revisiting equation (2.8), the air temperature in each cavity will also increase as the heat is transferred. The fluid is considered to have constant thermophysical properties, rendering

the following linear relation:

$$\frac{d\dot{Q}}{dz} = \dot{m}c_p \frac{dT_b}{dz} \tag{2.8 revisited}$$

$$\Delta T_b = \frac{\dot{Q}}{\dot{m}c_p} \tag{4.19}$$

Combining equations (4.19) and (2.3), the axial evolution of the convective heat transfer to the coolant can be implemented in the COMSOL FE stator heat transfer model. Since the axial air temperature increase relates directly to the amount of heat transfer to the fluid, an iterative loop similar to the one used in the OCM analysis is implemented. This is detailed in figure 4.11

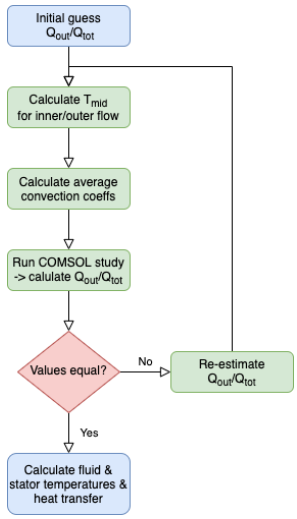

Figure 4.11: Air-TMS MATLAB-COMSOL solver sequence.

Finally, the model is evaluated through two parameter sweeps, one being the total mass flow rate at the inlet, the other over the mass split rate, m^*, at each $\dot{m}$. The two loops as well as the iterative solver in figure 4.11 is handled by a MATLAB-COMSOL LiveLink[35] script.

4.4.1 Results

The ACM model shows that it is possible for a total mass flow rate of 0.05kg/s splitting 50/50 between the finned channel and the air gap is capable of keeping the machine within acceptable operating conditions. The proposed configuration's performance is shown in table 4.8.

[35] LiveLink is a trademark of COMSOL AB

Parameter	Value
Air temperature	
Inlet	20°C
Outlet	
Finned annulus	83.2°C
Air gap	125.5°C
Mass flow rate	0.05kg/s
Mass split	50% out
ΔP	
Finned annulus	65Pa
Air gap	750Pa
Maximum winding temperature	200°C
Average stator temperature	170°C
Fin effectiveness, ϵ_{fs}	3.6
Fin efficiency, η_{fs}	0.90

Table 4.8: Air cooling system thermal performance.

This conclusion follows the evaluation of the air TMS as a function of the mass split factor, m^*, which can be seen in figure 4.12 was within the range 10% to 90%. The plot shows that allowing approximately equal amounts of the total mass of air (0.05kg/s) flow through either channel, the maximum stator temperature will reach 200°C. The same evaluation also shows the pressure loss in each channel (fig. 4.13) and the amount of the total heat generated within the stator transferred to the outside or inside heat sinks (fig. 4.14).

When comparing figures 4.12 and 4.14, it can be noted that the best TMS performance is when the heat taken up by the air gap cooling is higher than what is cooled by the fins. At some point, the mass flow passing the fins becomes too small to have much effect, and the stator temperature will rise. However, the stator reaches higher temperatures with dominant fin cooling than with dominant air gap cooling, indicating that the air gap is a more effective heat sink. At the optimum m^*, the heat transferred to the air gap is a little above 60%. The reason behind the effectiveness of the outer cooling is due to its relatively closer proximity to the more critical heat generator, namely the windings. This will be discussed in greater detail in section 5.1.2.

The pressure losses, shown in figure 4.13, indicate as expected that more energy is required to drive the air flow through the air gap than via the finned annulus, though the maximum ΔP is still quite low, not even reaching 2 kPa. The difference in pressure loss through each channel will have to be solved through some sort of nozzle system, as discussed in section 2.3.2. Effectively, the inner annulus pressure drop has to equal that of the air gap, or else the mass flow split ratio will adjust so that the equal pressure is met. In figure 4.13, this equates to $m^* \approx 0.12$, overheating the stator to a maximum temperature of $\sim$240°C. However, the actual design and optimization of the nozzle, or pressure equalizing system is left for further work.

It must also be noted that the validity of these results must be checked, as they derive from an incomplete CFD model (discussed in section 4.2.2).

From a thermophysical point of view, at this point of the analysis, not accounting for the support structures (ducting, secondary heat exchangers, filters etc.), both the oil cooled and the air cooled TMS are equally capable of maintaining stable operating conditions within the electrical machine. In the following chapter, the two systems are evaluated against each other, taking into account some of the more practical sides of the case omitted from the thermal analysis up to this point.

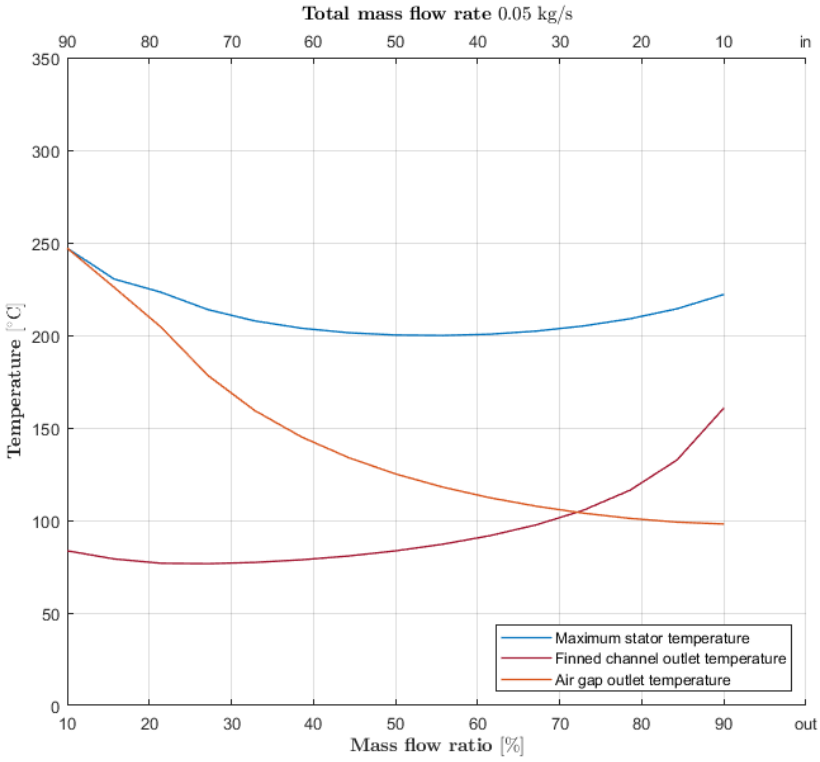

Figure 4.12: Maximum stator & air temperature @ varying m^*, $\dot{m} = 0.05kg/s$.

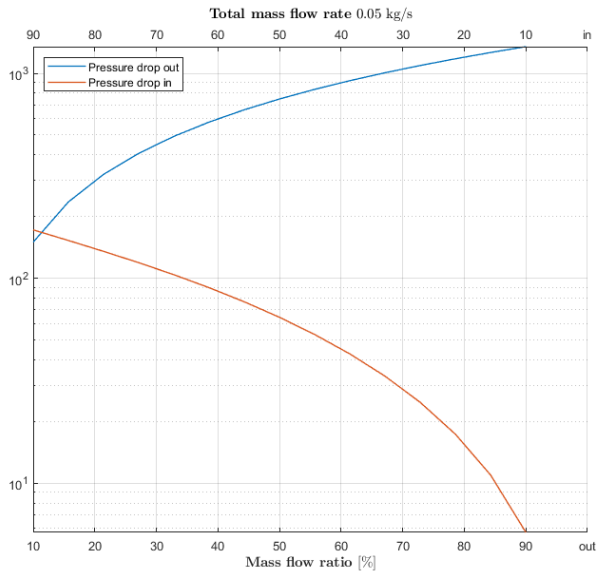

Figure 4.13: Pressure drop through air gap & finned annulus @ varying m^*, $\dot{m} = 0.05kg/s$.

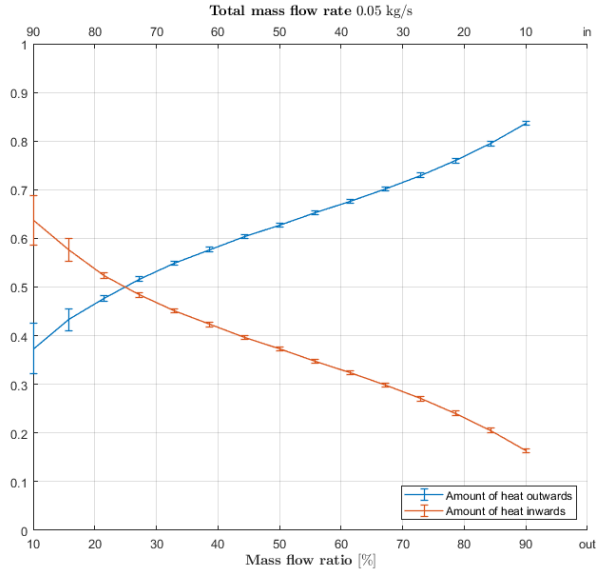

Figure 4.14: Heat uptake through air gap & finned annulus @ varying m^*, $\dot{m} = 0.05kg/s$.

Chapter 5

Cooling Concepts Comparison & Discussion

The study has tested two thermal management system (TMS) concepts on the same prototype outrunner motor, proving that either design is capable of ensuring good operating conditions. Neither versions operate with high pressure losses, yet they still deliver the necessary mass flow rates in order to sufficiently cool down the machine. There is even the added potential of letting in more without an excessive hike in pressure drop, proving a robust channel design.

Looking only at the thermal analysis covered in chapters 3 and 4, the two alternatives consist of similar geometry and achieve the same general result. However, they are based on two different flow concepts enforcing several additional considerations for each system. These are first and foremost practical issues regarding integration of the total system with the electrical machine and/or the potential aircraft application, which prove difficult to compare in numbers. The influence of these factors will not be analyzed in great length, but the ideas are presented in order to help assess the two designs.

Since the study so far has been on the active length of the stator, omitting the pumps, fans, ducts, etc., the main comparison analysis will be based on this isolated domain. Later, in section 5.1.3, the more complete system is discussed.

5.1 Comparison

The main distinction between the two systems are: (1) coolant; either oil or air, (2) flow direction; series or parallel coupling of the two cooling channels, and (3) the shape of the outer heat sink; isolated, axial ducts or using the entire air gap. All of these aspects relate to the original choice to compare a closed and an open-loop configuration.

5.1.1 General Performance

Figure 5.1 presents a side by side comparison of the two designs at their optimal mass flow rates.

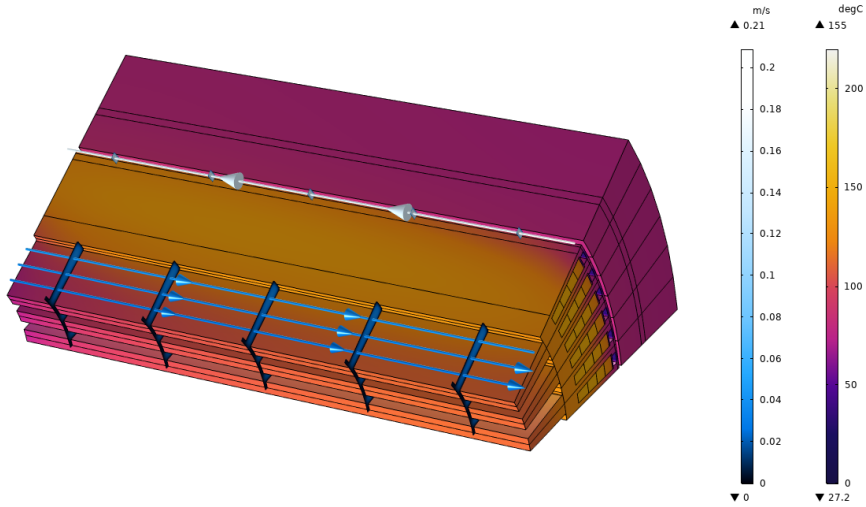

(a) COM-model with oil TMS.

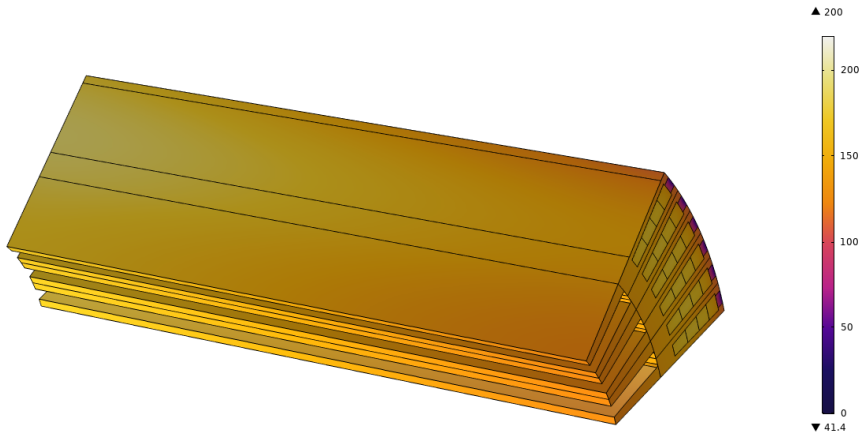

(b) ACM-model with air TMS.

Figure 5.1: Side by side comparison of the machine temperature fields with either oil or air TMS.

In the figures, both sections are oriented so that the fluid enters at the right side (the front of the machine), but for the oil TMS (fig. 5.1a), the same mass flow that enters the outer channels will be collected on the left side and return via the finned annulus, as both the

cooling ducts are coupled in series. This is indicated by the arrows on the streamlines. Meanwhile, the air alternative (fig. 5.1b) splits the total mass flow in two separate streams passing through either the air gap or the finned annulus in parallel, exiting at the left side.

A more obvious difference between the two figures is that the ACM does not include the rotor, and that the mass flow optimization is done with regards to the winding insulation maximum temperature (220°C). For this reason, the stator in figure 5.1b is considerably hotter than the one in figure 5.1a (note that the temperature color scale is equal). Though the rotor is missing from the air model, it is assumed that the magnets will not be as significant to the air TMS as it was found to be for the oil TMS, as the air gap cooling will contribute to the cooling of the rotor. This will be discussed in more detail later.

Otherwise, the temperature gradients within the two machines are relatively small. The parallel configuration will leave the outlet end hotter than the inlet, due to the heating of the air flow reaching its maximum at this section. The series arrangement of the oil cooling will counter this effect by having the inlet and outlet at the same face (right in fig. 5.1a), which in turn causes local cooler areas at the entry of each cooling duct, augmented by the thermal development of the flow.

In the separate analyses, the pressure loss through the channels were calculated. Based on this, the total theoretical fan/pump power can be estimated by formula (5.1), and the respective values are presented in table 5.1.

$$\dot{W}_{supply} = \frac{\dot{m}}{\rho}\Delta P \tag{5.1}$$

	Oil TMS	**Air TMS**
ΔP [Pa]	1300	750
$\dot{W}_{supply}$ [W]	0.07	30

Table 5.1: Theoretical fan work required for flow through cooling ducts.

It is important to note that equation (5.1) calculates the theoretical minimum work required, and that in reality, the fan/pump efficiency has to be considered, however, this calculation is done to give an example of the relative ratios. As can be seen from table 5.1, though the pressure losses are of relatively equal magnitude, the power supply for the flow is more than 400% higher in the air TMS. This is mainly due to the difference in density between the two flows.

The oil flow pressure loss through the ancillary circuit is not accounted for in ΔP, neither are the inlet and outlet sections of the air flow. This will modify the values in table 5.1 somewhat, though the fan work is still assumed to be higher than the pump. All in all, any of these configurations would require considerably less than any of the losses noted in table 2.2, and as such, the difference is negligible. Despite this, the relative difference

should be considered when scaling up the design.

It can be noted from figure 5.2 that the outer heat sink, closest to the electrical windings, is distinct between the two TMS designs: Since no oil is supposed to leak out of the closed-loop, the whole stator has to be encased by a glass fiber sleeve, this is what sets up the 72 outer channels system between the tooth tips. Conversely, the air flow does not require this outer casing, allowing the stator to be exposed and the entire air gap between the rotor and stator acts as the cooling channel.

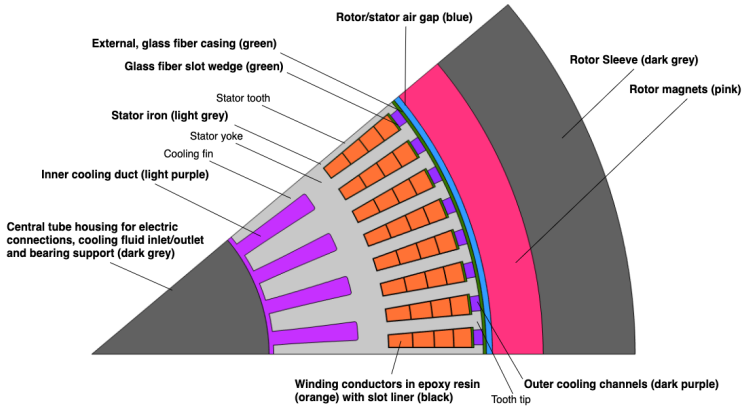

(a) $\frac{1}{9}^{th}$ of the simulated, oil cooled motor + TMS (radial cross-section) (revisited).

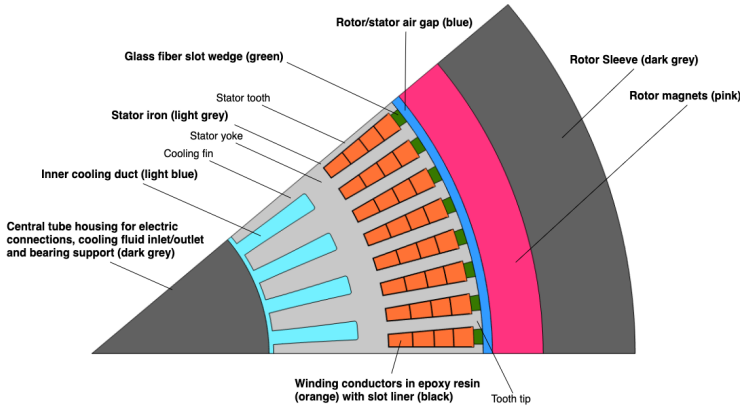

(b) $\frac{1}{9}^{th}$ of the simulated, air cooled motor (radial cross-section) (revisited).

Figure 5.2: Side by side comparison of the TMS model radial cross-sections.

In the COM analysis, the air gap was modelled as a solid domain with a modified air conductivity based on Tachibana and Fukui's correlation, since no there is no axial air flow

in the oil TMS.[1] It was shown that no heat could be transferred from the stator outside surface through the air gap to the rotor, lest the magnets should exceed their temperature tolerance. In effect, the outer cooling duct needs to serve two purposes: It should cool down the stator windings as well as shield the rotor from any outwards heat flux (section 3.2.3, fig. 3.9). As was seen later in the air gap numerical analysis, this would potentially be a built in function in the nature of the flow (section 4.2.2, fig. 4.9).

The ability to adjust the mass flow split, m^*, and thereby the cooling through either channel will help in this regard. Adding more air to the outer channel will increase the local cooling at the outer side of the stator, and may also to some degree help cool the rotor as long as the bulk flow temperature is sufficiently low, adding to the "shield effect". This is effectively why the air TMS is able to keep an overall higher temperature within the stator than the oil TMS, since the latter is limited by the fact that it has to adjust the total mass flow through both ducts in order to relieve the rotor.

5.1.2 Cooling Channel Evaluation

Both TMS alternatives work on the same principle of direct cooling, inasmuch as they both impose integrated, convective cooling flows close to the source of the heat generation. The TMS could either impose a strong temperature flux on the outside boundary of the assembly so that the machine's maximum temperature is below the allowed limit, or it could instill a more evenly spread, or critically located, heat extraction inside the components themselves. The latter option is direct cooling, which will, if properly designed, ensure a more uniform temperature distribution than indirect cooling.[2]

In the double conduit configuration used in both TMS designs, the goal is to remove the heat at their source. It can be shown that both the air and oil versions in this project have their highest performance when more heat is being transferred to the outer side than the inner, despite the fact that the surface area of the outer heat sink is less than half of the finned annulus. The outer cooling is responsible for absorbing most of the winding losses, which in this case is the most volumetric dense heat generation. This is illustrated in table 5.2, indicating how much of the total heat generated within the stator is taken up by the outer duct(s), as well as their relative heat transfer surface to the fins'.

	Oil TMS	**Air TMS**
Heat out	54%	63%
$A_{oc/ag}/A_{fs}$	0.47	0.33

Table 5.2: Heat and area ratios for the outside/inside heat transfer.

Meanwhile, the previous study indicated that both channels are needed to overcome the

[1] Tachibana and Fukui 1964.
[2] Yang et al. 2016.

heat generation, as the heat transfer surface at the outer cooling is too small.[3] The combined system shows promise by being capable of both directly cooling critical components, as well as adding enough surface area to make a compact and efficient heat exchanger.

This was made possible due to the integrated electromagnetic, structural and thermal design process. It is believed that a more aggressive, cooperative approach is what is necessary to construct the high specific power, high speed machines needed for electric flight.[4] This collaboration is especially important in the practical implementation of all the components created for this machine, making sure all the parts work as planned and combine well.

5.1.3 Practical Considerations

The TMS in itself is not without its drawbacks, however, as the more integrated design of both versions leaves the heat exchanger more vulnerable to manufacturing issues and overlooked implementation issues. If the system fails or is not working properly, it is not as simple as removing and improving a water jacket. Additionally, when constructing the machine, it is important to consider all of the support structure, making sure that these components also are included in the optimization and design process.

In order to complete the design process, collaboration is needed to ensure a manufacturable prototype with good performance. In the intersection between the separate fields lie choices such as: material selection, integration of components and support structures, manufacturing considerations and combined sensitivity analyses. Many of the practical issues discussed in this section happen in the intersection between one or more of the respective fields. During this project, cooperation was limited since each team member had to focus on the individual tasks and theses. The outbreak of COVID-19 and the subsequent closing of the campus further complicated the matter. The natural next step in the continuation of this project would be to combine the results from the reports and locate potential design conflicts and possible combinations for improvement.

The analysis of the TMS design relies heavily on the assumptions made for the material temperature limits. Though these choices have been made from ”best practice” choices and characteristic values, the actual material selection for the real machine are yet to be made. Areas of particular interest are the winding insulation and magnets, of course, but also the slot wedge and outer shell material in the oil TMS. In the analysis, this is suggested to be a glass fiber composite, but little more is known about its thermal behaviour other than an experimental thermal conductivity.[5]

The nature of the oil TMS, being a closed-loop configuration, is both one of its main strengths and weaknesses. The flow, driven by an external pump, can be controlled much

[3] Gjeset 2019.
[4] Hepperle 2012; Yi 2016.
[5] Saripally 2015.

more easily than for an air cooled machine, implying that it is more convenient to adjust mass flow according to the losses. However, as the name suggests, the oil circuit has to remain sealed, and potential leaks may severely impede the system performance. It is vital that the mechanical construction of the oil TMS is capable of containing the coolant as well as ensuring the planned flow cycle.

On top of this is the added weight from the closed-loop system support structure, which includes coolant tanks and secondary heat exchangers (SHE). The SHE's purpose is to cool down the heated oil returning from the machine until it reaches back to its inlet flow temperature and sent back. The sizing of this structure is dependent on the same parameters as the heat exchanger within the motor, namely cooling method, flow rate and geometry.

Lastly, since the oil TMS contains more components than the air TMS, it may be more susceptible to failure. If there are blockages, pump breakdowns, leaks and/or other malfunctions, the cooling performance may be critically limited. On the other hand, the open-loop air cycle is heavily dependent on air speed and favourable atmospheric conditions in order to work properly. Safety is an important factor in the design of aircraft components, and an assessment should be carried out on the robustness of either design.

The design of the air inlet and outlet, as well as the supply fan and nozzle have not yet been discussed. The open-loop configuration in the air TMS will require a redesign of the closed-drum rotor planned for the current prototype.[6] This work will have to be carried out in close collaboration with structural engineers, in order to ensure mechanical integrity at high speed operation. If this machine should be used as an aircraft motor, additional study should be done on the aerodynamic qualities of eventual inlets and outlets.[7] The same considerations have to be made for the SHE in the oil TMS in the case that a liquid-air heat exchanger is selected.

In the end, most practical experience comes from exactly experience with physical machines. It was for this reason planned to construct the prototype ER motor described in this thesis, based on the works of the multidisciplinary team.[8] This was, sadly not achieved within the time frame of this project, and remains for further studies. The considerations made in this section are laid out as arguments to evaluate when furthering the design of the electrical machine and the TMS.

5.1.4 Numerical Model Accuracy

Having little real-world experimental data on the actual prototype to compare with, it is difficult to specify quantitatively the error from the numerical model. Some of the potentially overlooked aspects are covered in the section above, though most of these are difficult to capture by this type of study. Instead, it is possible to quantitatively assess the

[6] Verde 2019.
[7] Christie, Dubois, and Derlaga 2017.
[8] Fossum 2019; Gjeset 2019; Verde 2019.

assumptions made during the thermal analysis.

The following are the most important assumptions for the COM model:

i. Steady state operation with constant, uniform heat generation within the stator iron and winding material

ii. Only the active length of the stator is part of the study; end-windings, bearings, manifolds & collector pipes are omitted

iii. Air gap can be modelled as a solid with an effective thermal conductivity and a constant volumetric heat generation

iv. Windings are lumped together as one piece with an intermediate copper/insulation conductivity

v. Characteristic values for conductivity and thermal contact resistance

vi. Outside rotor convection as a rotating cylinder in ambient, atmospheric air

vii. Secondary heat exchanger and other support structure is omitted

viii. Negligible radiation heat exchange

Though further investigation into these simplifications would potentially render a more detailed analysis and more accurate results, it is believed that the more pressing matter for the realization of the prototype machine will be to address the items listed in section 5.1.3. Besides, ii., v., vi., have already been partially evaluated through the sensitivity analysis (section 3.2.3), and iv. will be analyzed in the subsequent chapters. For its intents and purposes, the COM model is deemed sufficiently accurate, though a experimental calibration, as suggested in section 3.3.2 would eventually help verify both the TMS and its numerical representation.

The following are the most important assumptions for the ACM model:

i. Steady state operation with constant, uniform heat generation within the stator iron and winding material

ii. Only the active length of the stator is part of the study; end-windings, bearings, manifolds & collector pipes are omitted

iii. Negligible contributions from the windage and rotor losses

iv. Fully developed, turbulent flow in finned annulus

v. Air gap heat transfer follows unverified correlation

vi. Linear, axial temperature evolution of the cooling air

vii. Air gap pressure loss follows unverified relation

viii. Windings are lumped together as one piece with an intermediate copper/insulation conductivity

ix. Characteristic values for conductivity and thermal contact resistance

x. Air entering with sea level characteristics

xi. Ducting, fans and other support structure is omitted

xii. Negligible radiation heat exchange

This list is almost identical to that of the COM, and the same justifications will apply. However, this study relies heavily on the air gap numerical CFD model, which was not shown to capture the Taylor vortices expected at the high Taylor numbers for the case study. This might either imply a numerical or model error, or that simply the turbulence is too high and the vortices are disturbed. The assumptions made for this study are discussed in section 4.2.2, and the conclusion is that the model as-is, is unable to predict accurate behaviour, yet precise enough to help choose a fitting correlation from the literature. This decision was made in order for there to be a first estimate on the air TMS performance. In order to verify and correct this model, further investigation is needed.

5.2 Optimization

This machine was neither designed or built with a focus on weight or performance optimization, but rather as a first iteration of a proposed new design which must undergo further changes before it can be implemented as an actual aircraft motor. However, since weight and high power density is the ultimate goal for this type of machine, some considerations have to be made into how the outrunner motor can improve in terms of weight.

Generally speaking, a higher power density will imply:

A. More power

B. Lower weight

Considering A., this can be achieved by either further electromagnetic optimization of the machine or increasing the current density in the windings. Both of these options will alter the losses, and a re-calibration of the TMS should be carried out. The latter alternative will increase the stator heat generation. As discussed in section 3.2.3, exemplified by figure 3.7, the current oil-TMS is not able to cope with more than a 110% augmentation of the losses, given that the magnets have to be kept below 90°C. Possible solutions include: Upping the oil mass flow rate, using other magnet materials or redesigning the TMS. The simplest alternative would be increasing the oil flow, since this could be implemented without an excessive increase of pressure loss.

The air-TMS ACM model does not include the rotor, though it is implied that the magnet limit should be easier to maintain as the air gap flow would potentially be able to cool

the inner surface of the rotor. At the same time, imposing the axial air flow will increase windage, both cutting performance and raising temperatures. However, it has been shown that, compared to the stator losses, windage is not the principal contributor to the total performance, and the ACM study has predicted only a small ($\sim$22%) increase in windage loss from the added axial mass flow. The viscous heating effect has not yet been studied.

Increasing the packing factor and optimizing the slot shape is from both electromagnetic and thermal perspectives a good way to improve performance. For one, more space for copper gives potential for higher currents and more power. At the same time, since copper is a good conductor, the larger metal volume will increase conductivity and ease the winding heat transfer. This effect will be studied in greater detail in chapter 7. Yet, as was seen in section 3.2.3, the conductive benefit does not greatly affect the hot spots in the motor, and the increased current would lead to higher copper losses, which may in turn overheat the windings.

The TMS may be improved by altering the fin shape. Literature suggests that optimally shaping the fin cross-section will lead to a more even temperature distribution and thus increased heat transfer performance.[9] If possible, a closer evaluation of surface extension shapes may also remove some of the total fin mass, effectively making the stator lighter. If necessary, the same assessment could be done for the channels, but since the geometry is small it is assumed that this would add little benefit. In fact, the fin efficiency, η_{fs} in the oil-TMS is quite high ($> 70\%$).

In a similar fashion, it might also be an option to use higher conductivity resin in the stator slots or graphite sheets between stator laminate stacks in order to augment the thermal conductivity of the machine.[10] These steps, though they might not have as great an effect as increasing the mass flow, is a simple, passive method to improve existing systems if done correctly.

The total weight of both oil and air thermal management systems have yet to be calculated, as there are specific components of each concept that have not yet been considered. For air, this counts the necessary ducting and the fans needed to supply and extract the air flow in the open-loop configuration. The oil, on the other hand, needs both pumps, ducting in and out of the motor, coolant tanks and secondary heat exchangers. However, by comparing the listed support systems for each, the latter has more and heavier parts. It is by this logic implied that the oil-cooled version would potentially be heavier, though this is yet to be verified. TMS design analyses for machines of comparable characteristics have opted for open-loop air cooling.[11]

All in all, it seems that for the prototype machine, the oil TMS is the more robust, well understood system, while the air TMS shows promise with regards to weight. For building the prototype planned for experimental testing, the oil loop is the more suitable, as it is

[9] Alam and Ghoshdastidar 2002; Fabbri 1997; Fabbri 1998a; Fabbri 1998b; Fabbri 2000; Incropera et al. 2013; Kays and London 1984.

[10] Guechi et al. 2013.

[11] Christie, Dubois, and Derlaga 2017; Yi 2016.

easier to monitor (ref. fig. 3.11, section 3.3.2). Since the TMS geometries are similar, the results from the measurements lend themselves to either version. Meanwhile, it is suggested that more detailed analysis of the air gap model could be carried out, as well as a mass analysis, in order to have better grounds for comparison.

Chapter 6

Homogenization Techniques

In the steady-state FE model that the TMS study relies upon, the governing equation is the heat diffusion equation, as defined in section 2.2.1.

$$-k\nabla^2 T = \dot{q} \qquad \text{(2.2 revisited)}$$

Considering $\dot{q}$ a constant given by the electromagnetic analysis, the temperature distribution within the geometry is dependent on the thermal conductivity, k. This implies:

1. A high value of the thermal conductivity, k, will lower the temperature gradients within the geometry
2. A good, precise measurement, or (if necessary) model, for k is needed for accurate solutions

Meanwhile, there are regions within the stator that constitute of a mixture of components; composites. These domains consist of two or more phases with distinct properties, making up a larger structure. The detail modelling of each individual piece within the composite may prove time consuming. The geometry is often significantly smaller than the total structure, and there may be a large amount of separate constituents with a mixture of random and structured organisation. Instead, it is common to homogenize the conglomerate into a single material with a bulk property.[1] This may apply to multiple material structural, electric and thermophysical properties, though in this report it is the thermal conductivity that is of interest.

[1] Callister 2007.

6.1 Composite Domains in the Electrical Machine

In most electrical machines, there are at least two composite domains. In this report, the PM ER prototype is used as an example, shown in figures 6.1 and 6.2. The main components of the stator in the current machine is the iron core and the electrical windings, which are both composite constructions. These will be briefly described.

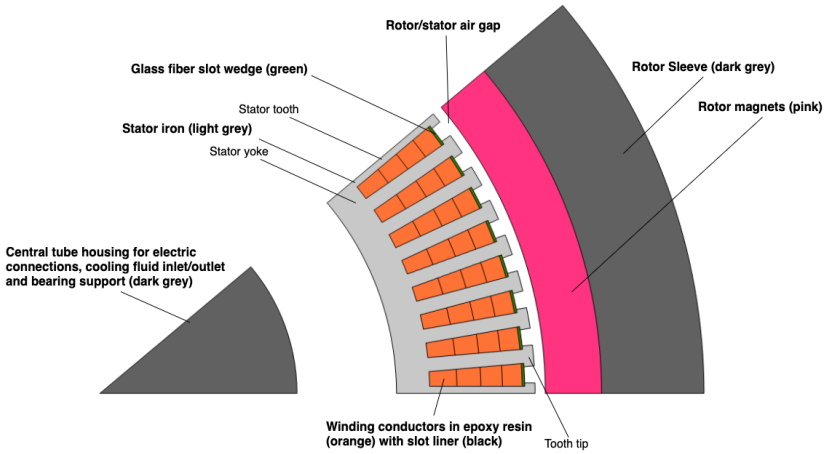

Figure 6.1: $\frac{1}{9}^{th}$ of the base design (radial cross-section) (revisited).

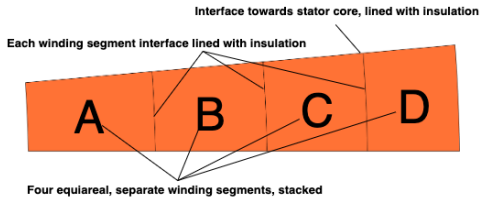

Figure 6.2: Detail of the electrical winding (revisited).

6.1.1 Stator Core

The stator core is a steel structure designed to hold the electrical windings and generate electromagnetic fields powering the motor.[2] In the prototype, this is a simple ring shape with multiple teeth posed radially outwards, separating the different slots.

Though commonly referred to as stator steel, or stator iron, the core actually consists of multiple, thin layers of silicon-steel with some insulation material between. Each piece

[2] Hanselman 2006.

is a radial cross section, and they are stacked atop one another until the active length of the machine is reached. The segmentation is done to prevent core losses,[3] and the general idea is that thinner layers will imply lower loss. The steel sheets may be less than 0.5mm thick,[4] causing the final product to include potentially hundreds of individual segments.

6.1.2 Electrical Windings

In the stator slots there are four separate winding "blocks", as shown in figure 6.2. The windings in an electric machine are the current carrying coils which magnetize the poles, inducing the necessary electromagnetic fields to drive the motor.[5] Though ideally, the only component necessary for this is a metal conductor, these are in reality a composition of single strands of (typically) copper conductors covered by a thin layer of insulation material, bundled together with additional layers of insulation and finally covered in epoxy after being fitted into the slot.

The conducting elements are kept small as to diminish copper loss,[6] and the insulation separates the individual strands. The resulting geometry is a mixture of dispersed wire strands with one or more different plastics (common insulators) in between. Simply due to the large number of constituents, there is some inherent randomness in the composite, though this depends on how the bundle is made. The exact composition and specific materials vary between manufacturers and application needs.

Regardless of the multiple components and structure of an electrical winding, it is common to assume that the cross-section of the bundle remains constant along its length. This is not the case with litz wire.

6.1.3 Litz Wire

Litz is a specific winding type consisting of several individually insulated metal strands which are woven or braided together to form a larger diameter thread. The weaving technique is applied in order to reduce the AC losses in the conductor by weakening the skin and proximity effect.[7] Due to the increased efficiency at higher current frequencies, litz is often implemented to electromagnetic induction, turbines and generators and radio transmission, as well as automotive applications.[8] Some examples are shown in figure 6.3.[9]

The different twisting, braiding and/or shaping technique varies between the different types of litz wire, and the choice of which to apply to a certain motor is typically design-

[3] Fossum 2019; Hanselman 2006.
[4] Fossum 2019.
[5] Hanselman 2006.
[6] Hanselman 2006; New England Wire Technologies 2017.
[7] New England Wire Technologies 2017; Surakitbovorn 2016.
[8] Agile Magnetics 2017; Dull 2019; New England Wire Technologies 2017.
[9] Sullivan and Zhang 2014.

specific. In any case, the more complex geometry of the litz wire have implications for the thermal homogenization model, as will be seen later.

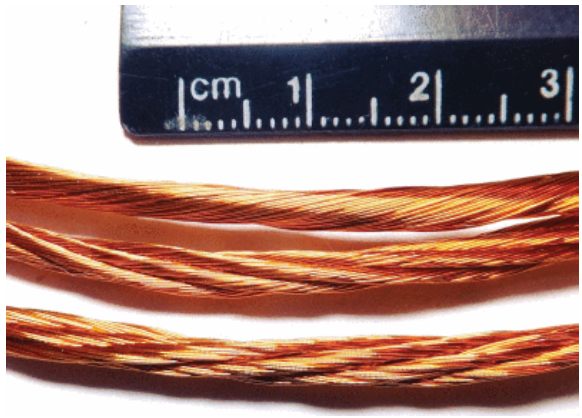

Source: Sullivan and Zhang 2014.
Figure 6.3: Litz wire examples.

6.2 Thermal Modelling of Composites

When creating an FE model of the electrical machine, the composite materials will impose an unnecessary amount of extra detail due to the multiple phases and small geometry. This will drastically increase the computation time. Therefore, it is common to use simplified representations in the thermal analysis of the machine, which are created by homogenizing the total domain into one material. These models have to accurately predict the behaviour of the composite, and are often generalized in such a way so that it captures the geometric and material parameters in order to be able to vary these.

In addition to being non-uniform, both the windings and laminate stack have a clear orientation. As is shown in figure 6.4, when travelling either transverse or longitudinal through the composite, two entirely different paths are encountered. This is assuming the materials have constant cross-sections along these axes.

Letting a particle pass through the stator core (figure 6.4a) along the τ-axis, it will only experience a single material, either silicon-steel or insulation, depending on the λ location. However, traversing the λ-dimension, the particle will pass through alternating layers of the two constituents.

Much the same case applies to the winding (figure 6.4b), however, the the axes are opposite. If a particle travels uni-axially along λ, it will pass through only one phase, while in the transverse plane it is possible to encounter all the different materials. Noted, the transverse cross section of the winding block in figure 6.4b is a random sequence of wire

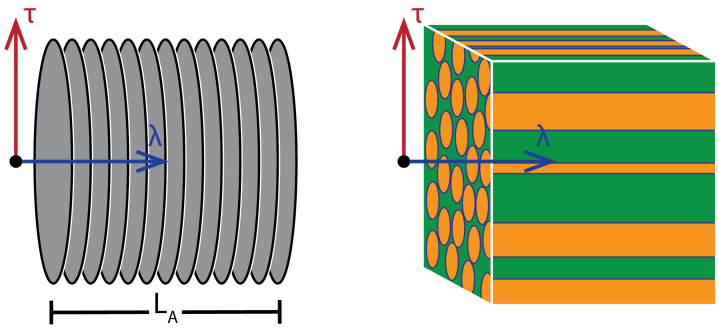

(a) Stator laminate stack. **(b)** Straight wire winding segment.

Figure 6.4: Electrical machine composites with transverse (τ) and longitudinal (λ) material properties.

strands, insulation and epoxy encapsulant, though this is not necessarily always the case. This is discussed further in section 7.2.2.

Due to the directionality of the two composites, it is expected that their material properties will be anisotropic.[10] For this reason it is expected that the thermal conductivity will have two distinct values for k_τ and k_λ. As such these axes are treated separately, and the homogeneous material model in the FE analysis will contain a diagonal thermal conductivity tensor reflecting this 2D property.

The problem remains to find a good way to calculate or measure these directional qualities in order to have a good representation of the material in the thermal analysis. An analytical approach can be taken by using the electrical-thermal analogy of resistance networks.[11] By using this method, one is able to create a system of nodes connected in series or parallel, using Kirchhoff's laws to connect the separate materials, as demonstrated in figure 6.5.

The thermal resistance through a homogeneous, plane wall is defined as:

$$\mathbb{R} = \frac{L}{kA} \tag{6.1}$$

And in the simple case of 1D, constant cross-section conduction, the network can be put together as:

$$\mathbb{R}_{total} = \sum \mathbb{R} \qquad \text{series configuration} \tag{6.2}$$

$$\mathbb{R}_{total} = \left[\sum \frac{1}{\mathbb{R}}\right]^{-1} \qquad \text{parallel configuration} \tag{6.3}$$

[10] Callister 2007.
[11] Incropera et al. 2013.

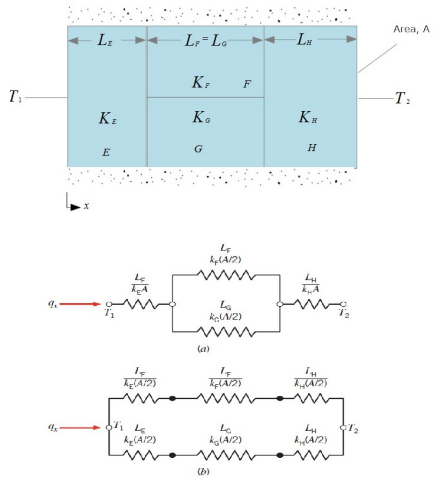

Source: DelPaine. Own work, CC BY-SA 4.0, Creative Commons.
Figure 6.5: Thermal resistance network example for a simple, composite wall.

Equations (6.2) and (6.3) can be directly applied to the laminate stack, as the geometry is simple enough to evaluate analytically. There also exists experimental studies of k_τ and k_λ for the stator core,[12] rendering this composite relatively simple to evaluate. Characteristic, empirical values are used for the stator steel in the FE TMS analysis.

The complex geometry and variations of the winding composite is not as straightforward to calculate using the electrical resistance analogy. Instead, a literature review and a separate FE analysis of the winding composition is evaluated in the following chapter. This especially applies to the litz wire, as it not only follows the same complex geometry as straight windings, but the twisting effect will break with the previous assumption of the constant cross-section, adding a 3D contribution to the anisotropic thermal conductivity. This is further discussed in section 7.3.

[12] Cousineau et al. 2015.

Chapter 7

Winding Homogenization Models

As stated in the previous chapter, it is often necessary to simplify the complex composition of winding in order to cut computation costs. A good engineering homogenization model has to be chosen which factors in geometry and the individual materials, being able to capture the realistic bulk thermal properties of the composite.

Generally speaking, the overall performance is determined by the individual constituents and the geometry, dictating how they interact. This generalization is still subject to a number of different parameters such as relative size, shape and arrangement, and as such, various studies have devised separate methods to estimate the bulk properties of composite materials. In the following sections, some of these are presented and discussed, comparing their ability to accurately model the behaviour of the total winding pack.

In the case of the electrical winding in an electric machine, an important geometric parameter is the packing factor (PF), which is the ratio between the metallic conductor cross section area and the total slot area:[1]

$$PF = \frac{A_C}{A_{sl}} \tag{7.1}$$

A high amount of wires is desirable since more current can pass through the winding, as it can be more distributed throughout the cross-section. This will increase the power and efficiency of the motor. In addition, since the thermal conductivity of metals typically are 10^4 higher than that of insulating materials,[2] a higher fraction of copper will lead to a higher bulk conductivity, which in turn will decrease the temperature gradients within the slot.

However, the insulation cannot be removed entirely ($PF < 1$), as this will lead to short circuiting of the machine. This added material will remove space in the slot which could

[1] Hanselman 2006.
[2] Incropera et al. 2013, p. 71.

potentially have been filled with copper. Additionally, since the conductors are of a certain shape and size, it is difficult to ensure that they fit perfectly into the allotted space when they are wound, leaving gaps. Therefore, the packing factor will typically lie somewhere between 40-60% depending on the motor application, wire manufacturing technique, tolerances and assembly.[3] New and improved manufacturing methods are able to push PF towards 80%.[4]

Nevertheless, for a given wire strand diameter and insulation thickness, the packing factor is a defining parameter for the behaviour of the total winding, and as such will be an important criteria when evaluating the models

Because of their composition, the winding's bulk thermal conductivity is highly anisotropic and has to be modelled as such. The most common way to represent this is by having one value (longitudinal, k_λ) along the strands and one across the cross-sectional plane (transverse, k_τ).

7.1 Longitudinal Conduction

Assuming that the cross-section of the wire bundle remains constant through the axial length and considering steady state 1D longitudinal conduction, it can be shown that the heat flux will diverge and flow through the different components corresponding to their materials' respective thermal conductivity. This phenomena is comparable to that of a parallel circuit of resistances, and infers that by using the thermal resistance analogy, an equivalent thermal circuit can be constructed and a total resistance can be expressed by following Ohm's law:[5]

$$\mathbb{R}_i = \frac{L}{k_i A_i} \tag{7.2}$$

$$\mathbb{R}_\lambda = \left[\sum \frac{1}{\mathbb{R}_i}\right]^{-1} \tag{7.3}$$

$$k_\lambda = \sum k_i \frac{A_i}{A_{sl}} \tag{7.4}$$

Assuming the fraction of cross-sectional surface of the wire insulation is small compared to the copper and encapsulant, the longitudinal conduction simply reduces to:

$$k_\lambda = k_E + (k_C - k_E)PF \tag{7.5}$$

Though this linear model does not capture the details, such as the insulation layer, it will be sufficient to evaluate the general temperature profile in the axial direction.

[3] Idoughi et al. 2011.
[4] Ayat et al. 2018.
[5] Incropera et al. 2013, p. 117.

7.2 Transverse Conduction

In the following section, a number of previously devised methods are described briefly. Their full description and derivation are found in their respective papers, cited in the footnotes. The corresponding formulas plotted later in figure 7.3 are found in appendix A.12.

The transverse heat conduction through a composite material such as conductor fibers in an insulating matrix is a more complex issue, as the resulting thermal network is highly dependent on the shape and size of the wire strand geometry and arrangement. This interaction has been studied both analytically,[6] experimentally[7] and numerically,[8] yielding different lumped conductivity formulas. These will be presented and compared to a FE simulation for validation.

7.2.1 Existing Models

Though analytical expressions for the material properties of composites can be traced back to the 19^{th} century, the study of modern, matrix-fiber arrangements follow the introduction of such materials in the middle of the 20^{th} century.[9] Hashin and Shtrikman were among the first to devise a method for homogenizing the conductivity of a series of circular fibers in a continuous matrix phase.[10]

This general formula was later corrected to better account for the arrangement of the composite constituents by Milton,[11] including a microstructural geometry parameter, ξ, adjusting for the material composition, which in this case is that of randomly distributed, circular fibers within a continuous matrix.[12] The ξ-values have been tabulated by Torquato and Lado for different geometries.[13]

Both these expressions concern the inclusion of an amount of homogeneous fibers within a consistent matrix, defined by their respective thermal conductivities and the volumetric ratio within the composition. In the case of electrical windings, however, it is also important to consider the inclusion of wire strand insulation, which, though mostly negligible in relative size, typically has a much lower conductivity than common epoxy resins used as encapsulant, and thus impedes the transverse heat conduction. Hashin and Shtrikman and Milton's two-phase simplification will be more suitable for low conductivity matrices, but will give overestimates if the thermal conductivity is different between the insulation and encapsulant, and/or if the insulation thickness is relatively large compared to the conductor

[6] Ayat et al. 2018; Hashin 1972; Jaritz and Biela 2013; Milton 1981; Simpson, Wrobel, and Mellor 2013; Wrobel, Ayat, and Baker 2017.

[7] Boglietti, Cavagnino, and Staton 2008; Boglietti et al. 2015; Delhommais et al. 2018; Jaritz and Biela 2013; Simpson, Wrobel, and Mellor 2013; Staton, Boglietti, and Cavagnino 2003; Wrobel, Ayat, and Baker 2017; Yi et al. 2019.

[8] Ayat et al. 2018; Idoughi et al. 2011; Simpson, Wrobel, and Mellor 2013.

[9] Hashin 1983.

[10] Hashin and Shtrikman 1962; Hashin 1972.

[11] Milton 1981.

[12] Idoughi et al. 2011.

[13] Torquato and Lado 1988.

strands.

This issue has been addressed by Simpson, Wrobel, and Mellor, proposing a "double-homogenization". This is done by first finding a relationship between the "non-conductor" materials' volumetric ratio and thermal conductivity, creating a corrected, "homogeneous" matrix which can be used in Hashin and Shtrikman's original equation. This method has proven to accurately predict the transverse thermal conductivity up to a packing factor of about 50%, though a comparison with FEA and experimental results shows that the model will overestimate the k_τ-value beyond this point.[14]

For high packing factors, Ayat et al. has proposed a separate formula based on thermal resistance networks to calculate the equivalent thermal conductivity. This formula also takes into account the influence of the insulation layer. The resulting estimates have given good correlation with experimental data, with a maximum error of 10% and showing improvement on the models provided by Hashin and Shtrikman and Simpson, Wrobel, and Mellor at $PF > 50\%$.[15]

The most recent model comes from Liu et al., using the same, double-homogenization approach as Simpson, Wrobel, and Mellor, and creating "wire-and-insulation" equivalent conductivity before inserting this into the formula from Hashin and Shtrikman. In comparison with FEA in the original paper, as well as with the other methods in figure 7.3's analysis, the expression provides a good correlation with more detailed data, both for low and high packing factors.

One certain aspect neither of these models are properly able to capture imperfections from manufacture and the influence on heat transfer from applying it to an actual machine. Small disturbances such as surface roughness and air bubbles in the impregnation have a relatively large influence on the heat transfer compared to their size. If there exists air cavities in the encapsulating resin as a result of the impregnation process, the poor heat transfer characteristics of the trapped gas will lower the overall thermal conductivity. However, it is difficult to predict the amount, size and location of such disturbances, and may lead to large statistical models at high computational cost. One way to fix this specific issue is to factor in an "impregnation goodness" and thermal contact resistances at the winding slot boundaries, though the only way to accurately predict their values is by obtaining experimental data.[16]

An experimental study is shown as an example, provided by Staton, Boglietti, and Cavagnino. The problem with these values, on the other hand, is that empirical models are often machine specific due to the large variations in geometry, materials etc. in electric motors which lead them to be more suitable if measurements have already been made on similar components. These experiments were done on a motor with a specific slot geometry using air as encapsulant and $PF \in \langle 35\%, 45\% \rangle$. As a consequence, the measured

[14] Simpson, Wrobel, and Mellor 2013.
[15] Ayat et al. 2018.
[16] Boglietti, Cavagnino, and Staton 2008; Staton, Boglietti, and Cavagnino 2003.

results fit best in when compared to the analytical values using the same parameters as input. This is shown in figure 7.3c, where as long as $PF < 45\%$, the linear regression corresponds well with the other models.

7.2.2 Numerical Model

The goal of this analysis is to find an overall transverse conductivity, k_τ, for a bundle of insulated wires in a matrix. The methods mentioned in the previous sections have derived simplified, analytical expressions to approximate the k_τ-value. Alternately, numerical analysis can be used to evaluate the heat diffusion equation[17] and simulate experiments using different geometries, packing factors, and component thermal conductivity. This is a relatively cheaper and less time consuming approach to acquiring large amounts of data through experiments, though it is often more complex than applying analytical methods and may be less accurate than empirical results.

The proposed FE model simulates a circular wire bundle with a fixed number of wire strands, each covered in a thin layer of insulating varnish and encapsulated in a homogeneous matrix of a specific material. Each strand produces a certain amount of volumetric heat generation, which is transferred through the bundle to the outer surface, which is kept at $0K$. Since the amount of conductors is a set number, expanding or contracting the bundle outer radius will either decrease or increase the packing factor. Finally, the overall thermal conductivity could be expressed by solving the heat diffusion equation with heat generation, as stated by Incropera et al.:[18]

$$T(r) = \frac{\dot{q}' R_B^2}{4k_\tau}\left(1 - \frac{r^2}{R_B^2}\right) + T_s \tag{7.6a}$$

$$k_\tau = \frac{\dot{q}' R_B^2}{4\left[T(0) - T_s\right]} \tag{7.6b}$$

Where the modified heat generation is a result of the heat solely being generated in the copper part of the cross-section:

$$\dot{q}' = PF \cdot \dot{q} \tag{7.7}$$

Since the arrangement of the different conductor strands in relation to each other affect both the heat flux and the packing factor, it is important to consider this when setting up the FE model. After all, this representation is supposed to imitate the actual bundle geometry. In this case, the model assumes that all the strands are placed in an ordered array, either orthogonal (each center fitting onto the intersections of a square grid) or orthocyclic (each center located on the corners of an equilateral triangle). In reality, perfect patterns such as these are hard to achieve, and a more random distribution is found, especially at lower packing factors. However, this is not necessary to mirror in the numerical simulation, since the arrangement will not have a significant influence until the insulation layer

[17] Incropera et al. 2013.
[18] Incropera et al. 2013, p. 150.

is compacted. This is shown in figure 7.3 and is further discussed in subsequent sections.

Considering insulated, circular wires in a matrix, the lowest and highest packing factors are achieved for an orthogonal and an orthocyclic array, respectively, assuming a tightly packed, uniform pattern, as shown in figure 7.1.

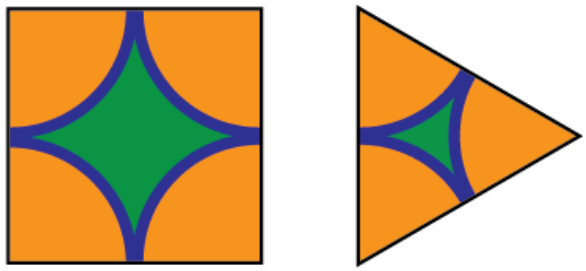

Orange: conductors; blue: insulation; green: encapsulant.

Figure 7.1: Wire arrangements; orthogonal (left) and orthocyclic (right).

Calculating the packing factors for these two cases is a matter of geometry, and reduces to:

$$PF_{\square} = \frac{\pi R_C^2}{4R_{ws}^2} \qquad \lim_{t_{in}\to 0} = \frac{\pi}{4} \approx 78.5\% \tag{7.8}$$

$$PF_{\triangle} = \frac{\pi R_C^2}{2\sqrt{3}R_{ws}^2} \qquad \lim_{t_{in}\to 0} = \frac{\pi}{2\sqrt{3}} \approx 90.7\% \tag{7.9}$$

$$R_C : \text{Conductor radius} \tag{7.10}$$

$$R_{ws} : \text{Wire strand radius} \tag{7.11}$$

The FE model was run in a loop for increasing $PF \in \langle 0.1, 0.8 \rangle$, starting with a large distance between each strand, gradually contracting until the limit where separate conductors touch each other. The model geometry for both the orthogonal and orthocyclic arrays are shown in figure 7.2. These were studied separately, and the results were plotted against the analytical models discussed in the previous section.

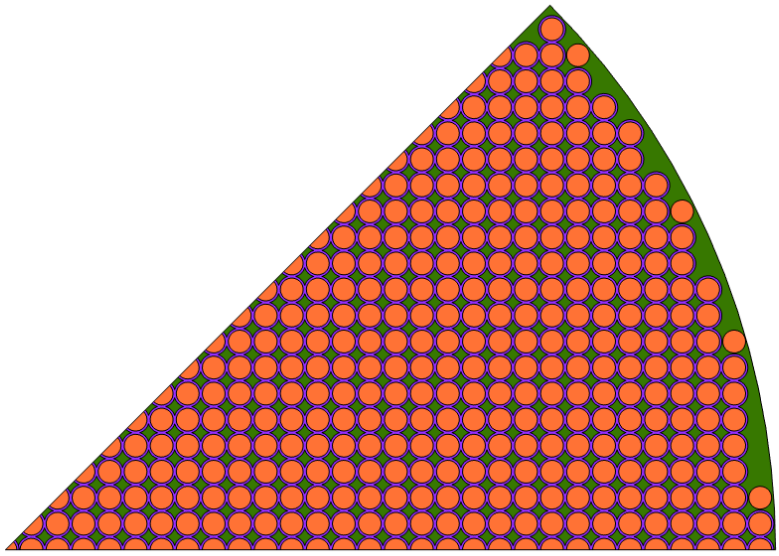

(a) Orthogonal array.

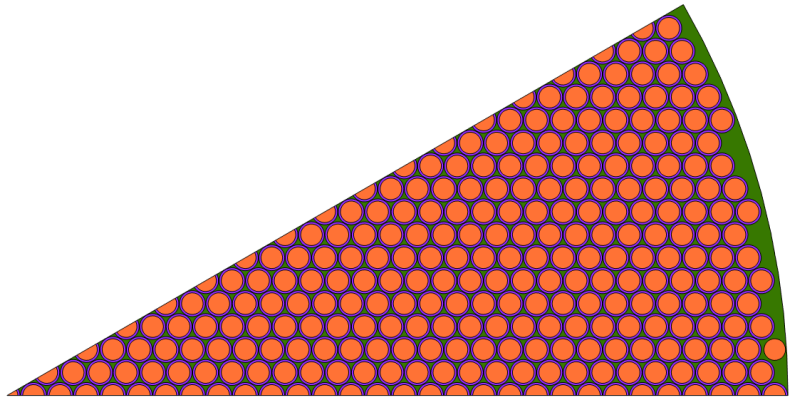

(b) Orthocyclic array.

Figure 7.2: COMSOL transverse conductivity model.

7.2.3 Model Comparison

Below, in table 7.2, a list of k_τ-models (in terms of packing factor, PF) are presented, their formulas indexed in appendix A.12. In addition, two separate numerical FE simulations were run in COMSOL for orthogonal and orthocyclic strand arrangements and combined with equations (7.6b) and (7.7) to provide equivalent conductivities at different packing factors. Considering equivalent wire bundles, the values plotted against PF is shown in figure 7.3. Additionally, experimentally measured values for different winding compositions are given in table 7.1 which are compared to both the relations from the literature and the FE simulation.

The choice of materials used will greatly affect the heat transfer characteristics as well as the electric properties. Using components with good thermal conductivity might be in conflict with their insulating abilities, as these phenomena are linked.[19] Commonly used windings in the present day use either varnish or epoxy as their encapsulant material, and for small machines, the impregnation of the windings is sometimes skipped and air is considered as the matrix substance instead. This gives a range of the encapsulant thermal conductivity, $k_E \in [0.03, \sim 1]\ \frac{W}{mK}$.[20]

Other materials may also be used, depending on the choice of conductor wire, application or if special heat diffusion considerations have to be taken, some of which may increase the overall thermal conductivity.[21] In the following model comparison (figure 7.3), only air, epoxy and varnish are considered, as the scope of this analysis is to match the simplified expressions with more detailed FE simulations and experimental measurements. A benefit of testing air as an encapsulant is that it gives a lower estimate for k_τ as if the impregnation process is unable to fill the slot, equivalent to a poor impregnation goodness.

Data source	$\boldsymbol{k_\tau}\ [\frac{W}{mK}]$	$\boldsymbol{PF}[1]$	$\boldsymbol{k_E}\ [\frac{W}{mK}]$	$\boldsymbol{k_C}\ [\frac{W}{mK}]$
Simpson et al.(I)	2.6 ± 0.1	60%	0.85	385
Simpson et al.(II)	2.4 ± 0.1	55%	0.85	234
Ayat et al. (I)	2.1 ± 0.1	55%	0.85	385
Ayat et al. (III)	2.4 ± 0.2	66%	0.85	234
Ayat et al. (VI)	2.0 ± 0.1	80%	0.03	234
Wrobel et al.(I)	1.4 ± 0.2	64%	0.44	385
Wrobel et al. (III)	1.5 ± 0.2	60%	0.44	385
Wrobel et al. (IV)	3.4 ± 0.7	60%	0.85	385

Table 7.1: Experimental data.
All samples are considered to have a $35\,\mu\text{m}$ insulation layer with $k_I = 0.26\frac{W}{mK}$ and conductor radius of 0.8mm. This is a slight variation in some cases from the actual data, but the difference is assumed negligible.

[19] Hanselman 2006; Incropera et al. 2013.
[20] Ayat et al. 2018; Idoughi et al. 2011; Jaritz and Biela 2013; Liu et al. 2019; Nategh et al. 2014; Simpson, Wrobel, and Mellor 2013; Staton, Boglietti, and Cavagnino 2003; Wrobel, Ayat, and Baker 2017; Yi et al. 2019.
[21] Ayat et al. 2018; Guechi et al. 2013; Nategh et al. 2014; Simpson, Wrobel, and Mellor 2013.

Model	Equation (ap. A.12)	Description
Staton, Boglietti, and Cavagnino	$k_\tau(PF)$ - (A.14)	Linear regression based on experimental data from stator slots of induction motors. Encapsulant: air.
Hashin and Shtrikman	$k_\tau(PF, k_C, k_E)$ - (A.15)	Analytical model of fiber reinforced material, not considering packing or fiber cross-section. No wire insulation.
Milton	$k_\tau(PF, k_C, k_E, \xi)$ - (A.19)	Analytical model of fiber reinforced material, corrected for random distribution. No wire insulation.
Simpson, Wrobel, and Mellor	$k_\tau(PF, k_C, k_E, k_I, R_C, t_I)$ - (A.24)	Analytical model of fiber reinforced material, using a double homogenization to include wire strand insulation.
Ayat et al.	$k_\tau(PF, k_C, k_E, k_I, R_C, t_I)$ - (A.28)	Analytical model of compressed, fiber reinforced material. Including wire strand insulation.
Liu et al.	$k_\tau(PF, k_C, k_E, k_I, R_C, t_I)$ - (A.29)	Analytical model of fiber reinforced material with double homogenization.
Jaritz and Biela (orthogonal)	$k_\tau(PF, k_C, k_E, k_I, R_C, t_I)$ - (A.33)	Analytical formula based on the thermal resistance between wire strands in an orthogonal, closely packed array.
Jaritz and Biela (orthocyclic)	$k_\tau(PF, k_C, k_E, k_I, R_C, t_I)$ - (A.39)	Analytical formula based on the thermal resistance between wire strands in an orthocyclic, closely packed array.
FE (orthocyclic)	$k_\tau(PF, k_C, k_E, k_I, R_C, t_I)$ - (N/A)	Numerical simulation of an orthogonal array for different packing factors.
FE (orthocyclic)	$k_\tau(PF, k_C, k_E, k_I, R_C, t_I)$ - (N/A)	Numerical simulation of an orthogonal array for different packing factors.

Table 7.2: Winding homogenization models comparison.

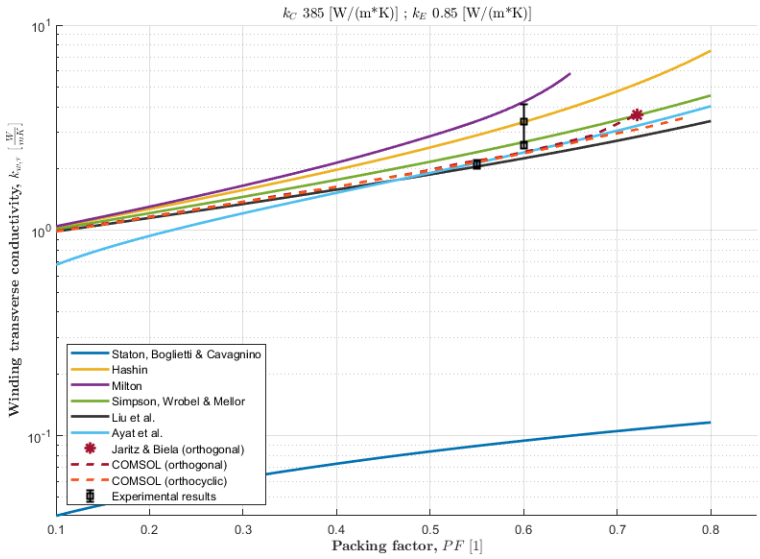

(a) Copper conductor in epoxy.

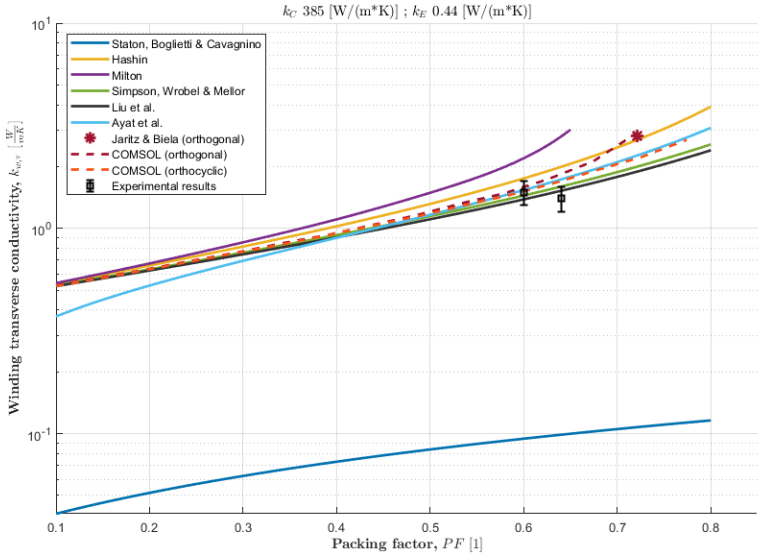

(b) Copper conductor in varnish.

Figure 7.3: k_τ - model comparison. Expressions used found in appendix A.12.

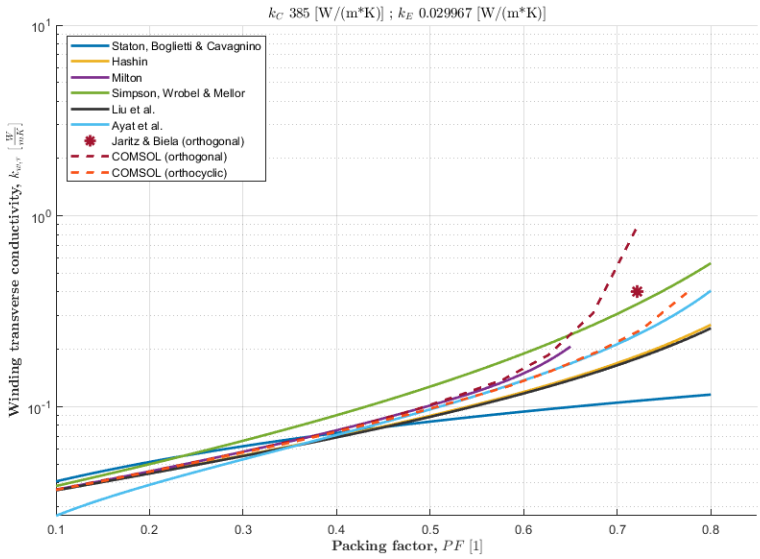

(c) Copper conductor in air.

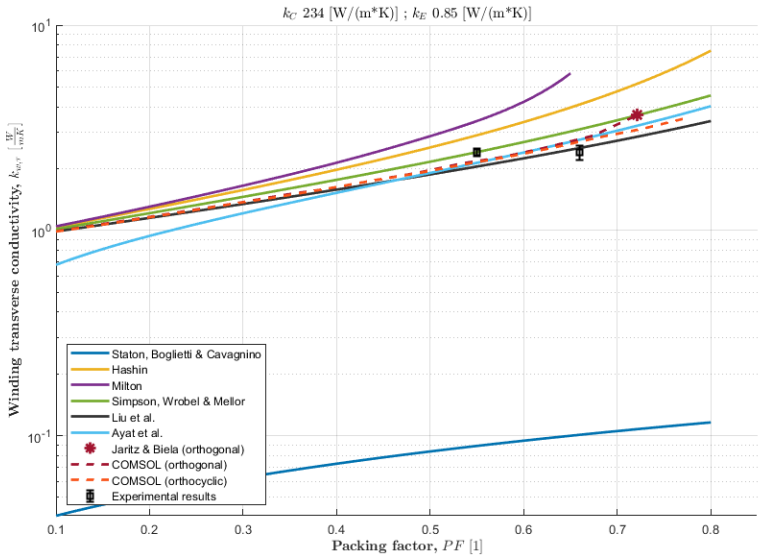

(d) Aluminium conductor in epoxy.

Figure 7.3: k_τ - model comparison (cont.). Expressions used found in appendix A.12.

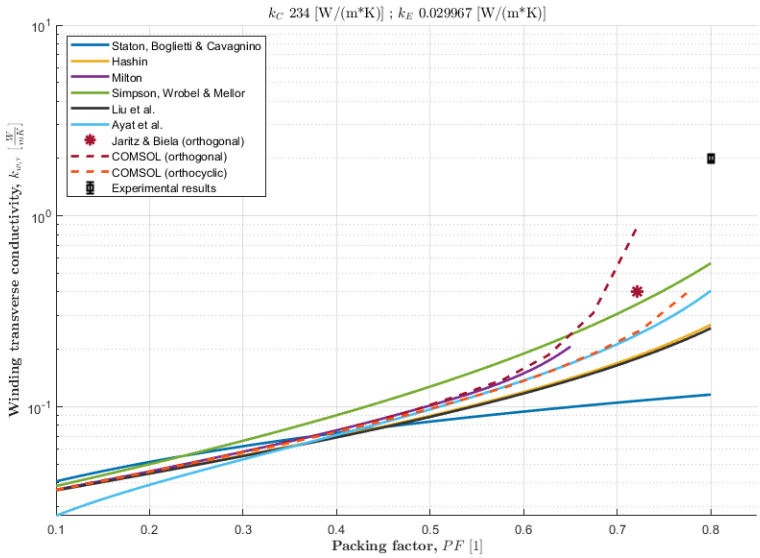

(e) Aluminium conductor in air.

Figure 7.3: k_τ - model comparison (cont.). Expressions used found in appendix A.12.

As figure 7.3 shows, all of the k_τ-models fall within the same range, except for the relation from Staton, Boglietti, and Cavagnino (dark blue line). This is due to the fact that this expression is based on a linear regression from experimental measurements of conductors in an air matrix, and will only give comparable results when the model setup is comparable, i.e. in figures 7.3c and 7.3e. Though in these cases it does show good correlation with other data up to about 0.4 PF, the limitations of this model render it unsuitable for most other applications.

Neither of the models from Hashin and Shtrikman (yellow line) and Milton (purple line) take into account the insulation layer. As a consequence, the insulating effect of $k_I < K_E$ (figs. 7.3a, 7.3b, 7.3d), or the increase of heat transfer from $k_I > K_E$ (figs. 7.3c, 7.3e) are not accounted for. This leads to an either overestimation or underestimation of the transverse conductivity proportional to the relation between the encapsulant and insulation layer conductivity.

The two FE geometries show good consistency in their reporting of k_τ-values up to a point at approximately 0.6 PF, indicating that up until this point, the stacking arrangement of the individual wire strands has negligible effect. The lines will however diverge as the compression of the winding block reaches the maximum theoretical limit (eqs. (7.8) & (7.9)), especially in the case of a poor encapsulant conductor such as air (figs. 7.3c, 7.3e). When reaching this geometrical limit, the wire strands are sufficiently close to each other that the heat flux will more or less bypass the matrix altogether. On the other hand, the orthogonal array (red, dashed line) is not as realistic at such high packing factors, as the wires have

a much more stable configuration in an orthocyclic array (orange, dashed line). By this logic, the true k_τ will lie closer to the lower FE simulation.

While discussing the phenomena of compacting the strand array to their limits, it can be observed from figure 7.3e that the experimentally measured result reports a value of $2.0 \pm 0.1 \frac{W}{mK}$ at 0.8 PF. This lies well above what is estimated by the other expressions, but does follow the same trend as the FE simulations. The report with this high k_τ-value also noted that the increase in PF from compressing the windings would also to some degree deform the individual wire strands, thus causing the drastic increase in thermal conductivity, and may also increase electromagnetic performance.[22]

The other experimental data correlate well with the analytical models, indicating a good connection between model and reality. Discrepancies can be explained by the high amount of both geometric and material property parameters affecting the results, as well as the manufacturing variance and measuring uncertainty. Cases of $k_{\tau,exp} < k_{\tau,mod}$ can be explained by the influence of air cavities (impregnation goodness).

Considering the more modern relations by Simpson, Wrobel, and Mellor (green line), Ayat et al. (light blue line) and Liu et al. (black line), these models correlate quite well with both the experimental measurements and the COMSOL FE simulations. Considering that these expressions are quick to use and provide decent accuracy, these are the most economical option when using in more complex FE model compositions such as an electrical machine. All the same, there are some differences between them, as they are valid for different ranges of PF.

Both Simpson, Wrobel, and Mellor's and Liu et al.'s expressions use the double homogenization based on Hashin and Shtrikman's original equation. The differences in value relate to their method of weighing the contributions of insulator and encapsulant thermal conductivity in the amalgamation. Liu et al.'s model follows more closely to the FE model, indicating better accuracy.

The Ayat et al. relation is derived based on thermal equivalent resistance theory, creating a network of wire strand, insulation layer and encapsulant matrix resistors. As can be seen in figure A.28, this simplification does not hold at lower packing factors, where the double homogenization models are more valid. However, in modern electrical machines, the aim is to achieve high conductor density, at which the thermal network model proves more accurate. It is this relation that is used in the FE TMS analysis.

7.3 Litz Wire & Transposition Effect

Litz wire is commonly used in high frequency machines, as they help mitigate some of the copper losses. They are distinguished from other conductors by their large number of

[22] Ayat et al. 2018.

small diameter strands woven or twisted together to form a larger bundle.[23] The thin wires allow for higher fill factors, especially since manufacturers are able to create compacted bundles made to fit better with the rectangular slot of the electrical machine.[24] While increasing the electromagnetic performance, this will also benefit the homogeneous thermal conductivity, as is shown in the preceding sections.

An added effect to the heat transfer is the twisting of the wires themselves. An example is shown in figure 7.4. Considering the heat transfer from side A of the bundle to B, this can happen through two distinct paths:

i. Directly transverse, through the cross section via low thermal conductivity, k_τ (calculated through methods discussed above)

ii. Following the metal conductor wire until it twists through to side B' via higher thermal conductivity, k_C

The second option is what is referred to as the transposition effect.[25]

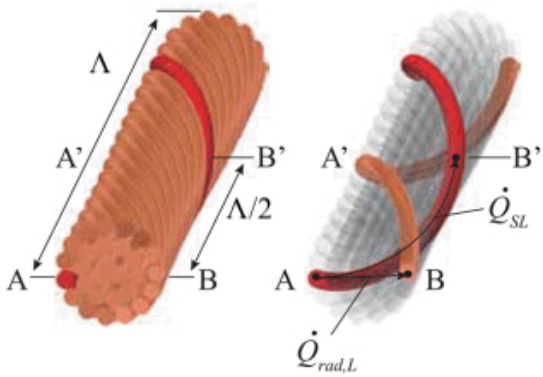

Source: Jaritz and Biela 2013.
Figure 7.4: Litz wire heat transfer paths.

In its simplest form, this reduces to two parallel paths with distinct thermal resistances:

$$\mathbb{R}_\tau = \frac{D_B}{k_\tau A_{AB}} \qquad \text{from point A to point B} \tag{7.12}$$

$$\mathbb{R}_C \approx \frac{\Lambda}{2k_C A_{ws}} \qquad \text{from point A to point B'} \tag{7.13}$$

The total transverse resistance, $\mathbb{R}_{\tau,\text{litz}}$, can then be evaluated through equation (6.3), following Kirchhoff's laws of resistance networks.

[23] Agile Magnetics 2017.
[24] Wereszczak et al. 2017; New England Wire Technologies 2017.
[25] Yi et al. 2019.

Though this is a slight oversimplification, it shows the underlying principle and the order of magnitude of the two routes. The ratio $\frac{\Lambda}{k_C}$ is a deciding factor whether $\mathbb{R}_C$ is sufficiently low as to allow most of the heat pass through the conductors. Since k_C typically is quite high ($k_{copper} \sim 400\frac{W}{mK}$), path ii. shows potential, yet on the other hand the bundle diameter, D_B is small when compared to the pitch length, Λ.[26]

The reality is not as simple. The interaction between separate wire strands and heat generation within the wire forms a complex network of heat transfer paths that is yet to be generalized in a ready-to-use expression. Litz wire geometry varies according to different classes and manufacturers, as is exemplified by figure 7.5. The dimensions of the bundle, especially the compacted types (figures 7.5g & 7.5h) may be custom made for the specific application.[27]

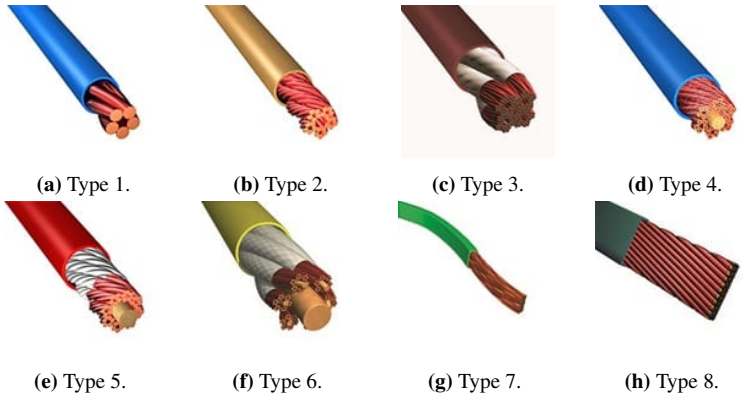

(a) Type 1. **(b)** Type 2. **(c)** Type 3. **(d)** Type 4.

(e) Type 5. **(f)** Type 6. **(g)** Type 7. **(h)** Type 8.

Source: New England Wire Technologies 2017.
Figure 7.5: Litz wire types.

Two studies found in the literature have made separate attempts on accounting for the transposition effect in litz wire.[28] Both these reports utilized a complex thermal resistance network to solve the problem, using computer software to simplify the systems and calculate $\mathbb{R}_{\tau,\text{litz}}$. As noted previously, these methods are made for specific bundle geometries, and do not simply generalize. The technique itself seems at this point too dependent on the specific litz wire composition, requiring it to be modified for each reiteration. This would prove cumbersome as engineering tools for homogenization in FE analysis.

It must be noted, however, that the most recent study by Yi et al. is published only a year prior to the current thesis, and has by experimental verification found an analytical thermal network model for rectangular litz wire with good correlation to real life results.[29] The report is only a conference paper, indicating that there may be a more detailed article

[26] *Litz Wire Calculation & Design*.
[27] New England Wire Technologies 2017.
[28] Jaritz and Biela 2013; Yi et al. 2019.
[29] Yi et al. 2019.

put out in the future. Though the current project was unable to re-create the data, the described method should potentially prove a good starting point for a more in-depth study.

Chapter 8

Concluding Remarks

The increasing interest in high speed electrical machines opens new possibilities and presents new cases for both structural, electromagnetic and thermal engineers. This report has studied a proposed prototype concept of a scaled down electric aircraft motor, creating an integrated TMS design in line with the predicted need for more aggressive, efficient cooling systems.[1] A more in-depth analysis has also been made on certain aspects of thermal analysis, namely Taylor-Couette-Poiseuille flow through a stator-rotor air gap and homogenization techniques for electrical windings. This chapter will give a brief summary of the different tasks performed in the project thus far. Based on this, some suggestions for further work are presented.

8.1 Thermal Management System Design

A prototype, compact, high-speed electric motor prototype has been designed, purposed for testing new machine configurations for aircraft application. Strict requirements are put on performance on every aspect of its construction, electromagnetic, mechanic and thermal. While the first two are covered in other reports,[2] the thermal management system has been created and evaluated in this work.

Multiple options for cooling the motor have been presented from literature and discussed. Based on the machine topology, the two most practical, yet efficient concepts have been chosen for further evaluation:

I. A closed-loop oil cooling system with channels on the inside and outside surfaces of the stator, combined in series (oil TMS)

II. An open-loop air cooling system with a parallel flow through the inside and outside channels (air TMS)

[1] Tüysüz et al. 2017; Yi and Haran 2019; Zhang et al. 2018.
[2] Fossum 2020; Verde 2020.

The heat sink geometry is synthesized from previous work[3] and literature,[4] using the available space in the machine to create a distributed ducting system combining direct and indirect cooling.

The inner surface of the stator has been modified to include fins in order to increase heat transfer. The outer heat sink would be either the gap between the tooth tips (opt. I.) or through the stator-rotor air gap (opt. II.), where the slight difference is due to the closed or open loop configurations.

Both systems were simulated using a FE model of the same machine geometry, materials and heat generation. The oil cooling flow was possible to implement directly in the numerical software through CFD, while to save computational time, the turbulent air flow was implemented as boundary heat transfer correlations. A study was then run to evaluate the two alternatives' performance, including a sensitivity analysis on the oil configuration.

The following conclusions can be drawn from the thermal study of the two configurations:

1. Both are able to adequately cool the machine at relatively low pump/fan power requirements ($\leq$ 30W)
2. The main material limitation in this motor is the demagnetisation temperature in the rotor magnets (90°C)
3. The outer heat sink is responsible to keep requirement 2, and ensure that no heat flux passes from the stator to the rotor
4. The heat losses and the coolant mass flow rate have the greatest significance in the TMS performance. Geometry and material parameters are less significant

The main finding (item 1) indicates that the axial forced convection cooling ducts provide good heat sinks, and that a low mass flow rate is possible due to the distribution of the channels. Increasing the flow is possible without a serious pressure rise in case of higher losses or if a larger safety factor is desired.

Though the heat transfer surface area is significantly larger on the inner, finned surface, the flux to the outer cooling channel is greater, since they are closer to the windings. The cooling of the rotor is achieved through convection on the outer, rotating surface, which is just capable of sustaining the magnet temperature limit as long as the rotor and stator are isolated from each other. This implies that the outer heat sink of the TMS has to ensure this insulation, and that while operating the machine, the cooling flow must absorb all the heat generated by the stator.

Though both versions are capable of ensuring stable operating conditions, many practical considerations such as weight, robustness, manufacturability and integration should be taken to create the optimum electrical machine. A prototype test rig was planned in order

[3] Gjeset 2019.

[4] Huang et al. 2012; Tüysüz et al. 2017; Vlach, Grepl, and Krejci 2007.

to gain hands on experience, calibrate numerical models and tackle some of the unforeseen issues. The building was not carried out within the scope of this project, and the final choice as to which TMS to implement remains for further work.

8.2 Air Gap Relations

Since the air TMS uses the air gap as a cooling channel, a more detailed analysis of the Taylor-Couette-Poiseuille flow and its effect on heat transfer was carried out. A comprehensive literature study has been conducted and multiple relations for air gap heat exchange and windage loss have been presented.

A rotational-symmetric 2D CFD model was simulated in COMSOL over different rotation speeds with and without a varying axial mass flow of air. The results were compared towards correlations found in the literature.

Though the model was able to capture some of the main characteristics of the fluid movement, the simplified model did not seem to fully detail the flow structures, and is believed to underestimate the heat and momentum transfer. Despite its deficiencies, the model itself proves the potential in using the air gap as a cooling channel, as the combined rotation and axial flow of the air provides good heat transfer characteristics, the space is open and available to use, and the heat sink provides cooling for both the stator and rotor. The correction of the CFD study and the in-depth, detail analysis of the air gap flow is left for further work.

8.3 Homogenization Techniques

The winding ”block” is a composite structure consisting of multiple materials and small components. This may prove time consuming to model in all its detail in a FE study of an electrical machine. Instead, the material is homogenized into a single substance with the bulk characteristics of the composite. The problem remains finding a good expression for the bulk material properties based on the constituents.

The study has presented multiple relations found in the literature for the transverse thermal conductivity of a bunch of individually insulated conductors in a homogeneous encapsulant matrix (the winding block). These have been compared to a 2D FE model of the same geometry, as well as experimentally measured values also found in previous reports.

The results indicate that the most recent, double homogenization model from Liu et al. is the most accurate for low packing factors, while Ayat et al.’s relation works better at higher packing factors. Very high copper density ($\sim$70-80%) found in compacted bundles will lead to a compression and deformation of the components, which will induce a significant increase in k_τ that neither of the established models are able to express.

A brief study of litz wire geometry has also been conducted, describing the increase in k_τ due to the transposition effect created by the twisted/braided wire strands. A literature survey has indicated that thermal resistance networks and 3D FE models are most suitable for these kind of composites, but these relations are more configuration and geometry specific and do not readily lend themselves to engineering correlations.

8.4 Further Work

This project has uncovered much potential in the future work concerning higher fidelity thermal models and better integrated cooling systems in HSP electrical machines. A better understanding of the underlying concepts of the heat exchange mechanisms is needed in order to better predict their application and effect.

The following points are presented as suggestions for further studies:

I. An experimental test of the prototype in order to calibrate numerical models and earn practical experience

II. Combining the different models from the team in order to perform cross disciplinary analysis of combined effects and multi-dimensional optimization

III. An in-depth study of the Taylor-Couette-Poiseuille flow in the air gap, improving the CFD model

IV. A screening of the cooling systems in their entirety, evaluating the mass, added drag, pump/fan requirements etc.[5]

V. Cooperating with electromagnetics to study the the impact of cooling channel location, weighing direct cooling benefits against performance losses[6]

VI. A fin/cooling channel optimization study

VII. Using either thermal resistance networks or FE numerical models to investigate the transposition effect of litz wire

VIII. Investigating other potential cooling mechanisms to have a more complete library of compact thermal management systems

IX. Thermal risk assessment of the machine

The main focus of this work has been to relate the various thermal modelling aspects (FE-analysis and calibration, flow/heat transfer relations and composite homogenization) to the prototype ER machine in order to highlight the necessity of proper knowledge of the underlying concepts. The work has in this manner only briefly discussed each facet, whereas

[5] Hepperle 2012.
[6] Demerdash, Garg, and Hamilton 1975; Özoğlu 2016.

the deeper understanding needs to be covered in more detail focused analysis. Though simply accepting the present correlations and creating TMS solutions for electrical machines is possible, the further advancement and higher performing systems is best achieved by in-depth evaluation, which may in turn lead to the necessary technology advancements needed to drive the mass implementation of electrical aircraft.

Bibliography

Agile Magnetics (Aug. 2017). *Litz Wire: An Ideal Solution for High-Frequency Applications*. URL: https://www.agilemagco.com/blog/5-benefits-of-using-litz-wire/ (visited on 03/17/2020).

Airbus (2018). *The Future is Electric*. URL: https://www.airbus.com/newsroom/news/en/2018/07/the-future-is-electric.html (visited on 12/05/2019).

– (2019). *E-Fan X - A Giant Leap Towards Zero-Emission Flight*. URL: https://www.airbus.com/innovation/future-technology/electric-flight/e-fan-x.html (visited on 12/05/2019).

– (2020). *Our decarbonisation journey continues: looking beyond E-Fan X*. URL: https://www.airbus.com/newsroom/stories/our-decarbonisation-journey-continues.html (visited on 04/28/2020).

Alam, I. and P.S. Ghoshdastidar (2002). "A Study of Heat Transfer Effectiveness of Circular Tubes with Internal Longitudinal Fins Having Tapered Lateral Profiles". In: *International Journal of Heat and Mass Transfer* 45, pp. 1371–1376.

Armstrong, R.C. et al. (Jan. 2016). "The Frontiers of Energy". In: *Nature Energy* 1.15020.

Ayat, S. et al. (Sept. 2018). "Estimation of Equivalent Thermal Conductivity for Electrical Windings with High Conductor Fill Factor". In: *2018 IEEE Energy Conversion Congress and Exposition (ECCE)*, pp. 6529–6536.

Ayat, S. et al. (2019). "The Use of Phase Change Material for the Cooling of Electric Machine Windings Formed with Hollow Conductors". In: *2019 IEEE International Electric Machines Drives Conference (IEMDC)*, pp. 1195–1201.

Becker, K.M. and J. Kaye (May 1962). "Measurements of Diabatic Flow in an Annulus With an Inner Rotating Cylinder". In: *Journal of Heat Transfer* 84.2, pp. 97–104.

Boglietti, A., A. Cavagnino, and D.A. Staton (2008). "Determination of Critical Parameters in Electrical Machine Thermal Models". In: *IEEE Transactions on Industry Applications* 44.4, pp. 1150–1159.

Boglietti, A. et al. (May 2015). "Equivalent Thermal Conductivity Determination of Winding Insulation System by Fast Experimental Approach". In: *2015 IEEE International Electric Machines Drives Conference (IEMDC)*, pp. 1215–1220.

Boglietti, A. et al. (Sept. 2018). "Calibration Techniques of Electrical Machines Thermal Models". In: *2018 XIII International Conference on Electrical Machines (ICEM)*, pp. 1108–1115.

Bouafia, M. et al. (1998). "Analyse expérimentale des transferts de chaleur en espace annulaire étroit et rainuré avec cylindre intérieur tournant". In: *International Journal of Heat and Mass Transfer* 41.10, pp. 1279 –1291.

Boulanger, A.G. et al. (June 2011). "Vehicle Electrification: Status and Issues". In: *Proceedings of the IEEE* 99.6, pp. 1116–1138.

Bunting Magnetics Europe Ltd. *Characteristics of NdFeB Magnets*. URL: https://e-magnetsuk.com/neodymium_magnets/characteristics.aspx (visited on 05/17/2020).

Callister Jr., W.D. (2007). *Materials Science and Engineering: An Introduction*. 7th ed. John Wiley & Sons, Inc. Chap. 16.

Childs, P.R.N (2010). *Rotating Flow*. 1st ed. Elsevier.

Christie, R.J., A. Dubois, and J.M. Derlaga (Apr. 2017). *Cooling of Electric Motors Used for Propulsion on SCEPTOR*. Tech. rep. NASA Glenn Research Center; Cleveland, OH United States: NASA.

COMSOL (2019). *CFD Module User's Guide*. URL: https://doc.comsol.com/5.5/doc/com.comsol.help.cfd/CFDModuleUsersGuide.pdf (visited on 04/25/2020).

Cousineau, J.E. et al. (June 2015). "Characterization of Contact and Bulk Thermal Resistance of Laminations for Electric Machines". In: DOI: 10.2172/1215166.

Dalløkken, P.E. (2017). *Airbus bygger nytt hybridelektrisk fly*. URL: https://www.tu.no/artikler/airbus-bygger-nytt-hybridelektrisk-fly/413022 (visited on 02/18/2020).

– (2020). *Delvis norskutviklet: Airbus og Rolls-Royce skrinlegger hybridfly-prosjekt*. URL: https://www.tu.no/artikler/delvis-norskutviklet-airbus-og-rolls-royce-skrinlegger-hybridfly-prosjekt/490810 (visited on 04/28/2020).

Delhommais, M. et al. (Mar. 2018). "Thermal model of Litz wire toroidal inductor based on experimental measurements". In: *2018 IEEE Applied Power Electronics Conference and Exposition (APEC)*, pp. 2658–2665.

Demerdash, N. A., V. K. Garg, and H. B. Hamilton (July 1975). "Effect of ventilating holes on radial flux and losses in stator slots of turbogenerators". In: *IEEE Transactions on Power Apparatus and Systems* 94.4, pp. 1177–1182.

Dubois, A. et al. (June 2016). "Design of an Electric Propulsion System for SCEPTOR's Outboard Nacelle". In: *16th AIAA Aviation Technology, Integration, and Operations Conference*.

Duffy, M. et al. (July 2018). "Propulsion Scaling Methods in the Era of Electric Flight". In: *2018 AIAA/IEEE Electric Aircraft Technologies Symposium (EATS)*, pp. 1–23.

Dull, B. (Aug. 2019). *What Is Litz Wire and Its Applications*. URL: https://info.triadmagnetics.com/blog/what-is-litz-wire-and-its-applications (visited on 03/17/2020).

Elghnam, R.I. (2014). "Experimental and numerical investigation of heat transfer from a heated horizontal cylinder rotating in still air around its axis". In: *Ain Shams Engineering Journal* 5.1, pp. 177 –185.

Equator Aircraft (2019). *Home - Equator Aircraft*. URL: https://www.equatoraircraft.com/ (visited on 04/25/2020).

Eviation (2019). *ALICE - All Electric – All Ready*. URL: https://www.eviation.co/ (visited on 04/29/2020).

Fabbri, G. (1997). "A genetic algorithm for fin profile optimization". In: *International Journal of Heat and Mass Transfer* 40.9, pp. 2165 –2172.

– (1998a). "Heat Transfer Optimization in Finned Annular Ducts under Laminar-Flow Conditions". In: *Heat Transfer Engineering* 19.4, pp. 42–54.

– (1998b). "Heat transfer optimization in internally finned tubes under laminar flow conditions". In: *International Journal of Heat and Mass Transfer* 41.10, pp. 1243 –1253.

– (2000). "Heat transfer optimization in corrugated wall channels". In: *International Journal of Heat and Mass Transfer* 43.23, pp. 4299 –4310.

Fossum, S.B. (Dec. 2019). *Super-Compact PM Motor for Electric Aviation*. NTNU Norwegian University of Science and Technology.

– (June 2020). "Design and Optimization of a Super-Compact PM-Motor for Aviation Using Genetic Algorithm". MA thesis. Trondheim: NTNU Norwegian University of Science and Technology.

Fénot, M. et al. (2011). “A Review of Heat Transfer Between Concentric Rotating Cylinders with or without Axial Flow”. In: *International Journal of Thermal Sciences* 50.7, pp. 1138 –1155.

Gao, N. and L. Yu (2013). “Research on loss and electromagnetic heat coupling of high speed permanent magnet synchronous motor”. In: *2013 IEEE International Conference on Mechatronics and Automation*, pp. 81–86.

Gjeset, E. (2019). *Cooling of Electrical Aircraft Machines*. NTNU Norwegian University of Science and Technology.

Gorland, S.H., E.E. Kempke Jr., and S. Lumannick (1970). *Experimental Windage Losses for Close Clearance Rotating Cylinders in the Turbulent Flow Regime*. Tech. rep.

Grosgeorge, M. (1983). “Contribution à l’étude du refroidissement d’une paroi tournante par air chargé d’huile pulvérisée”. PhD thesis. Université de Nancy.

Guechi, M. R. et al. (2013). “On the Improvement of the Thermal Behavior of Electric Motors”. In: *2013 IEEE Energy Conversion Congress and Exposition*, pp. 1512–1517.

Hanselman, D. (2006). *Brushless Permanent Magnet Motor Design*. 2nd ed. Magna Physics Publishing.

Hashin, Z. (Mar. 1972). *Theory of Fiber Reinforced Materials*. Standard. NASA; Washington, United States: NASA.

– (Sept. 1983). “Analysis of Composite Materials — A Survey”. In: *Journal of Applied Mechanics* 50.3, pp. 481–505.

Hashin, Z. and S. Shtrikman (1962). “A Variational Approach to the Theory of the Effective Magnetic Permeability of Multiphase Materials”. In: *Journal of Applied Physics* 33.10, pp. 3125–3131.

Hepperle, M (Oct. 2012). “Electric Flight - Potential and Limitations”. In: *Energy Efficient Technologies and Concepts of Operation*. URL: https://elib.dlr.de/78726/.

Heywood, J.B. (1988). *Internal Combustion Engine Fundamentals*. McGraw-Hill, Inc.

Howey, D.A., P.R.N. Childs, and A.S. Holmes (2012). “Air-Gap Convection in Rotating Electrical Machines”. In: *IEEE Transactions on Industrial Electronics* 59.3, pp. 1367–1375.

Huang, Z. et al. (2012). “Direct Oil Cooling of Traction Motors in Hybrid Drives”. In: *2012 IEEE International Electric Vehicle Conference*, pp. 1–8.

Idoughi, L. et al. (Dec. 2011). “Thermal Model With Winding Homogenization and FIT Discretization for Stator Slot”. In: *IEEE Transactions on Magnetics* 47.12, pp. 4822–4826.

Incropera, F.P. et al. (2013). *Principles of Heat and Mass Transfer*. 7th ed. John Wiley & Sons, Inc.

International Organization for Standardization (1975). *ISO 2533:1975, Standard Atmosphere*. Standard.

Jaritz, M. and J. Biela (Sept. 2013). “Analytical model for the thermal resistance of windings consisting of solid or litz wire”. In: *2013 15th European Conference on Power Electronics and Applications (EPE)*, pp. 1–10.

Kahourzade, S. et al. (Sept. 2018). “Estimation of PM Machine Efficiency Maps from Limited Experimental Data”. In: *2018 IEEE Energy Conversion Congress and Exposition (ECCE)*, pp. 4315–4322.

Karim, Z.A.A. and A.H.M. Yusoff (Feb. 2014). “Cooling System for Electric Motor of an Electric Vehicle Propulsion”. In: *Advanced Materials Research* 903, pp. 209–214.

Kays, W.M. and M.E. Crawford (1993). *Convective Heat and Mass Transfer*. 3rd ed. McGraw-Hill, Inc.

Kays, W.M. and A.L. London (1984). *Compact Heat Exchangers*. 3rd ed. McGraw-Hill, Inc.

Kosterin, S. and Y. Finatev (1962). “Heat transfer in turbulent airflow the annular space between rotating coaxial cylinders”. In: *Inzh.-Fiz. Zh* 8, pp. 3–9.

Kristjanson, K. (2019). personal communication.

Larsen, O.M. and J.P. Steinland (Mar. 2020). *Forslag til program for introduksjon av elektrifiserte fly i kommersiell luftfart*. Tech. rep. Avinor & Luftfartstilsynet.

Lilium (2019). *Regional Air Mobility - Lilium*. URL: https://lilium.com/ (visited on 04/25/2020).
Liu, H. et al. (Jan. 2019). "Comparative study of thermal properties of electrical windings impregnated with alternative varnish materials". In: *The Journal of Engineering*.
Loftin Jr., L.K. (1985). *Quest for Performance: The Evolution of Modern Aircraft*. Part II - The jet Age. NASA.
Masson, P.J. et al. (2007). "HTS Machines as Enabling Technology for All-Electric Airborne Vehicles". In: *Superconductor Science and Technology* 20, pp. 748–756.
McFarland, J. D., T. M. Jahns, and A. M. El (Sept. 2015). "Performance and efficiency comparisons for interior PM and flux-switching PM machines with ferrite magnets for automotive traction applications". In: *2015 IEEE Energy Conversion Congress and Exposition (ECCE)*, pp. 6529–6536.
MIDEL (2018). *MIDEL 7131 Thermal Properties*. URL: https://www.midel.com/app/uploads/2018/09/MIDEL_7131_Thermal_Properties.pdf (visited on 12/04/2019).
Milton, G.W. (1981). "Bounds on the transport and optical properties of a two-component composite material". In: *Journal of Applied Physics* 52.8, pp. 5294–5304.
Moran, M. J. and H. N. Shapiro (2006). *Fundamentals of engineering thermodynamics*. 5th ed. John Wiley and Sons Inc., New York, NY.
Nategh, S. et al. (2014). "Evaluation of Impregnation Materials for Thermal Management of Liquid-Cooled Electric Machines". In: *IEEE Transactions on Industrial Electronics* 61.11, pp. 5956–5965.
New England Wire Technologies (2017). *Litz Wire*. URL: https://s3-us-east-2.amazonaws.com/newtcdn/wp-content/uploads/2017/12/02144706/NEWT-Litz-Book_FINAL.pdf (visited on 03/10/2020).
NTB Nyhetsbyrå (2020). *Norske elbiler bidrar til CO2-kutt globalt*. URL: https://www.tu.no/artikler/norske-elbiler-bidrar-til-co2-kutt-globalt/490259 (visited on 04/25/2020).
Petukhov, B.S., T.F. Irvine, and J.P. Hartnett (1970). "Advances in heat transfer". In: *Academic, New York* 6, pp. 503–564.
Petukhov, B.S. and V.V. Kirillov (1958). "On heat exchange at turbulent flow of liquid in pipes". In: *Teploenergetika* 4.4, pp. 63–68.
Poncet, S., S. Haddadi, and S. Viazzo (2011). "Numerical modeling of fluid flow and heat transfer in a narrow Taylor–Couette–Poiseuille system". In: *International Journal of Heat and Fluid Flow* 32.1, pp. 128 –144.
Popescu, M. et al. (May 2016). "Modern Heat Extraction Systems for Power Traction Machines — A Review". In: *IEEE Transactions on Industry Applications* 52.3, pp. 2167–2175.
RClab (2014). *The Basics of Electric Power: Brushless Motors*. URL: http://www.rclab.info/2014/01/the-basics-of-electric-power-brushless.html (visited on 03/06/2020).
Rolls-Royce (2019). *The World's Most Powerful Flying Generator*. URL: https://www.rolls-royce.com/media/our-stories/discover/2019/e-fan-x-continues-to-explore.aspx (visited on 12/05/2019).
Saripally, A. (May 2015). "A Micromechanical Approach to Evaluate the Effective Thermal Properties of Unidirectional Composites". PhD thesis.
Shah, R.K. and A.L. London (1971). *Laminar Flow Forced Convection Heat Transfer and Flow Friction in Straight and Curved Ducts - A Summary of Analytical Solutions*. Office of Naval Research, pp. 116–121.
Simpson, N., R. Wrobel, and P.H. Mellor (Nov. 2013). "Estimation of Equivalent Thermal Parameters of Impregnated Electrical Windings". In: *IEEE Transactions on Industry Applications* 49.6, pp. 2505–2515.
Statistisk Sentralbyrå (2018). *Over 140 000 Electric Cars in Norway*. URL: https://www.ssb.no/en/transport-og-reiseliv/artikler-og-publikasjoner/over-140-000-electric-cars-in-norway (visited on 12/02/2019).

– (2019). *Registered vehicles*. URL: https://www.ssb.no/en/transport-og-reiseliv/statistikker/bilreg (visited on 02/20/2020).
Staton, D.A., A. Boglietti, and A. Cavagnino (July 2003). "Solving the More Difficult Aspects of Electric Motor Thermal Analysis". In: vol. 2, 747 –755 vol.2.
Sullivan, C. R. and R. Y. Zhang (Mar. 2014). "Simplified design method for litz wire". In: *2014 IEEE Applied Power Electronics Conference and Exposition - APEC 2014*, pp. 2667–2674.
Surakitbovorn, K. (Dec. 2016). *Litz Wire*. URL: http://large.stanford.edu/courses/2016/ph240/surakitbovorn2/ (visited on 03/17/2020).
Tachibana, F. and S. Fukui (1964). "Convective Heat Transfer of the Rotational and Axial Flow between Two Concentric Cylinders". In: *Bulletin of JSME* 7, pp. 385–391.
Torquato, S. and F. Lado (1988). "Bounds on the Conductivity of a Random Array of Cylinders". In: *Proceedings of the Royal Society of London. Series A, Mathematical and Physical Sciences* 417.1852, pp. 59–80. ISSN: 00804630. URL: http://www.jstor.org/stable/2398265.
Tüysüz, A. et al. (2017). "Advanced Cooling Methods for High-Speed Electrical Machines". In: *IEEE Transactions on Industry Applications* 53.3, pp. 2077–2087.
Verde, L.H. (Dec. 2019). *Mechanical Design of Electric Demonstrator for E-fan X Hybrid Aeroplane*. NTNU Norwegian University of Science and Technology.
– (June 2020). "Mechanical Design of Electric Demonstrator Motor for E-Fan X and a Study of Dynamics of Rotating Bodies". MA thesis. Trondheim: NTNU Norwegian University of Science and Technology.
Vlach, R., R. Grepl, and P. Krejci (2007). "Control of Stator Winding Slot Cooling by Water Using Prediction of Heating". In: *2007 IEEE International Conference on Mechatronics*, pp. 1–5.
Wereszczak, A.A. et al. (Apr. 2017). "Anisotropic Thermal Response of Packed Copper Wire". In: *Journal of Thermal Science and Engineering Applications* 9.4.
Wikipedia (2020). *Engine efficiency*. URL: https://en.wikipedia.org/wiki/Engine_efficiency#Internal_combustion_engines (visited on 02/19/2020).
Wrobel, R., S. Ayat, and J.L. Baker (May 2017). "Analytical methods for estimating equivalent thermal conductivity in impregnated electrical windings formed using Litz wire". In: *2017 IEEE International Electric Machines and Drives Conference (IEMDC)*, pp. 1–8.
Yang, Y. et al. (2016). "Thermal Management of Electric Machines". In: *IET Electrical Systems in Transportation* 7, pp. 104–116.
YDK. *Litz Wire Calculation & Design*. URL: https://www.hflitzwire.com/litz-wire-calculation-and-design/ (visited on 03/10/2020).
Yi, X. (Dec. 2016). "Electromagnetic-thermal modeling for high-frequency air-core permanent magnet motor of aircraft application". MA thesis. Urbana, IL 61801: University of Illinois at Urbana-Champaign.
Yi, X. and K.S. Haran (2019). "Thermal Integration of a High-Frequency High-Specific-Power Motor within Electrically Variable Engine". In: *2019 AIAA/IEEE Electric Aircraft Technologies Symposium (EATS)*, pp. 1–10.
Yi, X. et al. (May 2019). "Equivalent Thermal Conductivity Prediction of Form-Wound Windings with Litz Wire Considering Transposition Effect". In: *2019 IEEE International Electric Machines Drives Conference (IEMDC)*, pp. 2048–2055.
Zhang, X. et al. (July 2018). "Large electric machines for aircraft electric propulsion". English. In: *IET Electric Power Applications* 12 (6), 767–779(12). ISSN: 1751-8660.
Zheng, L. et al. (2005). "Design of a super-high speed permanent magnet synchronous motor for cryogenic applications". In: *IEEE International Conference on Electric Machines and Drives, 2005.* Pp. 874–881.
Çengel, Y.A. and J.M. Cimbala (2010). *Fluid Mechanics: Fundamentals and Applications*. 2nd ed. McGraw-Hill, Inc.

Özoğlu, Y. (2016). “New Stator Tooth for Reducing Torque Ripple in Outer Rotor Permanent Magnet Machine”. In: *Advances in Electrical and Computer Engineering* 16.3, pp. 49–56.

Erling Gjeset

Thermal Management Systems for Compact Electrical Machines

NTNU
Norwegian University of
Science and Technology